



## **Antenna Design for a Wireless Sensor Network Node**

**Tiago Miguel Carrusca Parra**

Thesis to obtain the Master of Science Degree in  
**Electrical and Computer Engineering**

Supervisors: Prof. António Manuel Restani Graça Alves Moreira  
Eng. Nuno Miguel Faria Pires

### **Examination Committee**

Chairperson: Prof. Fernando Duarte Nunes  
Supervisor: Prof. António Manuel Restani Graça Alves Moreira  
Members of the Committee: Prof. João Manuel Torres Caldinhas Simões Vaz

**April 2014**



## Acknowledgments

I would like to acknowledge all of those who continuously supported and encouraged me throughout the last year.

First and foremost, I would like to express my sincere gratitude to my supervisors, Prof. António Moreira and Nuno Pires MSc. Without their guidance, vast knowledge and persistent help this dissertation would not be possible.

I would like to thank Eng. Ricardo Rodrigues for providing the means to build a functional node prototype including my antenna proposal and an application-specific goal.

Several simulation measurements and setups would not be possible to achieve without the support and efforts of João Costa and Jerome Mollet from CST™Online Support. I would also like to leave a word of thanks to Tony Guilin, from Johanson Inc., for his advises on experimental measurement balun setups.

All the experimental measurements of this work would not be possible without the knowledge, experienced advises and laboratory know-how of António Almeida, MSc.

It is a privilege to me to leave a word of gratitude to Sr. Carlos Brito. His practical expertise, persistence and self-eduction, made the construction and assembling of the prototypes an attainable goal.

I want to thank my friends for the support and encouragement and great moments throughout my academic career.

Last but not least, I am extremely grateful to my mother, father and brother and especially to my girlfriend for the unconditional support and shared love.



## **Abstract**

Recently, there has been an increasing interest in wireless sensor networks (WSN). These networks are becoming more widely used through several applications such as military, environmental, health and industrial. Each of these may demand several application-level requirements such as mechanical dimensions of its nodes. For this reason, it follows logically that antennas for WSNs are in constant development to fulfill these requirements.

This work presents an integrated solution of an antenna for an agriculture wireless sensor network, tuned to cover the 2.4 GHz ISM band which was implemented on a node prototype.

Several studied antennas structures are presented and performance and designing constraints are assessed. The proposed solution was chosen after a vast study of balanced and unbalanced antennas.

To corroborate the simulation results of the selected antenna, a bowtie-shaped folded dipole, distinct solutions for differential impedance measurements, making use of baluns and a test-fixture, have been developed and tested. The antenna characterisation includes radiation patterns studies of the node-integrated solutions.

The proposed solution showed a better overall performance than previously used chip, and fulfills the project requirements making possible to enhance the communication performance between the WSN nodes for the intended application.

**Keywords:** Wireless Sensor Networks, printed antennas, printed baluns, differential impedance measurements.



# Contents

Acknowledgments . . . . .	iii
Abstract . . . . .	v
List of Tables . . . . .	xi
List of Figures . . . . .	xv
Glossary . . . . .	xvii
<b>1 Introduction</b>	<b>1</b>
1.1 Motivation . . . . .	1
1.2 Problem Statement . . . . .	2
1.3 Contributions . . . . .	3
1.4 Thesis structure . . . . .	3
<b>2 Wireless sensor networks and applications</b>	<b>4</b>
2.1 Introduction . . . . .	4
2.2 WSN Design . . . . .	4
2.2.1 Hardware . . . . .	4
2.2.2 Protocols . . . . .	6
2.2.3 Deployment . . . . .	6
2.2.4 Scalability . . . . .	7
2.2.5 Power consumption . . . . .	7
2.3 Network applications . . . . .	8
2.3.1 Military Applications . . . . .	8
2.3.2 Environmental Applications . . . . .	9
2.3.3 Health Applications . . . . .	11
2.3.4 Industrial Applications . . . . .	11
<b>3 Study and development of antenna solutions</b>	<b>12</b>
3.1 Introduction . . . . .	12
3.2 Requirements and design goals . . . . .	12
3.3 Unbalanced antennas . . . . .	13
3.3.1 Planar inverted F-antenna . . . . .	13
3.3.2 Chip antennas . . . . .	15

3.3.3	Whip antennas . . . . .	17
3.4	Balanced antennas . . . . .	19
3.4.1	Patch antenna . . . . .	20
3.4.2	Multiple conductor folded dipole . . . . .	22
3.4.3	Dual-band dipole antenna . . . . .	23
3.4.4	Bowtie antenna . . . . .	24
3.4.5	Bowtie-Shaped Folded Dipole (proposed antenna) . . . . .	25
3.5	Overall comparison and conclusions . . . . .	27
<b>4</b>	<b>Microstrip to balanced dipole transition design and measurement</b>	<b>29</b>
4.1	Introduction . . . . .	29
4.2	Balun characterisation . . . . .	29
4.3	Baluns solutions . . . . .	32
4.3.1	Printed balun A . . . . .	32
4.3.1.1	Balun design . . . . .	33
4.3.1.2	Simulations results . . . . .	36
4.3.1.3	Experimental results . . . . .	38
4.3.1.4	Conclusions . . . . .	39
4.3.2	Printed balun B . . . . .	40
4.3.2.1	Simulations results . . . . .	41
4.3.3	Integrated passive ceramic balun . . . . .	42
4.3.3.1	Two-port characterisation method . . . . .	43
4.3.3.2	Three-port characterisation method . . . . .	45
4.3.3.3	Extension port calibration . . . . .	47
4.4	Test fixture . . . . .	48
4.5	Conclusions . . . . .	50
<b>5</b>	<b>Proposed antenna characterisation</b>	<b>52</b>
5.1	Introduction . . . . .	52
5.2	Impedance measurement results . . . . .	52
5.3	Radiation patterns . . . . .	54
5.3.1	Bowtie-Shaped Folded Dipole (antenna proposal) . . . . .	55
5.3.2	Whip antenna (Pulse Electronics W1030) . . . . .	56
5.3.3	Chip antenna (JTI 2450AT45A100) . . . . .	57
5.3.4	Conclusions . . . . .	58
<b>6</b>	<b>Conclusions</b>	<b>59</b>
6.1	Future Work . . . . .	61
<b>A</b>	<b>Antennas and baluns mechanical dimensions</b>	<b>63</b>





# List of Tables

2.1 Commercial WSN node specifications . . . . .	5
3.1 Performance estimation of the considered antennas . . . . .	27
5.1 Maximum received power and cross-polarisation for the antennas measured in the anechoic chamber . . . . .	58



# List of Figures

1.1 Chip antenna mounted on previously build WSN node . . . . .	3
2.1 General hardware architecture of a sensor node . . . . .	5
2.2 Commercial WSN nodes . . . . .	6
2.3 Power consumption of a MICAz node . . . . .	8
2.4 False-color satellite imagery . . . . .	9
2.5 Precision agriculture in a greenhouse . . . . .	10
3.1 Illustrative perspective view of the 100mm x 50mm board . . . . .	13
3.2 Atmel PIFA . . . . .	14
3.3 PIFA simulation design . . . . .	14
3.4 PIFA return loss datasheet measurement . . . . .	15
3.5 PIFA return loss for different radiating element length . . . . .	15
3.6 Johanson Ceramic Chip Antenna . . . . .	16
3.7 Close-up of a WSN node prototype including a chip antenna . . . . .	16
3.8 Chip antenna mounting considerations . . . . .	17
3.9 Ceramic chip antenna return loss (datasheet values) with and without matching circuit . . . . .	17
3.10 Whip antenna variations . . . . .	18
3.11 Close-up of a built node prototype including a balun structure . . . . .	18
3.12 Illustration of a coplanar stripline section . . . . .	19
3.13 Differential mode - EM fields . . . . .	20
3.14 Patch antenna . . . . .	21
3.15 Patch antenna return loss . . . . .	21
3.16 Patch antenna radiation patterns at resonance 4.9 GHz . . . . .	22
3.17 Multiple conductor folded dipole . . . . .	22
3.18 Demonstration kit including the multiple conductor folded dipole . . . . .	22
3.19 Multiple conductor folded dipole return loss . . . . .	23
3.20 Dual band antenna composed of a dipole and two open loops . . . . .	24
3.21 Dual-band dipole return loss . . . . .	24
3.22 Bowtie antenna . . . . .	24
3.23 Bowtie antenna return loss and impedance . . . . .	25

3.24 Bowtie antenna radiation patterns at 2.45 GHz . . . . .	25
3.25 Bowtie-shaped folded dipole . . . . .	26
3.26 Bowtie-shaped dipole return loss and antenna magnitude impedance . . . . .	26
3.27 Bowtie-shaped folded dipole radiation patterns at 2.45 GHz . . . . .	27
3.28 Bowtie-shaped folded dipole. E-Field: absolute value . . . . .	27
3.29 Prototype node including bowtie-shaped folded dipole . . . . .	28
 4.1 Flux coupled balun transformer . . . . .	30
4.2 Block diagram of signal conversion . . . . .	30
4.3 Printed balun A . . . . .	33
4.4 Illustration of a grounded coplanar stripline (GCPS) section . . . . .	33
4.5 Side-cut illustration of a microstrip line . . . . .	34
4.6 Bend design parameters . . . . .	34
4.7 T-Junction power divider . . . . .	35
4.8 Balun A s-parameters . . . . .	37
4.9 Balun A amplitude and phase balance . . . . .	37
4.10 Balun A differential mode (mixed mode) s-parameters . . . . .	37
4.11 Test boards for measuring insertion and return losses . . . . .	38
4.12 Balun A insertion losses comparison . . . . .	39
4.13 Balun A return losses comparison . . . . .	39
4.14 GCPS-CPS transition segment of Balun A . . . . .	40
4.15 Via structure in detail . . . . .	40
4.16 Sequence of snapshots of the Balun B including the proposed antenna . . . . .	41
4.17 Balun B S-parameters - differential mode (mixed mode) . . . . .	42
4.18 Johanson Ceramic Balun . . . . .	42
4.19 Insertion Loss test board for measuring insertion loss . . . . .	43
4.20 Insertion Loss test board: S-Parameters . . . . .	44
4.21 Return loss test board for measuring return loss . . . . .	44
4.22 RL test board return loss . . . . .	45
4.23 3-port (3P) test board . . . . .	45
4.24 Ceramic chip balun amplitude and phase balance . . . . .	46
4.25 3P test board differential mixed-mode converted s-parameters . . . . .	46
4.26 CST Design Studio software embedding setup . . . . .	47
4.27 3D model of the designed test fixture . . . . .	47
4.28 Short calibration test setup . . . . .	48
4.29 Thru-Reflect-Line calibration boards for High Speed USB 3.0 Std-A/Std-B connectors . . . . .	48
4.30 Test fixture . . . . .	49
4.31 Test fixtures with different semi-rigid coaxial cable lengths . . . . .	49
4.32 Test-fixture short circuited . . . . .	50

4.33 Mounting setup for the test fixture including the BSFD antenna . . . . .	50
5.1 Balun A impedance test board including the proposed antenna . . . . .	52
5.2 Balun B impedance test board including the proposed antenna . . . . .	53
5.3 Ceramic Balun impedance test board including the proposed antenna . . . . .	53
5.4 Test fixture impedance test board including the proposed antenna . . . . .	53
5.5 Impedance magnitude measurements . . . . .	54
5.6 Anechoic chamber mounting setup . . . . .	55
5.7 Measurement positions for both E-plane and H-plane of the chip antenna . . . . .	55
5.8 Simplified 3D model of node prototype including the proposed antenna . . . . .	56
5.9 Bowtie-shaped folded dipole simulated and measured radiation pattern . . . . .	56
5.10 Whip antenna and proposed antenna radiation pattern comparison . . . . .	57
5.11 Chip antenna radiation pattern . . . . .	57



# Glossary

<b>6LoWPAN</b>	IPv6 over Low power Wireless Personal Area Network
<b>BSFD</b>	Bowtie-Shaped Folded Dipole (proposed antenna)
<b>CAD</b>	Computer Aided Design
<b>CMRR</b>	Common-Mode Rejection Ratio
<b>CPS</b>	Coplanar Stripline
<b>DBD</b>	Dual-band Dipole
<b>GCPS</b>	Grounded Coplanar Stripline
<b>HART</b>	Highway Addressable Remote Transducer Protocol
<b>IL</b>	Insertion Loss
<b>ISM band</b>	Industrial, Scientific and Medical band
<b>JTI</b>	Johanson Technology Inc.
<b>MANET</b>	Mobile Ad-hoc NETwork
<b>MMIC</b>	Monolithic microwave integrated circuit
<b>PA</b>	Precision Agriculture
<b>PIFA</b>	Planar Inverted F-Antenna
<b>QoS</b>	Quality of Service
<b>RF</b>	Radio Frequency
<b>RL</b>	Return Loss
<b>SOLT</b>	Short-Open-Load-Thru
<b>TEM</b>	Transverse Electromagnetic
<b>TRL</b>	Thru-Reflect-Line
<b>UAV</b>	Unmanned Aerial Vehicle
<b>VNA</b>	Vector Network Analyser
<b>VSWR</b>	Voltage Standing Wave Ratio
<b>WSN</b>	Wireless Sensor Network



# **Chapter 1**

## **Introduction**

### **1.1 Motivation**

Wireless sensor networks (WSN) are a new class of distributed systems [1] that consists of spatially distributed or dispersed group of devices which use dedicated sensors to monitor physical and/or environmental conditions. WSN were initially designed to facilitate military operations, but their applications have since grown to span several domains including medical, industrial, and most recently, home networks. Although this evolution had originally been fuelled by military research domains, nowadays, with the recent tremendous technological advances, the possibility of producing low-cost sensor has increased significantly, which lead us to the challenge of scaling networks to a larger number of nodes. From this point of view problems have arisen such as design of power-conservative and efficient protocols, design of data handling techniques including data querying, data mining, data fusion, data dissemination, and localisation techniques.

With the high demand and ease of designing sensor nodes, some projects in this area simply moved from private/closed research projects to open-source ones. Open-source projects have received much attention in recent years from those interested in being part of and contributing to a project. The image of an open-source can be contradictory because in one hand being part of one would not give much financial return but on the other hand it is an opportunity to learn about other research areas and, at the same time, improve our knowledge when overcoming the challenges presented. Recently, a new concept of open-source hardware projects has emerged, which shares many of the principles and approaches of free and open-source software ones.

This work aims to contribute to a software/hardware open-source project that consists of an agriculture wireless sensor network in which each device of this network transmits information according to a topology of a specifically designed protocol. Each of these devices are designed in a modular fashion in which printed circuit boards (nodes) interact to gather sensor information and transmit it to another node or to a gateway to help in decision-making.

Establishing a wireless communication channel between nodes requires an antenna module. There are several antenna structures that can be used for this specific application, but ceramic chip, whip, or

printed antennas are the most commonly used in printed circuit boards (PCB); these are studied and discussed in the next chapter. Clearly, each antenna type has its own characteristics and each system has different design requirements; for this reason, antennas are still being developed designed to fulfill requirements.

Over the last two decades, printed antennas, and particularly microstrip antennas, have found increasing applications in the industrial sector [2]. Despite the fact that these antennas were first proposed in 1953 by G.A. Deschamps [3] they have only recently become practical due to its overall low cost of substrate material and simplified manufacturing design process using CAD [2], and high demand. The advantages of microstrip antennas over conventional antennas include them being low profile (lightweight); the low fabrication cost and the capability for multiple frequency operation. There are also some disadvantages such as narrow bandwidth and low-power handling.

Characterising and measuring small antennas impedance can be a hard task. In the case of differential fed antennas, the accuracy of impedance measures has been troublesome for several years. Nowadays, researchers have developed methods to overcome these problems via baluns structures using single-ended or differential probes/test fixture.

## 1.2 Problem Statement

Wireless sensor networks for agricultural applications require integrated antennas in nodes that allow for communication within the range of few meters. Existing solutions, such as ceramic chip antennas (figure 1.1) have proven to be unsatisfactory concerning the communication range.

The purpose of this work is to contribute with a proposal of an integrated antenna solution in order to enhance the communication performance between nodes of a wireless sensor network for an agricultural application, to overcome the communication range limitation when using a chip antenna.

Requirements and project constraints concerning the substrate choice, radio-transceiver output impedance, radiation pattern and manufacturing are to be addressed in chapter two.

An important goal in this work is the development of baluns which are needed to the measurement of a differential antenna impedances.

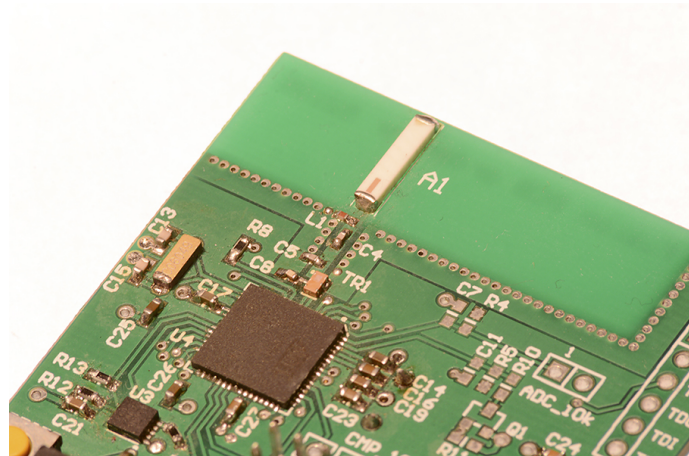


Figure 1.1: Chip antenna mounted on previously built WSN node

### 1.3 Contributions

The major contributions of this work are:

1. a new printed dipole antenna design to be used in a WSN node;
2. the design of two printed baluns, intended to provide differential impedance measurements on balanced devices;
3. the study of several characterisation techniques for printed antennas and baluns;
4. a complete experimental characterisation of the designed structures;
5. a design validation of an antenna solution to be integrated in a communication module for an agricultural wireless sensor network;
6. a functional prototype including the proposed antenna in its substrate

### 1.4 Thesis structure

This thesis work is divided in three major chapters. First, in chapter two, WSNs are introduced with a brief study and their applications in real world. The third chapter presents several antennas commonly used in WSNs and some new antenna designs. The fourth chapter addresses the problem of measuring differential antennas. The fifth chapter studies the proposed integrated antenna characterisation. Finally the thesis ends with a chapter reviewing the main conclusions drawn and proposals for future work in this area.

# Chapter 2

## Wireless sensor networks and applications

### 2.1 Introduction

WSN is a relatively new network concept in ad-hoc networks. Before the appearance of WSN, Mobile Ad-hoc Networks (MANETs) were the most common networks used to collect sensor information for data mining. MANET and WSN have important similarities but also many fundamental differences. The critical factors in the design of a WSN are: hardware; protocols; deployment; scalability and power awareness. This means that standards and protocol stacks differ significantly due to application-specific and resource-constrained goals of WSNs.

This chapter briefly addresses some aspects of WSN design and applications.

### 2.2 WSN Design

Designing a WSN requires a wide knowledge of the current state-of-the-art solutions of different research fields due to a constant development and deployment of this emerging area which is expected reach 2\$ billion by 2024 [4]. This sub chapter includes some major factors, divided in the next sections, that constraint the design of a complete network.

#### 2.2.1 Hardware

According to [5], a generalized diagram of a WSN architecture is presented in the figure 2.1. The authors of the reference divide the architecture into four major core units listed next:

- **Sensing Unit:** consists of a bundle of sensors which provide the means to gather and send physical quantities and are converted by analog to digital converters to be analysed and processed by the processing unit;

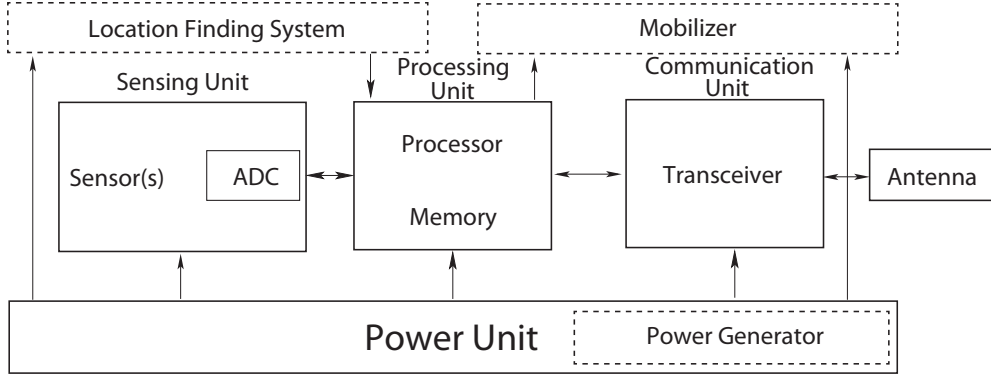


Figure 2.1: General hardware architecture of a sensor node [5]

- **Processing Unit:** frequently known as micro-processor, this unit is responsible for controlling the other units' functionalities. However, it may also contain memory and several inputs/outputs, hence, its alternative title of micro-controller;
- **Communication Unit:** this unit comprises the radio frequency transceiver which includes the antenna(s);
- **Power Unit:** this is responsible for maintaining the electric activity of the sensor node. This may be achieved by a network lifetime fuel cell or by recharging a battery via energy harvesting, such as solar energy with solar cells.

Several wireless sensor network commercial solutions (see figure 2.2) are listed below:

Specifications					
Platform	Application	Processor Speed	RAM	RF Range	Data Rate
MICA	Educational	8-16MHz	4 KB	2.4 - 2.48 GHz	38.4/250 Kbit/s
LOTUS	Industrial Monitoring	10-100 MHz	64 KB	2.4 GHz ISM	250 Kbit/s
TelosB	R&D	8 MHz	10 KB	2.4 - 2.48 GHz	250 Kbit/s
IRIS	OEM Edition	8 MHz	8 KB	2.4 GHz ISM	250 Kbit/s
LOTUS	Industrial Monitoring	8 MHz	4 KB	433 MHz ISM	Fixed
WASPmote	Versatile applications	14.7 MHz	8 KB	2.4 ISM	250 Kbit/s

Table 2.1: Commercial WSN node specifications. Adapted from [5]

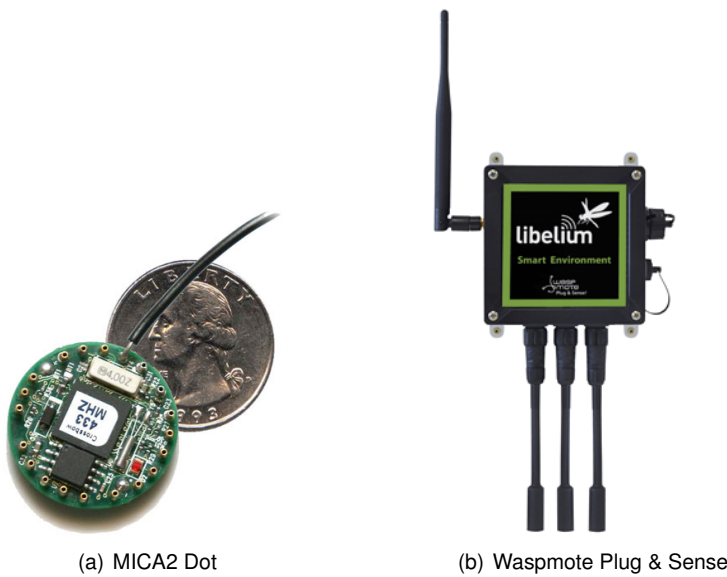


Figure 2.2: Commercial WSN nodes

## 2.2.2 Protocols

As WSN evolved, several key factors such as robustness, efficiency and reliability arose to challenge the Quality of Service (QoS). As these factors require mass expertise in all fronts of networking stack, from physical radio design to channel access schemes, routing protocols, and distributed data-processing algorithms [6], the IEEE introduced in 2003 introduced a standard which specifies the physical layer and media access control (MAC). The major features of IEEE 802.15.4 standard rely upon specifications in the physical and MAC layers for low-rate nearby communications. The standard defines, among others, that these networks should be capable of providing up to 250 kbps of data transfer rate with simple QoS requirements. The reason why this standard uses low transmission rates is because sensor network applications do not usually need high data transfer rates and consequently would clearly benefit from low-power solutions to reduce power consumption. The list below briefly reviews the most used 802.15.4 standard-based specifications:

1. Zigbee
2. Wireless HART (Highway Addressable Remote Transducer Protocol)
3. 6LoWPAN (IPv6 over Low power wireless personal area network)

Most commercial WSN solutions use one of these three standards. However each may be better suited for a particular application. For instance, Zigbee networks are targeted for home automation, smart energy, building automation, telecommunication services and health care while Wireless HART is suited for automation and industrial applications.

## 2.2.3 Deployment

Deployment of wireless sensor networks is an area that has attracted a lot of interest in the past few years. With the increasing number of nodes deployed in WSN infrastructures the ability to collect sensor

information from all nodes has been part of a strategy to succeed in real-world applications. This not only reduces the overall costs, but can also prolong network lifetime. According to [7], node deployment can be classified as:

- **static deployment:** nodes remain static during the network lifetime. This method may be sub-classified as either controlled or random deployment [8]. The mentioned reference also expose demonstrate optimization goals for this node deployment method such as: area coverage, network connectivity, network lifetime, and data fidelity.
- **dynamic deployment:** nodes may re-arrange their position due to application-level requires location changes.

These strategies are used in a wide variety of applications suggested in [8]. For instance, authors in [9] present design strategies of using unmanned aerial vehicles (UAVs) to deploy wireless sensor networks for post-disaster monitoring, which perfectly exemplifies the "random-static" deployment mentioned above.

As referred to earlier, the WSN of interest consists in a wireless sensor network for agriculture, and for this reason a "controlled-static" deployment is used in order to optimize the performance of the network.

## 2.2.4 Scalability

Wireless sensor networks may grow to contain hundreds of nodes; this creates scalability necessitate in-place routing protocols for managing and controlling scalable and adaptive networks. Several routing protocols, studied in [10] and [11] addresses these problems and assesses those which are the best routing protocols using quantitative metrics such as throughput, latency, energy consumption, and delay.

## 2.2.5 Power consumption

As referred to earlier, the power unit is a key element in the WSN node structure. However, it is also the principle time limiting factor in the lifetime of a network. Currently, batteries are the major source of energy in WSNs and/or power buffer, in the case of energy harvesting WSN nodes. In [12], the authors show the different energy sources suitable for scavenging, energy conversion devices and a wide comparison of practical energy harvesting devices such as vibration based or solar based devices. In fact, in the WSN of interest, solar energy scavenging is used with a solar cell module.

Currently, solutions to overcome this problem are based on batteries which may, in the case of nodes failure in a low density network, be quickly drained.

According to [5], sensing, communication, and data processing are the three major power consuming domains. In fact, the greatest part of the power is spent by peripherals, specifically radio modules, as figure 2.3 illustrates. To overcome the problem raised by high consumption of the radio modules, radio transceivers often feature a Wake-on-Radio functionality that essentially wakes up and listens up for incoming packets without the micro-controller interaction. This simple power-saving mechanism can save up to 99.99%, according to [5]. When it comes to the sensing unit, a periodic interval of physical

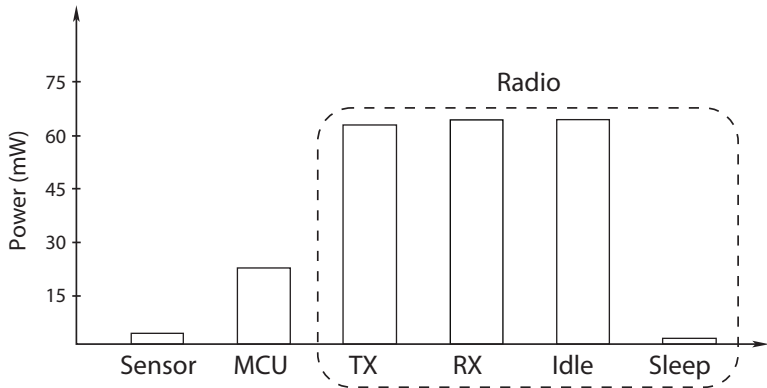


Figure 2.3: Power consumption of a MICAz node [5]

phenomenon sensor to read may also drastically decrease the energy consumed. For instance, in a wide range of air temperature sensing applications there is no sense in reading temperature in 10 seconds intervals. However, depending on the application-level this should not be the case. So, energy expended by sensors is related to the application purpose. Note that this sensors also provide waking from sleep state mechanisms independently of the micro-controller. For example, several temperature sensors provide a "configurable interrupt threshold value as well as a hysteresis value" [13].

Dynamic Voltage Scaling is another processing power-saving technique. It adapts the power supply voltage and clock frequency of the microprocessor which depends upon the workload, leading to lower energy consumption without affecting the overall performance.

## 2.3 Network applications

As expected, WSNs support a wide range of applications, from military to home monitoring. For that reason, the different types of sensors are applied according to the application. According to [5], they include seismic, magnetic, thermal, visual, etc, which are able to monitor: "temperature, humidity, pressure, speed, direction, movement, light, soil makeup, noise levels". This section addresses four main categories of WSN applications.

### 2.3.1 Military Applications

As mentioned in the motivation section in chapter 1, WSNs were first design to suit military purposes. However, due to application-level requirements, robustness, scalable self-organization, network connectivity, energy consumption, fault tolerance, and end-to-end message security are the major concerns. According to [14] these type of WSNs can be applied in four military operation scenarios:

- battlefield: large-scale and non-manually deployed;
- urban-warfare and force-protection: medium-scale and manually deployed;
- other-than-war: any scale, both manually or non-manually deployed.

In [15], a battlefield scenario requesting distribution of thousands of tactical sensors in a specific area using UAV dropping and/or artillery deployment methods is presented. It has a self-organising initialisation period and after that the information is reported to a UAV sink node.

Also [14] and [16] report, among others, several examples of military WSN applications such as perimeter protection, sniper detection and localisation [17], "chemical, biological and explosive vapor detection with micro cantilever array sensors", or monitoring friendly forces and equipment.

### 2.3.2 Environmental Applications

Environmental applications include, for example, monitoring animals [18], environmental conditions that affect crops and livestock; irrigation; precision agriculture; forest monitoring [19]; early flood detection. Considering that an antenna proposal is to be used in an agricultural application, WSNs are studied accordingly.

#### Agricultural applications

Agricultural applications can be divided into several domains according to the application itself and to scale factors. Literature constantly refers to agricultural applications as precision agriculture (PA). PA provides the means to monitor, determine, and manage agricultural practices.

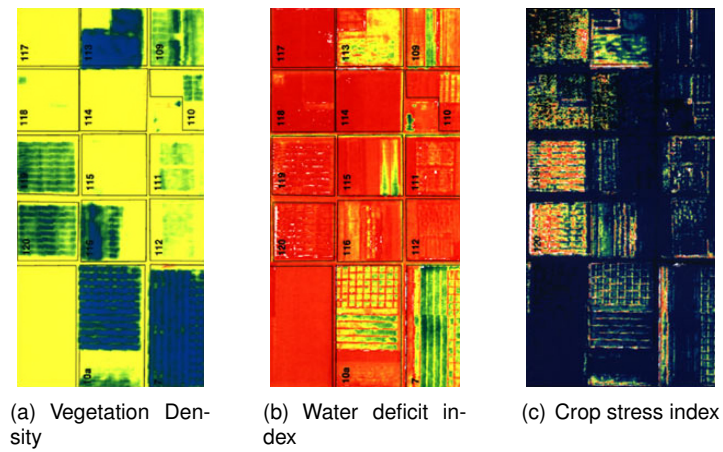


Figure 2.4: False-color satellite imagery [20]

Despite having the same goal, this designation should not be confused with precision farming. Precision farming (PF), satellite farming or site-specific crop management (SSCM) are designations to define the concept of observing, measuring and responding to false-color imagery (figure 2.4). Although PF may collect data from field sensors to improve data accuracy, the decision support system (DSS) acts solely upon data collected from GPS, satellite, aerial remote sensing to optimise the managing of soils and improve crop yields. Thus, in a sense, it does not fundamentally consist of a wireless sensor network.

In the past years, precision agriculture (figure 2.5) has been applied in order to assist agronomists and farmers with the goal of reducing the overall costs while at the same time achieving a continuous



Figure 2.5: Precision agriculture in a greenhouse [21]

and successful return of the crops by tracking the crop yield season after season. This is accomplished by optimising the crop proprieties using past data. While the advantages in a long-term were mentioned, three major short or mid-term advantages are listed below.

- Control of irrigation quantity;
- Control of chemurgy (pesticides, fertilisers);
- Control of seed germination.

In [22] for example a wireless sensor network is used to protect of a specific variety of potato against a fungal disease by tracking the temperature and humidity within the crop canopy. In [23], the authors present a WSN developed for monitoring micro-climate conditions and pest infestation in olive groves. In [24] [25] [26] solutions for optimisation, monitoring and control of water irrigation using different techniques is presented.

In [27], materials and methods and topologies to improve the deployment of a wireless sensor network in a crop field are shown

Although there are several projects reported in literature, as can be found in the references above, the sensors employed may not vary as much. According to [28] the most commonly used sensors are:

- Atmospheric pressure sensor
- Leaf Wetness sensor
- Humidity sensor
- Temperature sensor
- Luminosity sensor
- Soil moisture sensor
- Soil temperature sensor
- Ultraviolet radiation sensor
- Anemometer
- Pluviometer
- Dielectric permittivity sensor

### **2.3.3 Health Applications**

Over the last years there has been a concerted effort in research as to health applications both for humans and animals. In the case of human applications, WSN are fundamentally applied in hospitals and homes. Several applications are listed below.

- emergency response
- provision of interfaces for the disabled [29]
- integrated patient monitoring [30] [31]
- drug administration [30]
- tracking and monitoring doctors and patients in hospitals [30]
- monitoring system for wellness determination of elderly [32]
- Sudden Infant Death Syndrome (SIDS) detection [33]
- premature infant thermal regulation [33]

### **2.3.4 Industrial Applications**

The industrial sector may represent the most competitive market for WSNs. Thus, manufacturers invest in monitoring and control applications to reduce the products overall cost, by reducing the human-factors and preventing manufacturing downtime of their plants. According to [34] the industrial applications can be divided based on specific production requirements.

- Industrial environmental sensing
  - pollution
  - hazard
  - security
- Condition monitoring
  - structural health
  - equipment condition
  - human error monitoring
- Process automation
  - evaluation
  - improvement

# **Chapter 3**

## **Study and development of antenna solutions**

### **3.1 Introduction**

As mentioned in chapter 2, WSNs may be implemented in a wide range of applications. As expected, each of these applications may require different node distinctive node deployment, hence, very contrasting topologies. This fact may drastically reduce the probability of finding a completely designed and characterised antenna suited for a specific WSN. The next section addresses the requirements for this work project. After recognizing the requirements, constraints and design goals, an extensive study and comparison of commonly used antennas in wireless sensor networks is addressed. Also, several antennas are designed and finally only one is chosen to be implemented in the communication module.

### **3.2 Requirements and design goals**

As stated in the previous chapter, micro-controllers can integrate a communication unit which is the case of this work.

The micro-controller of interest, the ATMEL ATmega128RFA1, is a fully integrated low-power transceiver (Zigbee and 802.15.4) for the 2.4 GHz ISM band. It comprises a RAM of 128 Kbytes and a maximum operating frequency of 16 MHz. The RF port has a  $100+0j \Omega$  differential impedance and provides -100 dBm sensitivity and transmitting output power up to 3.5 dBm [35].

The requirements and manufacturing constraints needing to be fulfilled in this work are listed below.

Requirements:

1. printed antenna on FR-4 substrate (0.8 mm thickness and  $\epsilon_r = 4.3$ ) with a copper layer thickness of 35  $\mu\text{m}$ .
2. antenna without extra circuit elements;
3. frequency range: 2.4 - 2.5 GHz (2.4 GHz ISM band)

4. omni-directional radiation pattern in one of the operational planes;
5. highly efficient radiation;
6. maximum antenna size of 60 mm x 50 mm;

Manufacturing constraints:

1. minimum trace width of 6 mils (0.1524 mm);
2. minimum trace space of 6 mils (0.1524 mm);

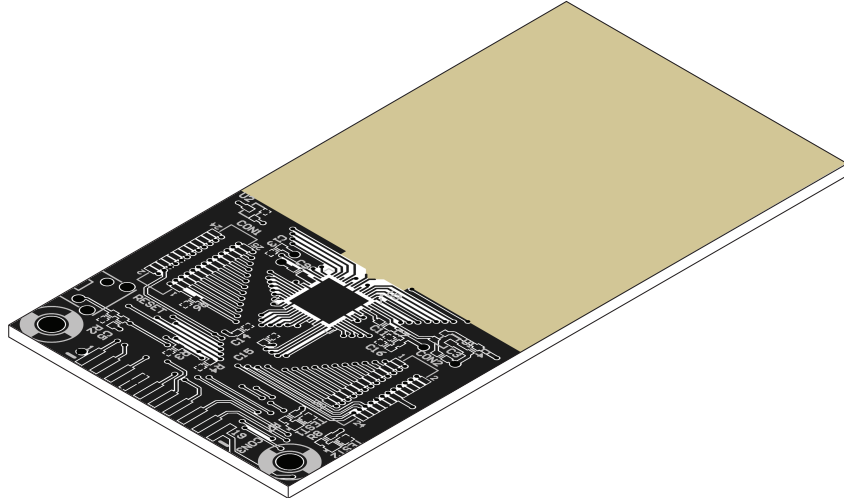


Figure 3.1: Illustrative perspective view of the 100mm x 50mm board

To clarify the mechanical dimensions requirements, figure 3.1 illustrates the area available for antenna design. The manufacturer of the PCB circuit boards (Seeestudio) only allows boards with a minimum of 50 mm x 50 mm area, and as the circuit itself has approximately 40 mm x 50 mm of impressed circuitry, it was decided to extend the available design area to 50 mm x 60 mm, thus equalling a full size of 100 mm x 50 mm.

### 3.3 Unbalanced antennas

In this section, WSN commonly used unbalanced antennas are studied. However, as stated before, the output/input of the RF interface is balanced, which means that using one of these antennas introduces a new challenge of converting the balanced signal to an unbalanced signal. Subsequently, a balun structure and other lumped extra components besides the antenna may be required.

#### 3.3.1 Planar inverted F-antenna

A planar inverted F-antenna (PIFA), suggested by Texas Instruments for 2.4 GHz ISM band [36] is illustrated in figure 3.2. This antenna design implemented by 3TEC in a WSN node [37], claims a communications range of "50 m indoor range and about 125 m outdoors", which is satisfactory for this project scope. Although this antenna does not have a differential feeding point, it was agreed to study this configuration due to its compact size.

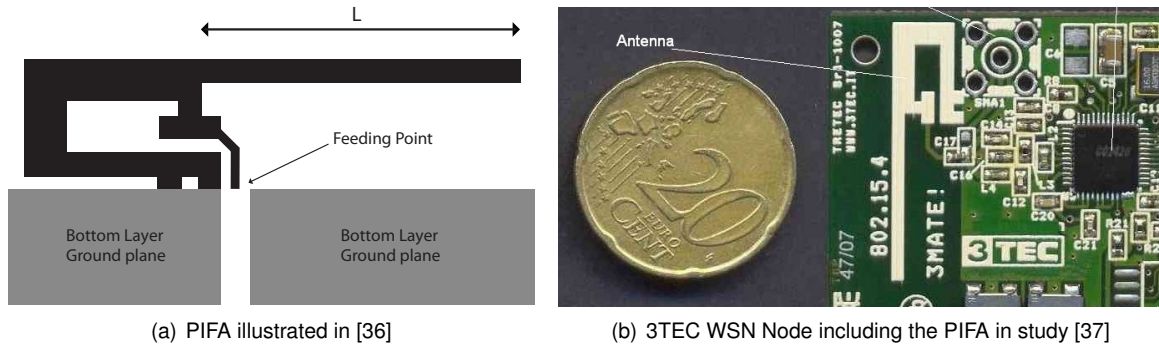


Figure 3.2: Atmel PIFA

The information provided in [36] suggests a peak gain of +3.3dB and an overall size of 25.7 mm x 7.5 mm, which makes this antenna a compact solution for 2.4 GHz ISM band. It is also stated that this antenna does "not require any matching components" and the feed point is "matched directly to 50 Ohm", which is the microstrip transmission line beginning at the surface edge of the antenna as figure 3.2 suggests.

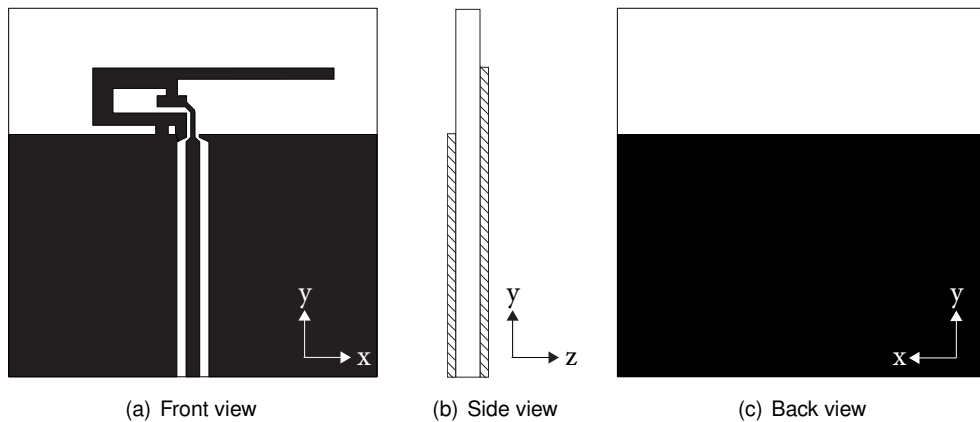


Figure 3.3: PIFA simulation design

Some details are not completely clear as the height of the substrate and length of the radiating element vary across two application notes [36][38] for the same model. This intrinsically implies that a variation on the height of the substrate for this antenna causes a detuning which can be reversed by changing the length of the radiating element [39]. Furthermore, datasheet values for measured reflection coefficient, shown in figure 3.4, at the feed point of the antenna show approximately 24 dB.

Several simulations were conducted in order to confirm the implications of changing the length of the radiating element. It was decided to use a grounded coplanar waveguide transmission line of 50 Ohm to match the feed point referred above (figure 3.3). Results are presented in figure 3.5 according to the available dimensions.

Return losses curves presented in figure 3.5, show that this antenna may be easily detuned, due to a minor variation on the length of the radiating element,  $L$ , illustrated in figure 3.2(a).

However, this fact can turn out to be an advantage when considering this antenna design. To tune this antenna, on a prototype tuning board, instead of implementing the radio transceiver and balun,

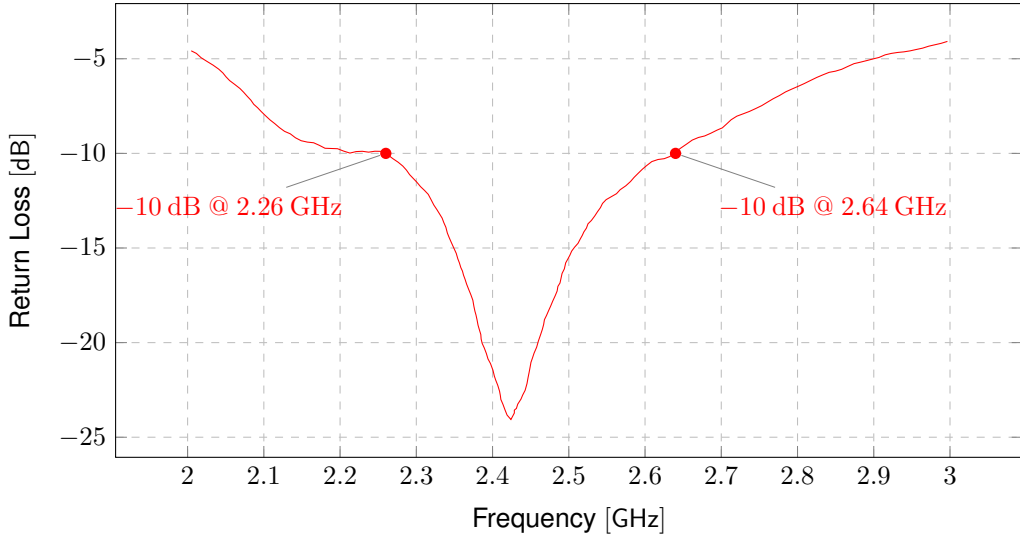


Figure 3.4: PIFA return loss datasheet measurement

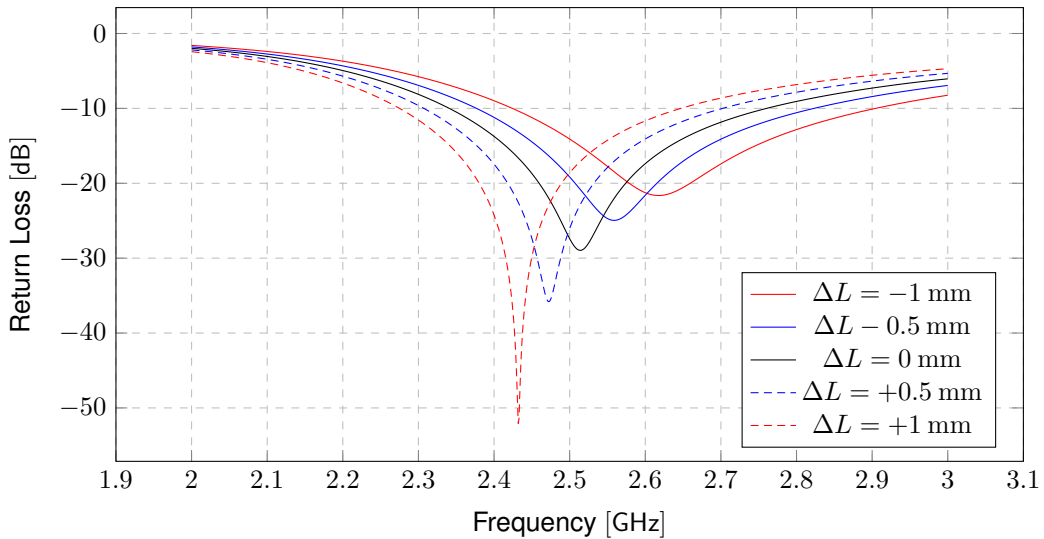


Figure 3.5: PIFA return loss for different radiating element length.  $\Delta L = 0$  corresponds to  $L = 16.4$  mm

these are replaced by an SMA connector in the feeding point of figure 3.2(a). The antenna on the tuning board has to be designed with an oversized radiating element. Hence, by checking with a VNA the reflection coefficient, the radiating element can be interactively trimmed to provide the desired resonance frequency.

It would be interesting to proceed with this antenna design in this project if balanced feeding could be considered as an option.

### 3.3.2 Chip antennas

Ceramic antennas can be built in several antenna structures including monopoles, inverted F antennas, and planar inverted F antennas (PIFA). Figure 3.6(a) depicts a quarter-wavelength monopole which features a gold radiating element encapsulated in ceramic. Its mechanical dimensions are shown in

figure 3.6(b).

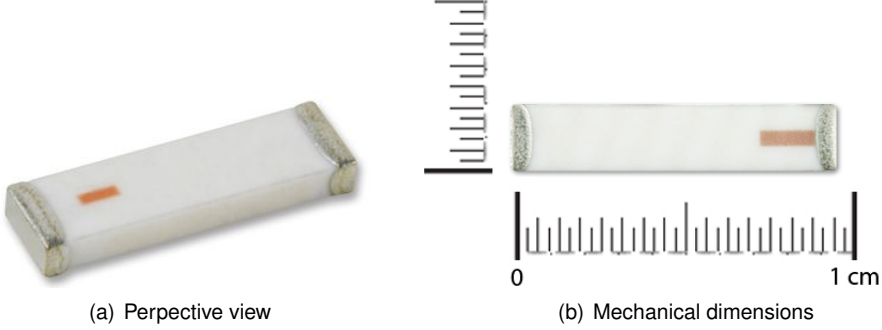


Figure 3.6: Johanson Ceramic Chip Antenna

As stated, previously to this work, a ceramic chip antenna specifically chosen for the WSN node was implemented as illustrated in first chapter (fig. 1.1) and in a cropped figure 3.7.

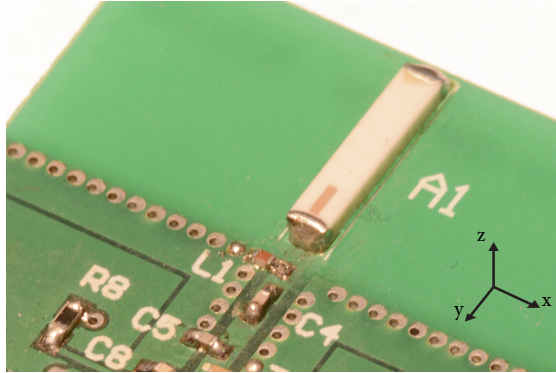


Figure 3.7: Close-up of a WSN node prototype including a chip antenna

To enhance the overall performance of these antennas they should be designed with great care regarding keep-out areas, orientation, circuit board design, interference, proximity de-tuning and degradation concerns. According to [40], "efficiency is not exceptionally high and is typically in the range of 10-50%, which corresponds to 3 to 10 dB loss", consequently reducing the frequency range. As also stated, "buying a chip antenna does not guarantee good performance". Moreover, the initial cost of the antenna plus the logistics that involves optimisation of the final board might be higher than the cost of a printed antenna. As an option, to tune these antennas, this manufacturer provides a paid custom service to tune their antenna solutions embedded in custom circuit boards [41].

Besides that, several advantages such as small sizes, on-ground or off-ground designs, design flexibility and initial cost make these the most typical antennas used on circuit boards with RF interfaces.

According to the datasheet of this model [42], 2450AT45A100, the manufacturer guarantees the following specifications:

1. frequency range: 2400 - 2500 MHz;
2. return loss: 9.5 dB min;
3. average gain: 1.0 dBi typ (XZ-Vert. pol. - axes in figure 3.7);
4. peak gain: 3.0 dBi typ. (XZ-Vert. pol.);

5. impedance:  $50 \Omega$ .

Several chip antennas may require the use of matching networks which in this case require a matching network in order to tune to the desired frequency. This particular model requires a  $1.5\text{pF}$  capacitor and an  $3.9\text{nH}$  inductor as shown in figure 3.8(b).

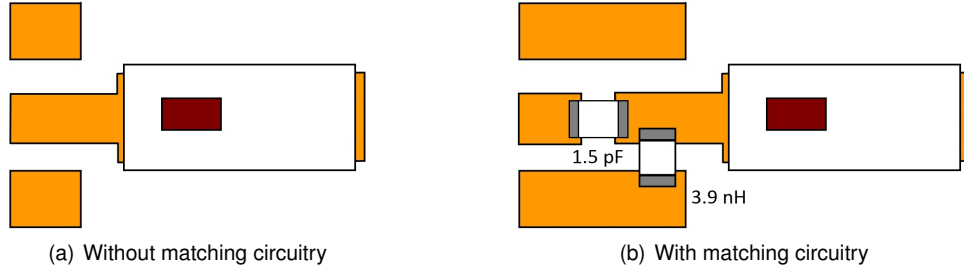


Figure 3.8: Chip antenna mounting considerations

This matching technique significantly increases the return loss and the bandwidth, as figure 3.9 illustrates, by tuning the antenna with non-resistive components. It is also referred to in the datasheet that the distance from the inductor to the antenna may change, which suggests that every custom printed circuit board implemented with this antenna should be tuned individually.

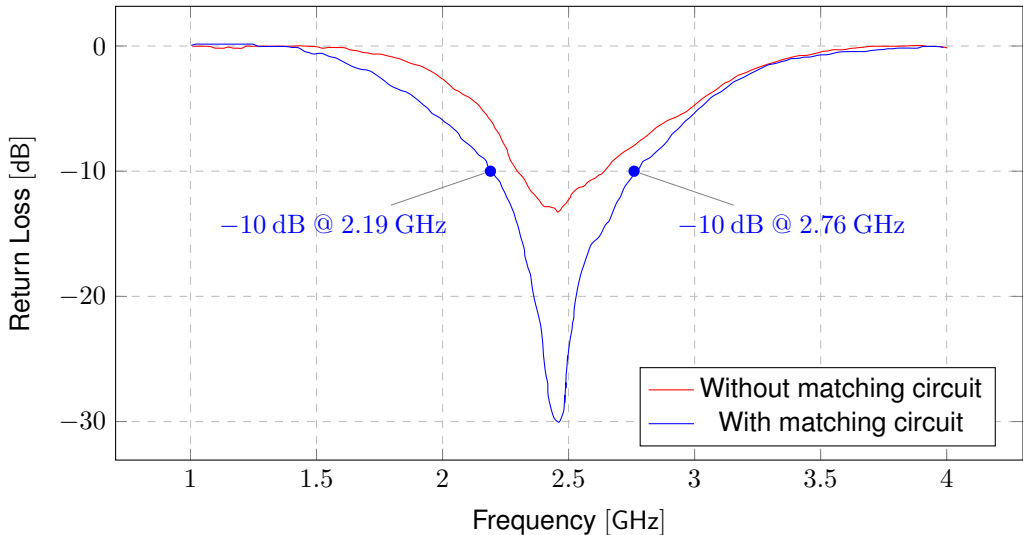


Figure 3.9: Ceramic chip antenna return loss (datasheet values) with and without matching circuit

The main drawback of this antenna solution is its low-efficiency. A communication module prototype could not establish a satisfactory transmission beyond 3 meters range. Thus, an alternative antenna solution should be found.

### 3.3.3 Whip antennas

A whip antenna, frequently called "ducky" or "stick" antenna is in its basic form a single-element antenna. Although these are commonly defined as monopoles, the fact is that helical and dipole antenna structures are also available in this antenna type (figure 3.10).



Figure 3.10: Whip antenna variations

The use of these antennas brings several advantages to the project. The first is the omnidirectional radiation pattern. Also, a whip antenna may be installed outside an potential WSN node enclosure case. In comparison with previous antenna solutions this can be beneficial if the radiation pattern distortion caused by the protective enclosure is a primary concern.

However, these antennas have a high cost of manufacturing, which imposes higher production costs when comparing with chip or printed antennas. Also, another problem arises: similarly to ceramic chip antennas, the unbalanced feeding point of this type of antennas requires a balun structure in order to convert the balanced feeding from the micro-controller radio transceiver to an unbalanced feeding of the whip.

Previously to this project work, a whip antenna was also implemented in a prototype node board as shown in 3.11. The model used, a Pulse Electronics W1030 [43] (figure 3.10(c)) is a one-quarter wavelength dipole. The gain is 2.0 dBi, and the return loss is less than -10 dB ( $VSWR < 2$ ) for the 2.4-2.5 GHz frequency range. As usual the SMA connector allows a unbalanced feeding point with  $50\ \Omega$  impedance.

Figure 3.11 also illustrates the components used between the micro-controller and the whip antenna, due to the requirement of a balun to convert the  $100\ \Omega$  balanced impedance to  $50\ \Omega$  unbalanced impedance of the whip antenna.

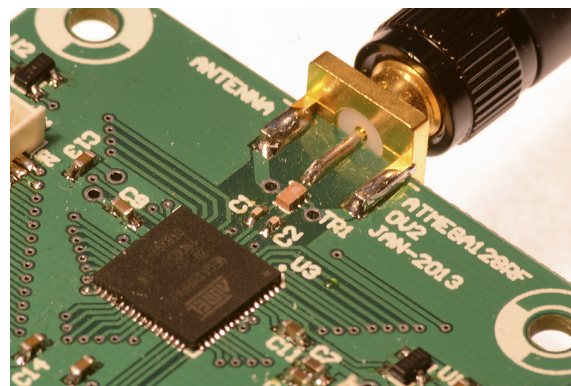


Figure 3.11: Close-up of a built node prototype including a balun structure

### 3.4 Balanced antennas

As explained in section 3.2, an integrated printed antenna with the required impedance should be considered.

As already stated, the transceiver has a differential feed, meaning that it provides a differential voltage between two terminals. These two conditions immediately suggest a solution based on balanced fed antennas, despite the fact that a single-ended fed could also be implemented.

A differential or balanced antenna is a simple designation for an antenna which is, normally, a symmetrical center-fed structure. This means that currents flow with equal and opposite currents in the feeding port of the antenna. The simplest and most-known form of balanced antennas is a half-wavelength dipole which consists of two quarter-wavelength elements displaced in a back-to-back configuration equalling a length of  $L = \lambda/2$ . This configuration yields a sinusoidal current along dipole arms as well as an omnidirectional radiation pattern, which fulfils one of the project's requirements.

Assuming that a balanced antenna is used in this project, a transmission line to connect it to the transceiver is required. In microwave communications, transmission lines can be found in different types of structures such as striplines, microstrips and waveguides. In this work only printed lines will be studied as this was defined as a requirement of the project. To "connect" the radiating element to the radio transceiver there are two possible main structures that can be applied in the whole design of the antenna: coplanar striplines (CPS) and grounded coplanar stripline (GCPS), both which are considered to have a differential pair transmission line. CPS has the advantage the fact that the built antenna is not so close to a ground plane closeness which would affect the antenna pattern, distorting it from the desired omnidirectional behaviour. Moreover, the performance of coplanar lines is comparable to, and sometimes superior to microstrip line in terms of guided wavelength, dispersion, and losses [44]. Coplanar strips transmission lines or coplanar striplines are designations given to a setting of two conductor strips of width "w" in close proximity, defined by a gap of width "d" and supported by a dielectric of thickness "h" (see figure 3.12). If the strips have different width it is said to be a "asymmetric CPS" otherwise is called symmetric CPS or simply CPS.

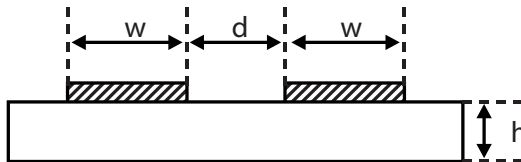


Figure 3.12: Illustration of a coplanar stripline section

### EM fields and Propagating modes

The structure in figure 3.13, supports a quasi-TEM (Hybrid mode), which has non-zero electric and magnetic fields in the direction of propagation (YY). Hybrid modes have higher order modes with cut-off frequencies different from DC (0 Hz) and are undesirable. These modes are a combination of both, the transverse electric (TE) and transverse magnetic (TM) modes and thus have the longitudinal compo-

nents of both, the electric and the magnetic fields. The wave propagates in two different media (air and dielectric) in a hybrid mode.

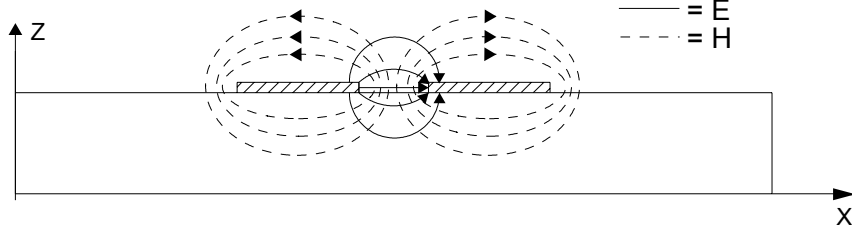


Figure 3.13: Differential mode - EM fields

### Differential impedance of CPS structures

As stated in [45], the characteristic differential impedance of a CPS structure of the hybrid mode can be studied using (analytical) approximations in equations 3.1 and 3.2. The author in [45], also state that the equations 3.1 and 3.2 are satisfactorily accurate in a wide range of substrate thicknesses.

$$Z_\phi = \frac{30\pi}{\sqrt{\epsilon_{eff}}} \frac{K(k')}{K(k)} . \quad (3.1)$$

$$\epsilon_{eff} = 1 + \frac{\epsilon_r - 1}{2} \frac{K(k')K(k_1)}{K(k)K(k'_1)} . \quad (3.2)$$

$$k = \frac{a}{b} \quad \text{where} \quad a = d/2 \quad , \quad b = \frac{2w+s}{2} \quad (3.3)$$

$$k_1 = \frac{\sinh(\pi a/2h)}{\sinh(\pi b/2h)} . \quad (3.4)$$

Note that in equations 3.1 and 3.2,  $K$  function is the complete elliptical integral of the first kind and  $k' = \sqrt{(1 - k^2)}$ .

#### 3.4.1 Patch antenna

A patch antenna was presented in [46] for a radar application requiring differential feeding. The authors present a design of a symmetrically fed patch antenna with low return loss at 24.25 GHz. The antenna should match a  $100\Omega$  differential output port impedance of a MMIC via a transmission line. A tapered coplanar grounded microstrip is used to connect the radiating element to the MMIC. At  $y=0$  (figure 3.14) due to the close proximity between microstrip lines and because these lines are excited with equal magnitude and phase opposition currents, coupling with the two microstrip lines to create an odd-mode, more precisely, a differential mode.

The mentioned reference does not provide either dimensions of the patch nor the materials used. An antenna was re-designed for 2.45 GHz using the same feeding structure. A re-scaling was performed in

order to lower the operating frequency and fit the area available for the design. The ground place was limited in size so that the patch radiated for both sides.

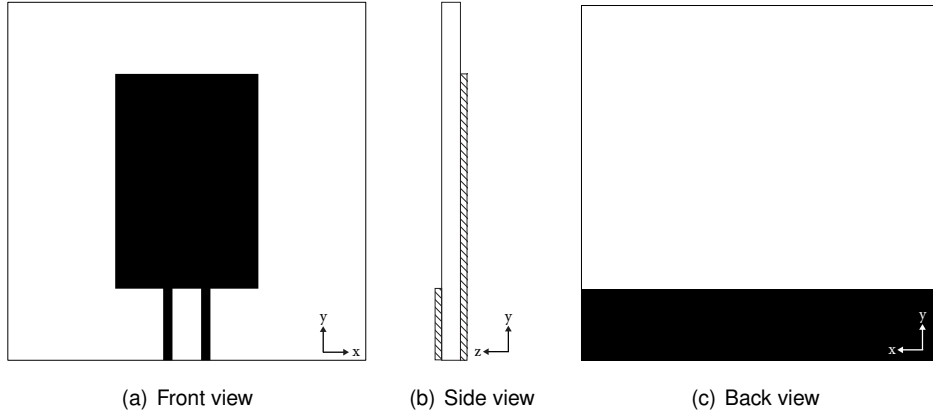


Figure 3.14: Patch antenna

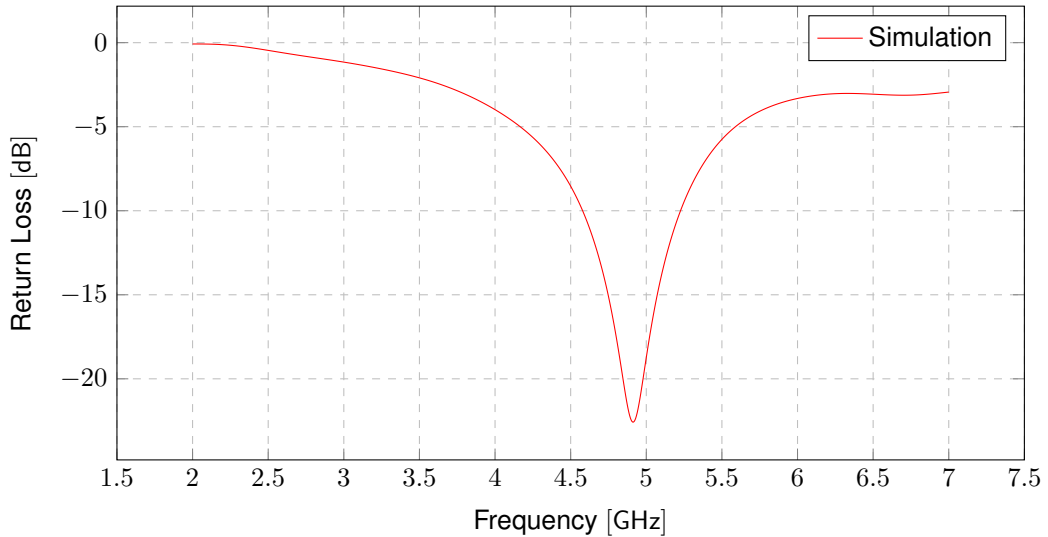


Figure 3.15: Patch antenna return loss

The results of the simulated return losses of the redesigned antenna, presented in the figure 3.15, show that due to dimensions restrictions, it is not possible to tune this antenna at the 2.45 GHz operating frequency. Moreover, this antenna does not have an omni-directional radiation pattern as shown in figure 3.16 for the resonant frequency 4.9 GHz; once again requirements could not be met. It can be noted that it would be easy to re-scale the antenna structure to other bands such as the 5.8 GHz ISM. A re-design of the coplanar stripline may be required in order to achieve the desired impedance.

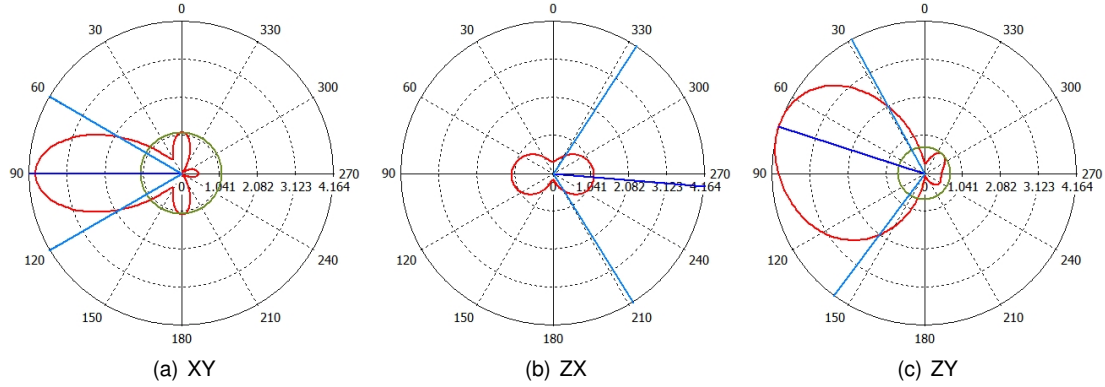


Figure 3.16: Patch antenna radiation patterns at resonance 4.9 GHz. Values are normalized to maximum gain (ZX)  $G = 4.16$

### 3.4.2 Multiple conductor folded dipole

An antenna inspired by a multiple conductor folded dipole geometry, illustrated in figure 3.17, was proposed by Atmel for a radio controller board kit to demonstrate point-to-point communications in wireless low-rate personal area networks [47]. The transceiver used in micro-controller model, Atmel ATAVRRZ200, has the required differential antenna output impedance. Along with the kit, an application note on the design and characterisation of the antenna is provided. An illustration is presented below in figure 3.17 and also a photography of the assembled kit including the antenna provided.

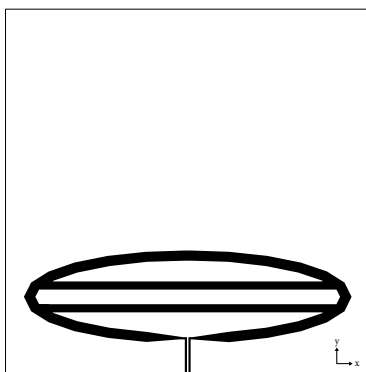


Figure 3.17: Multiple conductor folded dipole



Figure 3.18: Demonstration kit including the multiple conductor folded dipole

Note that as this antenna is a modification of a four-conductor folded printed dipole, a theoretical simplified model implying that it should have an impedance of  $4^2 \times 73 \Omega$ , i.e.,  $1168 \Omega$ , if the conductors length were equal (which is not the case) to half of a wavelength.

To corroborate the results presented in the application note, this antenna was subject of simulation in the *CST Microwave Studio*. Several parameters not mentioned in that document such as, thickness and relative permittivity of the dielectric, or copper thickness were taken as the parameters required for the design of the final antenna referred in section 3.2.

As shown in figure 3.19, and despite the fact that the antenna is fed by a  $96 \Omega$  coplanar stripline, the return loss simulated did not match the expected results. By converting the simulated reflection

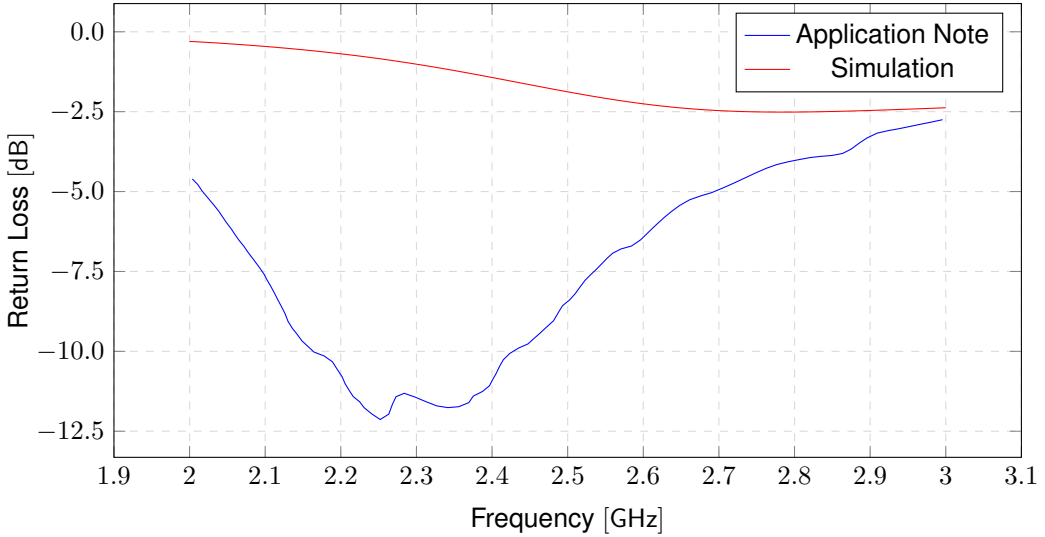


Figure 3.19: Multiple conductor folded dipole return loss

coefficient (see equation 3.5) to the respective impedance of the antenna, its magnitude reveals, at 2.45 GHz,  $223 \Omega$ , which is not close to the  $76 \Omega$  announced in [47]. Thus, this antenna design was not considered as a valid solution for this work.

$$Z = Z_0 \frac{1 + \Gamma}{1 - \Gamma}, \quad Z_0 = 50 \Omega \quad (3.5)$$

Further information on the impedance measurements in the application note is present in the reference [47].

### 3.4.3 Dual-band dipole antenna

A dual-band dipole (DBD) antenna proposed in [48] is illustrated in figure 3.20 for the 2.4 GHz and 5.2 GHz band. It was decided to analyse this antenna given that it fit all the requirements and constraints described in 3.2.

This antenna has a dipole structure in the top copper layer radiating at 5.2 GHz and two open rectangular loop resonators in the bottom copper layer, which radiate at 2.4 GHz due to the coupling effect with the top layer dipole. According to the authors this antenna has an omni-directional pattern at both 2.4 and 5.2 GHz and, it exhibits a peak gain (on the E-plane) of 2.7 and 3.7 dBi respectively.

Figure 3.21 illustrates the return loss for several antennas presented in [48]. The antenna of interest in this study is represented by the "double dipole" curve. It might be difficult to visualise the value of return loss at 2.45 GHz but is certainly between -15 dB and -20 dB.

Please note that the discontinuity of the truncated ground plane introduces losses and thus inefficiency in the antenna, which is not discussed in the reference.

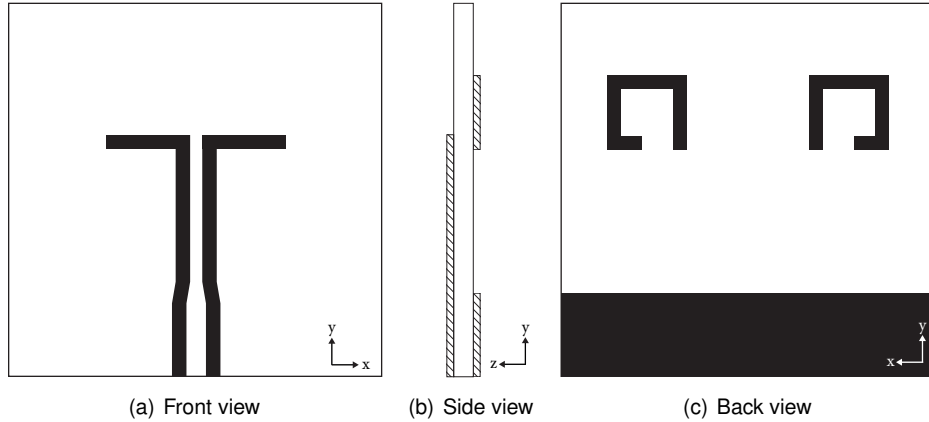


Figure 3.20: Dual band antenna composed of a dipole and two open loops

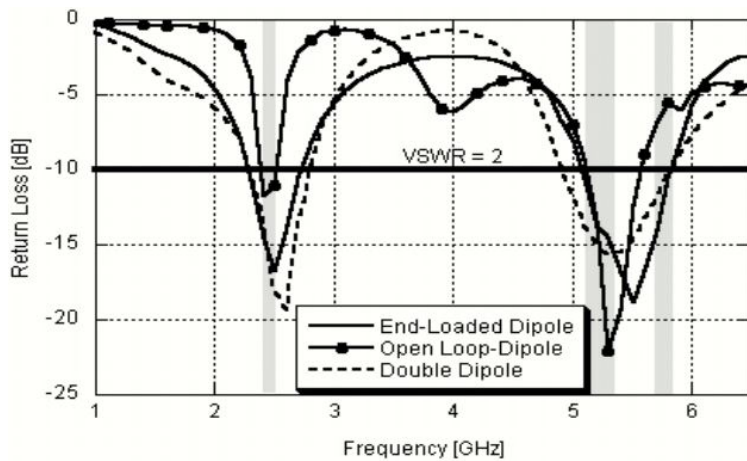


Figure 3.21: Dual-band dipole return loss [48]

### 3.4.4 Bowtie antenna

A bowtie dipole antenna (figure 3.22) was re-scaled using the concept of reference [49] and optimized according to the requirements. Note that the transmission line from the edge of the board to the feeding point does not have tapering, thus no impedance mismatch occurs.

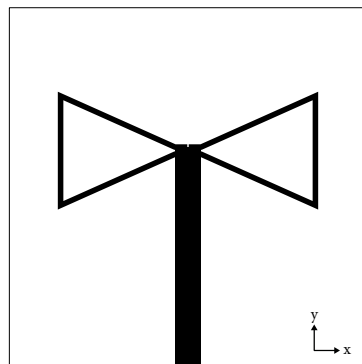


Figure 3.22: Bowtie antenna

As shown in the figure 3.23, this antenna suits the requirements for this project, as a result of -24 dB

return loss and good impedance match close to 100 Ohm at the central frequency of the desired band. However, the CPS gap "d" (see figure 3.12) is very close to the minimum trace space guaranteed by the manufacturer, thus making this fact a minor drawback. This antenna should be considered as a valid antenna proposal and it is subject of comparison with other valid options in section 3.5.

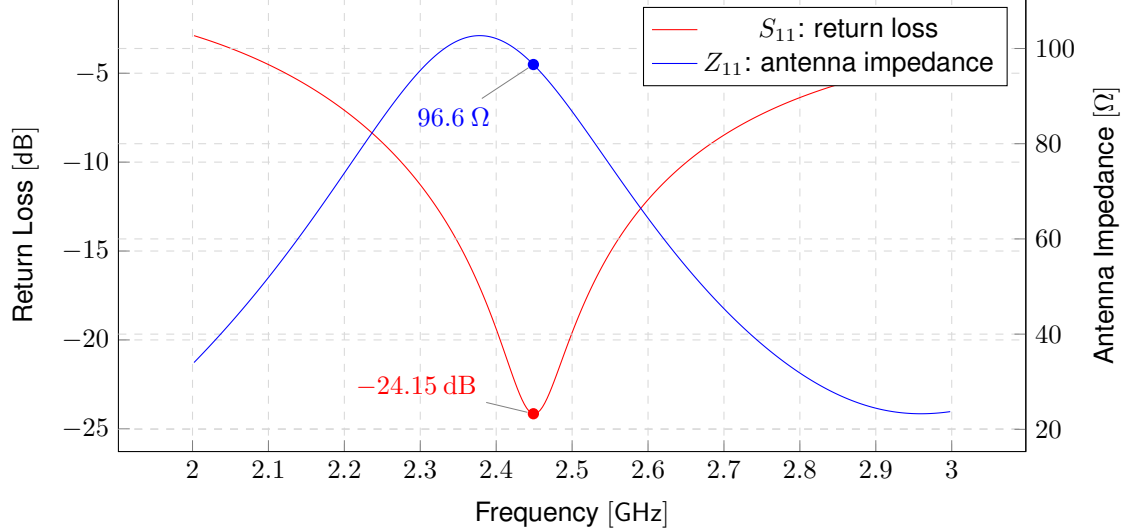


Figure 3.23: Bowtie antenna return loss and impedance

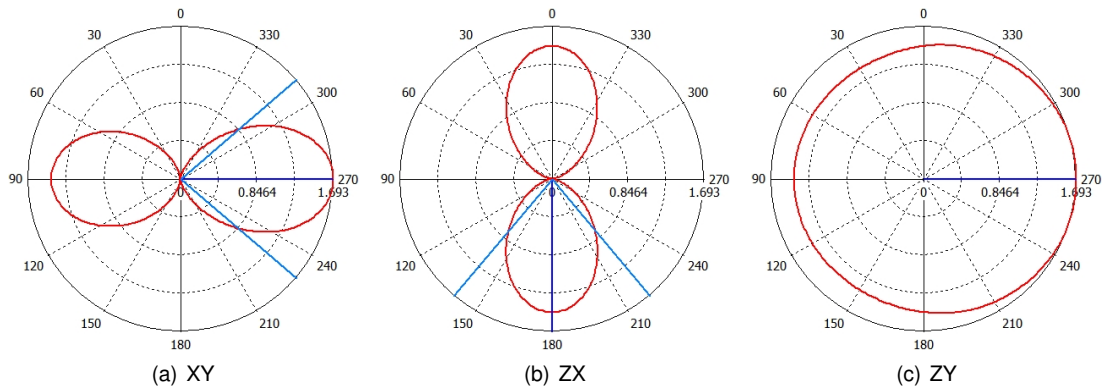


Figure 3.24: Bowtie antenna radiation patterns (linear scaling) at 2.45 GHz according to different cutting-planes.

See Appendix A for mechanical dimensions of the antenna.

### 3.4.5 Bowtie-Shaped Folded Dipole (proposed antenna)

A bowtie-shaped folded dipole (BSFD), illustrated in figure 3.25, has been designed with the purpose of acting as a solution for this project. This antenna has an approximate differential impedance of  $200 \Omega$  at the feeding point which provides a 50 dB return loss at 2.67 GHz. Thus, in order to shift the resonant frequency to 2.45 GHz and to easily provide the connection to the micro-controller, a transmission line was added. This line acts as a quarter-wavelength transformer shifting the resonant frequency and at the same time performing an impedance transformation to an almost pure resistive antenna. Through a

software optimisation process the best dimensions obtained are reported in appendix I.

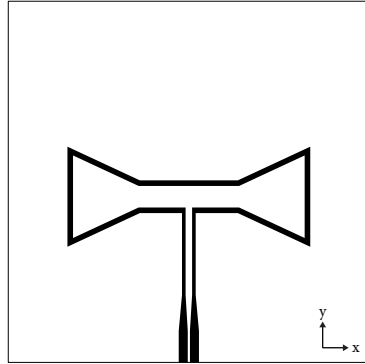


Figure 3.25: Bowtie-shaped folded dipole

Figure 3.26 shows the simulation curves for the impedance and return loss of the antenna. As shown, the optimal value for return loss is relatively close to the center value of the 2.4 GHz ISM band. As also illustrated, the impedance of the antenna is near the desired  $100 \Omega$  which makes it a considerable option for the work.

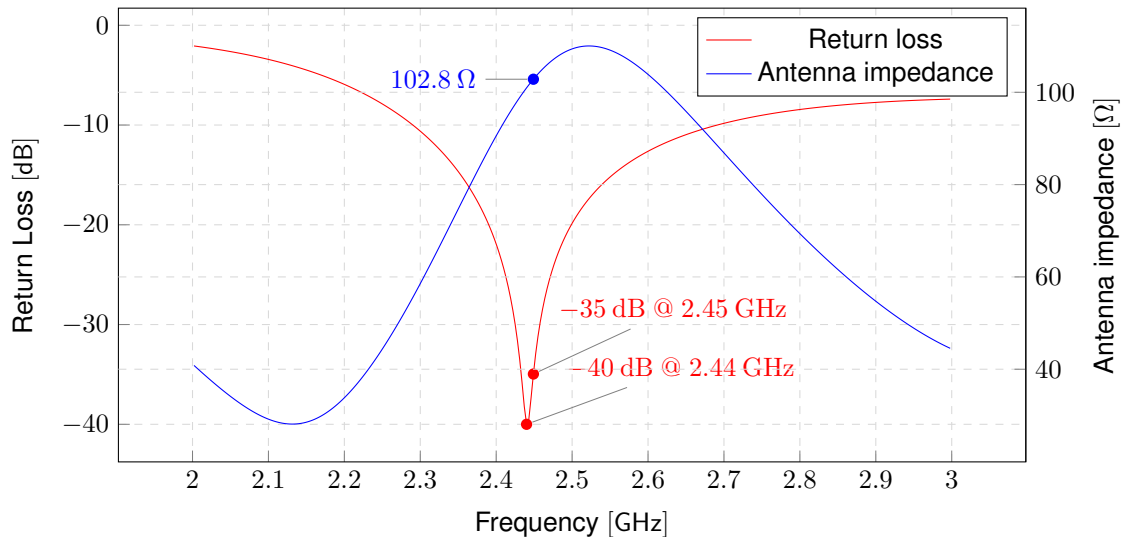


Figure 3.26: Bowtie-shaped dipole return loss and antenna magnitude impedance

The radiation patterns for the antenna are presented in figure 3.27 (axes shown in figure 3.25). Due to the fact that this antenna has great similarities with a simple dipole, an omni-directional pattern is achieved in the ZY cutting plane, as expected. Note that the values on the radiation patterns are normalised to the antenna maximum gain,  $G = 1.653$ .

A sequence of snapshots of electric field distribution around the conductors is illustrated in figure 3.28 where a low reflection, and consequently good matching, is obtained.

This antenna was chosen to be implemented in a prototype RF module for the agriculture WSN because it fulfils the project requirements.

See Appendix A for mechanical dimensions of the antenna.

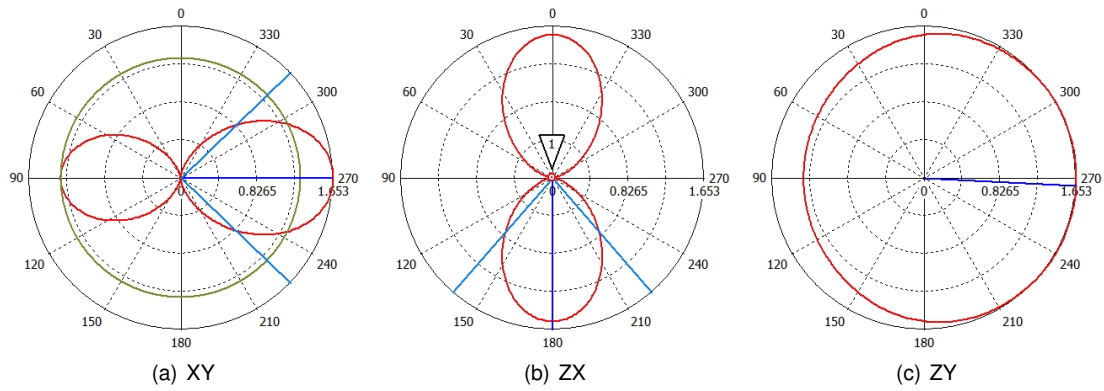


Figure 3.27: Bowtie-shaped folded dipole radiation patterns (linear scaling) at 2.45 GHz according to different cutting-planes

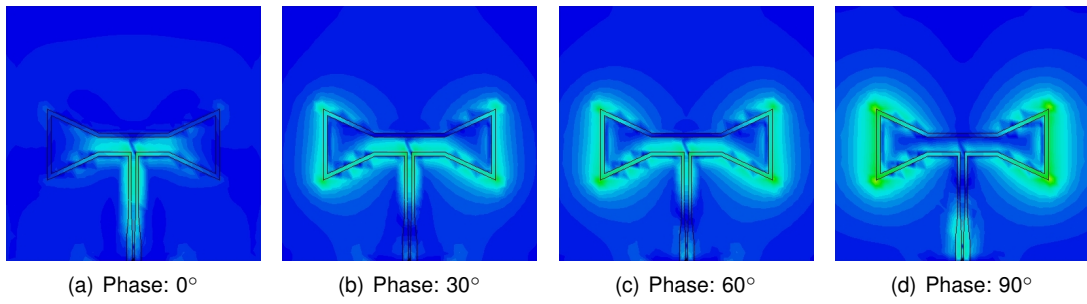


Figure 3.28: Bowtie-shaped folded dipole. E-Field: absolute value

### 3.5 Overall comparison and conclusions

Several specifications regarding the studied antennas are presented in table 3.1. Please note that both the Patch antenna and the Multiple conductor folded dipole are not shown due to unsatisfactory performance. Refer to 3.4.1 and 3.4.2 for more detailed information on these antennas.

Performance parameter	Antennas					
	PIFA <sup>1</sup>	Chip <sup>1</sup>	Whip <sup>1</sup>	Bowtie <sup>2</sup>	BSFD <sup>2</sup>	DBD
Feeding type	Bal.	Bal.	Bal.	Unbal.	Unbal.	Unbal.
Impedance ( $\Omega$ ) <sup>3</sup>	50	50	50	96.6 $\Omega$	102.8 $\Omega$	100 $\Omega$
Return Loss (dB) <sup>3</sup>	-21	-29	< -10	-24.2	-34.9	$\simeq$ -17
Bandwidth (%)	15.5	23.03	- <sup>4</sup>	15.5	16.4	- <sup>4</sup>
Peak gain (dBi)	2.7	3.0	2.0	2.3	2.3	2.7
Efficiency (%)	93.2 <sup>3</sup>	- <sup>4</sup>	- <sup>4</sup>	97.1	98.3	- <sup>4</sup>
Price range (\$) <sup>5</sup>	5-0.7 <sup>6</sup>	1.3-0.4 <sup>7</sup>	3.4-1.8 <sup>8</sup>	5-0.7 <sup>6</sup>	5-0.7 <sup>6</sup>	5-0.7 <sup>6</sup>

<sup>1</sup> This antenna structure can only be used when combined with a balun

<sup>2</sup> The values presented for the antenna are simulated results

<sup>3</sup> Value for 2.45 GHz frequency

<sup>4</sup> Value not available

<sup>5</sup> The price range vary from 1 unit to 2500 units

<sup>6</sup> Seedstudio and Eurocircuits

<sup>7</sup> Farnell

<sup>8</sup> Digikey

Table 3.1: Performance estimation of the considered antennas

Considering that the manufacturing process has mechanical variations measured by a tolerance factor, the fact that the CPS gap is smaller in the bowtie antenna suggests that a minor variation in this gap would change the impedance of the transmission line, thus, resulting in an antenna impedance mismatch. Regarding the dual-band antenna, it did not show an excellent performance concerning return loss and bandwidth, and was excluded.

For these reasons and also because the bowtie-shaped folded dipole exhibited better performance in what concerns to the the return loss and maximum impedance mismatch, this was the antenna proposal to be implemented on a fully working prototype node. Figure 3.29 depicts the final node including the designed bowtie-shaped folded dipole.

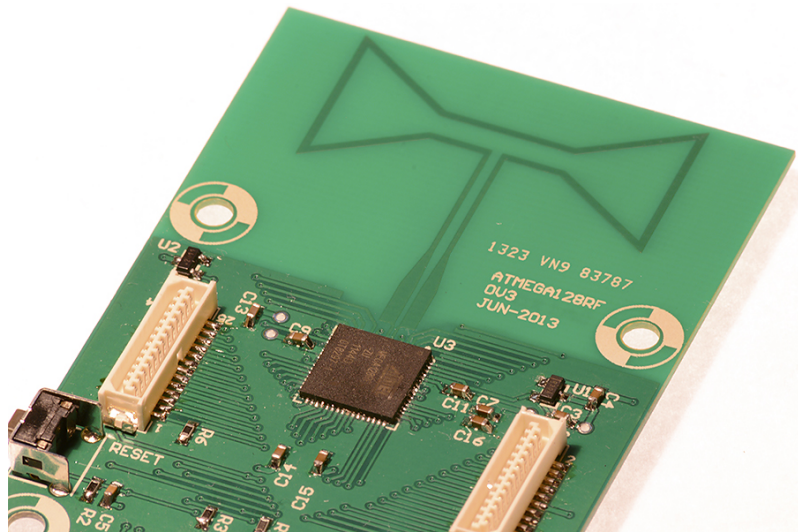


Figure 3.29: Prototype node including bowtie-shaped folded dipole, built by the manufacturer, following the proposed design

The following chapter studies balun solutions capable of providing differential impedance measurements of the input impedance of the chosen antenna.

# Chapter 4

## Microstrip to balanced dipole transition design and measurement

### 4.1 Introduction

In order to measure the impedance of the chosen antenna a microstrip to coplanar stripline transmission should be designed. Common used solutions include baluns and test-fixtures. For this reason this chapter aims at designing two microstrip balun structures, a commercial integrated ceramic balun solution and finally a test-fixture method. Thus, before designing the baluns, the next section introduces a complete study on baluns characterisation.

### 4.2 Balun characterisation

A balun is a transformer used to convert unbalanced to balanced transmission structures and vice-versa, hence, it is defined as a bidirectional structure. Additionally, baluns can also provide impedance transformation. Baluns are used in a wide range of applications such as radio and television receivers, video and audio processing; and historical reasons determined the most common used impedance for the unbalanced port of baluns as  $50\ \Omega$  or  $75\ \Omega$ . The term derives from "**balanced**" + "**unbalanced**".

An ideal balun (figure 4.1) introduces a  $180^\circ$  phase shift between the balanced ports and  $0\ \text{dB}$  amplitude difference between the unbalanced port and the sum of amplitudes of the balanced ports as figure 4.2 illustrates. However, due to non-ideal characteristics, practically all commercial low-end baluns introduce minor amplitude and phase impairments.

The performance of baluns can be characterised by important specifications: insertion loss, return loss, amplitude and phase balance, common-mode rejection ratio and balanced port isolation. All these parameters are considered during the characterisation of the baluns.

Baluns can be characterised as 3-port networks or 2-port networks, the latter, however, with less precision. An ideal balun represented as a 3-port network ( $s$ -parameters matrix in equation 4.1) can

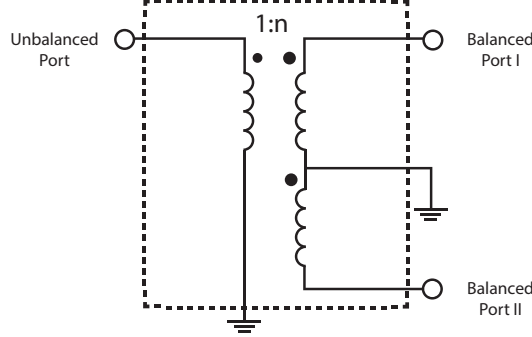


Figure 4.1: Flux coupled balun transformer

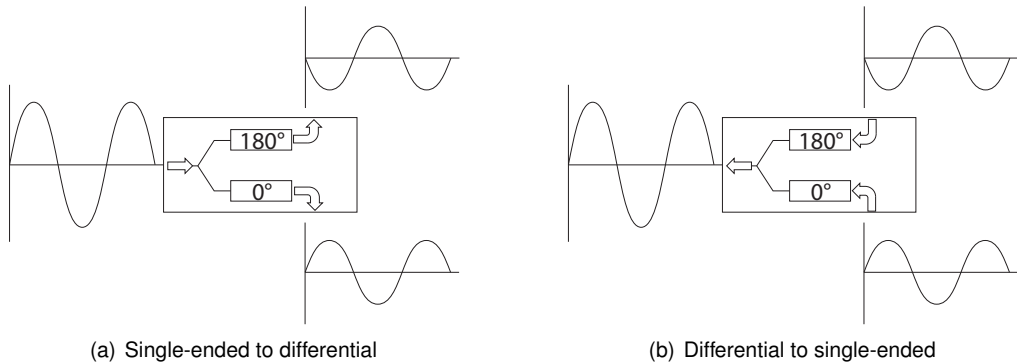


Figure 4.2: Block diagram of signal conversion

be converted to a 2-port network by transforming the two balanced ports into one logical port, which creates a common-mode and differential-mode on the logical port. This conversion, frequently called single-mode to mixed-mode conversion, is used to provide a better comprehension on the referred existing modes and easily achieve several performance specifications such as common-mode rejection ratio. Note that throughout this work, port 1 will be referred as the unbalanced port and ports 2 and 3 as the balanced ports.

$$[S] = \begin{bmatrix} s_{11} & s_{12} & s_{13} \\ s_{21} & s_{22} & s_{23} \\ s_{31} & s_{32} & s_{33} \end{bmatrix} = \begin{bmatrix} -\infty & \frac{1}{\sqrt{2}} & -\frac{1}{\sqrt{2}} \\ \frac{1}{\sqrt{2}} & s_{22} & s_{23} \\ -\frac{1}{\sqrt{2}} & s_{32} & s_{33} \end{bmatrix} \quad (4.1)$$

According to [50], and as shown in equation 4.2a, single-ended S-parameters can be converted into mixed-mode S-parameters, represented by  $[S^{mm}]$ . Note that this conversion assumes no existing coupling between the balanced ports.

$$[S^{mm}] = [M][S][M]^{-1} \quad (4.2a)$$

$$\text{where } [M] = \begin{bmatrix} 1 & 0 & 0 \\ 0 & \frac{1}{\sqrt{2}} & -\frac{1}{\sqrt{2}} \\ 0 & \frac{1}{\sqrt{2}} & \frac{1}{\sqrt{2}} \end{bmatrix}, [M^{-1}] = \begin{bmatrix} 1 & 0 & 0 \\ 0 & \frac{1}{\sqrt{2}} & \frac{1}{\sqrt{2}} \\ 0 & -\frac{1}{\sqrt{2}} & \frac{1}{\sqrt{2}} \end{bmatrix} \quad (4.2b)$$

$$[S^{mm}] = \begin{bmatrix} s_{11} & s_{1d2} & s_{1c2} \\ s_{d21} & s_{d2d2} & s_{d2c2} \\ s_{c21} & s_{c2d2} & s_{c2c2} \end{bmatrix} \quad (4.2c)$$

$$= \begin{bmatrix} s_{11} & \frac{1}{\sqrt{2}}(s_{12} - s_{13}) & \frac{1}{\sqrt{2}}(s_{12} + s_{13}) \\ \frac{1}{\sqrt{2}}(s_{21} - s_{31}) & \frac{1}{\sqrt{2}}(s_{22} + s_{33} - s_{32} - s_{23}) & \frac{1}{\sqrt{2}}(s_{22} + s_{23} - s_{32} - s_{33}) \\ \frac{1}{\sqrt{2}}(s_{21} + s_{31}) & \frac{1}{\sqrt{2}}(s_{22} + s_{32} - s_{23} - s_{33}) & \frac{1}{\sqrt{2}}(s_{22} + s_{32} + s_{23} + s_{33}) \end{bmatrix} \quad (4.2d)$$

Note also that  $S_{d21}$  represents the differential response of port 2 to a single-ended stimulus of port 1; and  $S_{1d2}$  represents the single-ended mode response to a differential stimulus of port 2. In the same way,  $S_{d2c2}$  represents the differential response of port 2 when it is stimulated with a common-mode signal.

Considering now the matrices  $[S]$  and  $[S^{mm}]$ , the performance of a balun can be characterised by the following parameters:

### Amplitude and phase balance (AB and PB)

Due to non-ideal characteristics, baluns may not perform optimally when delivering a differential signal on the balanced ports. Thus, a performance specification named amplitude and phase balance determines the balun's capability of creating a perfect differential mode.

According to the equations 4.3 and 4.4, this is calculated using the values from the  $[S]$  matrix.

$$\text{Amplitude Balance} = 20 \log_{10} \left( \frac{|S_{31}|}{|S_{21}|} \right) \text{ [dB]} \quad (4.3)$$

$$\text{Phase Balance} = \text{Ph} \left( \frac{S_{31}}{S_{21}} \right) \text{ [°]} \quad (4.4)$$

Generally, standard microwave baluns have a phase balance of  $\pm 15^\circ$  max and  $\pm 10^\circ$  typical and a amplitude balance of  $\pm 1.5$  dB max and  $\pm 1$  dB typical [51].

### Insertion and return Loss

Insertion loss may be represented by scattering parameters "pairs":  $S_{12}/S_{21}$ ,  $S_{13}/S_{31}$ ,  $S_{23}/S_{32}$ ; however the latest pair is often called balanced port isolation. Typically, baluns do not offer high isolation because they are intended to be matched simultaneous at port 2 and 3 by a resistive impedance. Assuming an ideal balun, the insertion loss from port 1 to 2 and 3 and vice-verse ( $S_{12}/S_{21}$ ,  $S_{13}/S_{31}$ ) is  $1/\sqrt{2}$  (or -3 dB), as a result of theoretical power split.

The ideal balun may be described by the scattering parameters matrix 4.1.

To properly characterise the return loss on ports 2 and 3, the matrix  $[S^{mm}]$  should be considered for both existing mixed-modes. Thus, the return loss performance is evaluated by  $S_{d2d2}$  and  $S_{c2c2}$ .  $S_{d2d2}$  represents the differential return loss, while  $S_{c2c2}$  is the common-mode return loss, in the ideal matrix 4.5

(in dB). Note that, according to the scope of this project, only the differential mode should be considered.

$$\begin{bmatrix} S_{11} & S_{1d2} \\ S_{d21} & S_{d2d2} \end{bmatrix} = \begin{bmatrix} -\infty & 0 \\ 0 & -\infty \end{bmatrix} \quad (4.5)$$

### Common-mode rejection ratio

Frequently, in literature, common-mode rejection ratio is used as a figure of merit of balanced circuits. It is defined as the ratio between differential signal gain/loss and common-mode signal gain/loss and is calculated through the equation 4.6.

$$\text{CMRR} = \frac{S_{1d2}}{S_{1c2}} = \frac{S_{12} + S_{13}}{S_{12} - S_{13}} \quad (4.6)$$

According to [51], typical low performance balun have 15-20 dB of CMRR.

## 4.3 Baluns solutions

The baluns to be designed must have a  $50\Omega$  input impedance to match the SMA connector of the VNA and a  $100\Omega$  (output) differential impedance to match the antenna input. The baluns requirements are listed below.

1. balanced/unbalanced impedance:  $50\Omega / 100\Omega$  (1:2 impedance conversion ratio);
2. frequency coverage: 2.4-2.5 GHz;
3. SMA input connector;
4. same substrate as in the antenna design, FR-4.

The next sub-chapters address four baluns solutions.

### 4.3.1 Printed balun A

A new balun was designed in this project based on the structure presented in [52]. It features a quarter-wavelength transformer (5) followed by a T-junction power divider (4) and finally a difference of half guided wavelength,  $\lambda_g/2$ , between two trace branches in order to introduce a  $180^\circ$  phase shift (2) and, consequently, a differential mode in the coplanar stripline (1).<sup>1</sup> All steps involved in the designed balun are described in the next subsections, according to the diagram in figure 4.3(a) numbering. Figure 4.3(b) depicts the built balun.

---

<sup>1</sup>The numbering in parenthesis represents the designing subsections below, which are illustrated in figure 4.3(a)

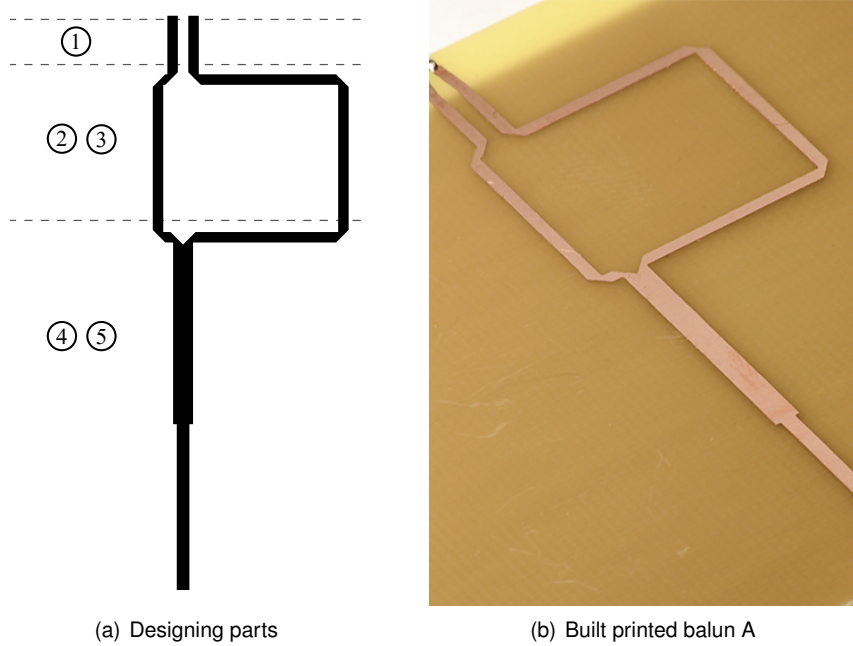


Figure 4.3: Printed balun A

#### 4.3.1.1 Balun design

The complete design of the balun comprehends five parts which are addressed below.

##### 1. Grounded coplanar stripline (GCPS)

To achieve a  $100 \Omega$  differential impedance on the grounded coplanar stripline (figure 4.4) we have used equation 4.7 (see reference[53]), which represents the impedance of a microstrip line (equation 4.8), multiplied by 2 and by a coupling factor.

By fixing  $w = 1.25 \text{ mm}$ , and solving the equation 4.7,  $s = 1.25 \text{ mm}$  was obtained. Note that these coupled microstrip lines have an independent impedance of  $Z_{ms} = 55.7 \Omega$ , according to equation 4.8.

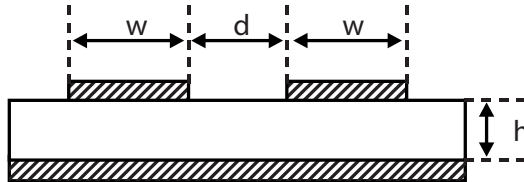


Figure 4.4: Illustration of a grounded coplanar stripline (GCPS) section

$$Z_d = \frac{174}{\sqrt{\epsilon_r + 1.41}} \ln \left( \frac{5.98h}{0.8w + t} \right) \left( 1 - 0.48 \exp \left( -0.96 \frac{d}{h} \right) \right), \quad 0.1 < \frac{w}{h} < 3 \quad (4.7)$$

$$Z_0 = \frac{87}{\sqrt{\epsilon_r + 1.41}} \ln \left( \frac{5.98h}{(0.8w + t)} \right), \quad 0.1 < \frac{w}{h} < 3 \quad (4.8)$$

##### 2. Phase shift branches

Two microstrip line branches were inserted in the balun structure in order to provide a  $180^\circ$  phase shift. This means that a path difference of  $\lambda_g/2 = 17.25$  mm had to be created (see equations 4.9 and 4.10 [53]). An illustration of the microstrip structure is shown in figure 4.5 with the respective designing parameters.

$$\varepsilon_{eff} = \frac{\varepsilon_r + 1}{2} + \frac{\varepsilon_r - 1}{2} \left( 1 + 12 \left( \frac{h}{w} \right) \right)^{-1/2}, \left( \frac{w}{h} \right) \geq 1 \quad (4.9)$$

$$\lambda_g = \frac{\lambda_0}{\sqrt{\varepsilon_{eff}}} \quad (4.10)$$

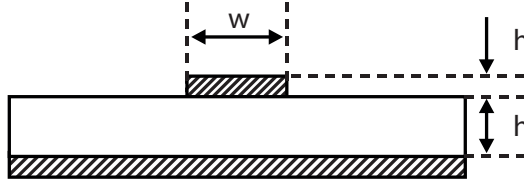


Figure 4.5: Side-cut illustration of a microstrip line

### 3. Bends in microstrip lines

Microstrip bends are one of the most encountered discontinuities structures. They may vary from a simple  $90^\circ$  to a curving line bend. In this balun design the chosen option was mitered bends illustrated in the figure 4.6, leading to optimal performance in terms of reflection. According to [54] the optimal parameters can be calculated from the equations 4.11, 4.12. Figure 4.6 illustrates the designing parameters used. As calculated previously the width of the microstrip is  $w = 1.24$ mm.

$$d = w\sqrt{2} \quad (4.11)$$

$$x = d(0.52 + 0.65e^{-1.35(w/h)}) \quad (4.12)$$

Solving the equations, it was obtained  $x = 1.497$  mm and  $d = 1.767$  mm.

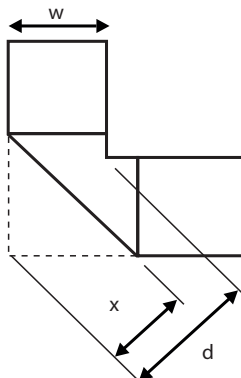


Figure 4.6: Bend design parameters

#### 4. T-Junction microstrip power divider

Power dividers are also common discontinuities present in microwave devices. The goal is either to divide the power from one source or to combine the power from two sources. They are normally represented as a 3-port network by the general equations 4.13. Moreover, the equation 4.13b is only valid if the power is split evenly.

Throughout this work, port 1 is defined as the port responsible to split the power and ports 2 and 3 responsible to combine the power, as figure 4.7(a) illustrates.

$$|S_{11}|^2 = 0 \quad (4.13a)$$

$$|S_{21}|^2 = |S_{31}|^2 \quad (4.13b)$$

$$|S_{11}|^2 + |S_{21}|^2 + |S_{31}|^2 = 1 \quad (4.13c)$$

$$|S_{21}| = |S_{31}| = \frac{1}{\sqrt{2}} \quad (3 \text{ dB}) \quad (4.13d)$$

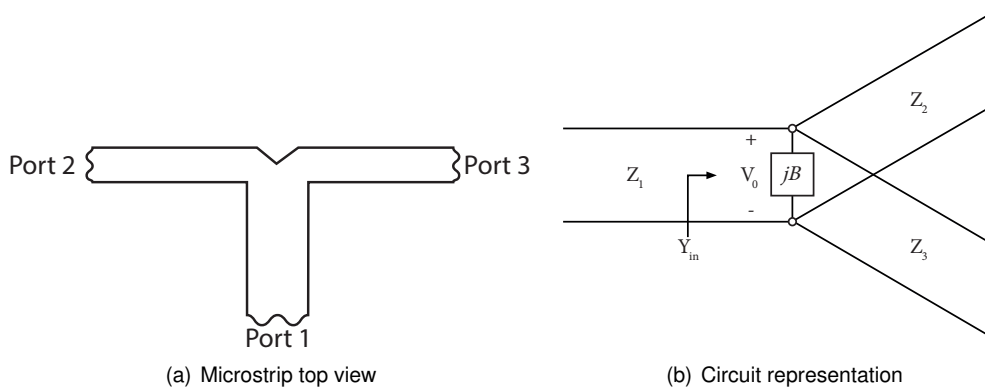


Figure 4.7: T-Junction power divider

Image 4.7(b) clarifies the impedance transformation, which is analytically obtained according to equation 4.14.

$$Y_{in} = jB + \frac{1}{Z_1} + \frac{1}{Z_2} = \frac{1}{Z_0}. \quad (4.14)$$

Assuming that losses are negligible (ie,  $B = 0$ ) the impedance of the unbalanced port is solved in equation 4.15b.

$$\frac{1}{Z_1} + \frac{1}{Z_2} = \frac{1}{Z_0}. \quad (4.15a)$$

$$Z_0 = \frac{Z_1}{2} = \frac{Z_2}{2} = \frac{Z_{ms}}{2} = 27.91 \Omega \quad (4.15b)$$

## 5. Quarter-wavelength impedance transformer

To accomplish the conversion of  $27.91 \Omega$  to  $50 \Omega$  (to match the SMA connector), a quarter-wavelength impedance transformer was designed. Assuming that the impedance transformation is performed according to equation 4.16,

$$Z_{in} = \sqrt{Z_0 Z_{out}} \quad (4.16)$$

and,  $Z_{in} = 50 \Omega$ , and  $Z_{out} = 27.91 \Omega$ ,  $Z_0$  is obtained.

$$Z_0 = 37.36\Omega \quad (4.17)$$

Hence, according to equation 4.8, the width of a  $37.36 \Omega$  microstrip is 2.1 mm and, according to equation 4.10, a length equal to  $\lambda_g/4 = 16.7$  mm. The final microstrip line has the impedance of  $50 \Omega$  and a width of 1.5 mm.

See Appendix A for mechanical dimensions of the balun.

### Design aspects and considerations

Note that this balun is basically a microstrip to ground coplanar stripline (GCPS). However, the chosen antenna is fed by a coplanar stripline, hence, some losses are originated. Refer to the experimental results of this balun for further info on these losses.

This balun design has a narrow band due to designing parts 2 and 5 which are directly related to the frequency. For this reason this balun was designed to achieve optimal behaviour at 2.45 GHz, thus, the balun should perform satisfactorily within a close frequency range.

#### 4.3.1.2 Simulations results

To confirm the analytic based design of the balun an EM simulation was performed. Satisfactory good results were achieved but a software-optimization had to be made in order to fine tune the structure parameters. The optimisation to reduce the phase/amplitude balance and return/insertion loss at 2.45 GHz shows an enhancing of 20 dB, as illustrated in figure 4.8(a),

As mentioned earlier in this chapter, the performance of a balun is also characterised by the amplitude and phase balance, and common mode rejection ratio.

Equations 4.3 and 4.4 for the amplitude and phase balance calculation, are illustrated in simulation curves of figure 4.9. Please note that the values for the insertion losses from port 1 to port 2 and 3, represented by  $S_{21}$  and  $S_{31}$  in figure 4.8(b), show apart the 3 dB loss (see 4. Power Divider in the previous subsection), an extra loss of 0.25 dB and 0.47 dB, respectively, for 2.45 GHz.

Although not illustrated the curve for common-mode rejection ration, this value, according to equation 4.6, equals to CMRR = 77.43 dB at 2.45 GHz.

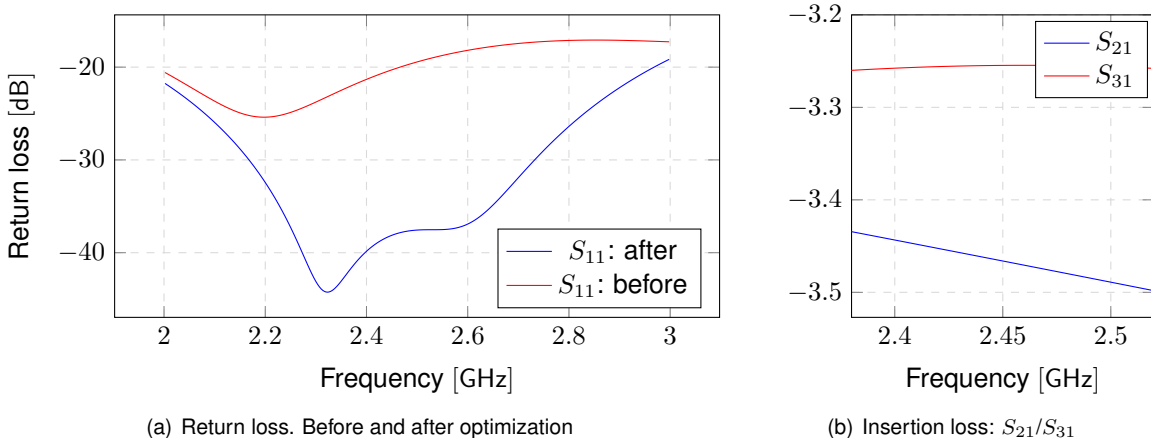


Figure 4.8: Balun A s-parameters

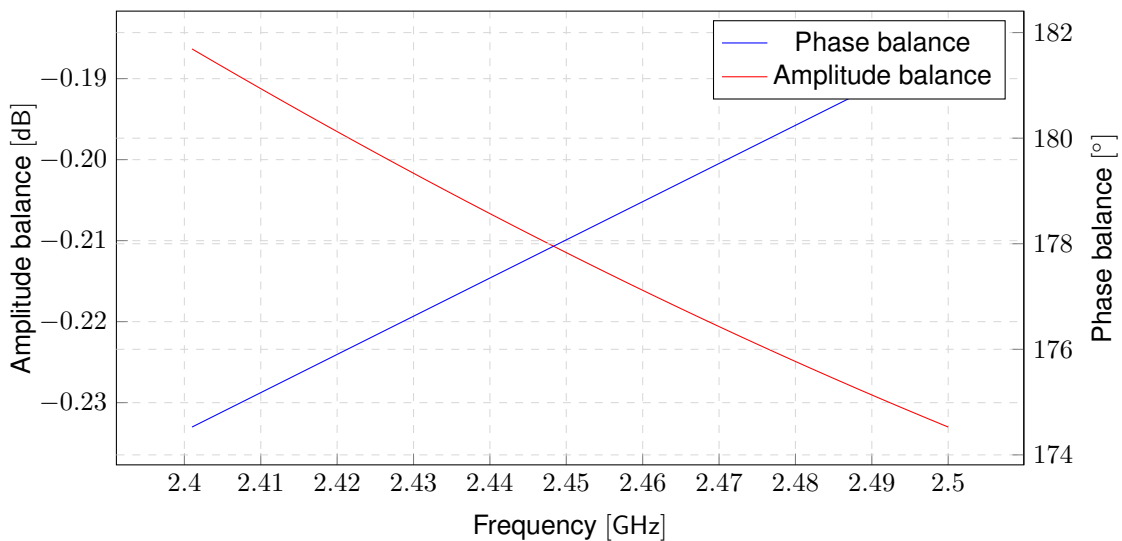


Figure 4.9: Balun A amplitude and phase balance

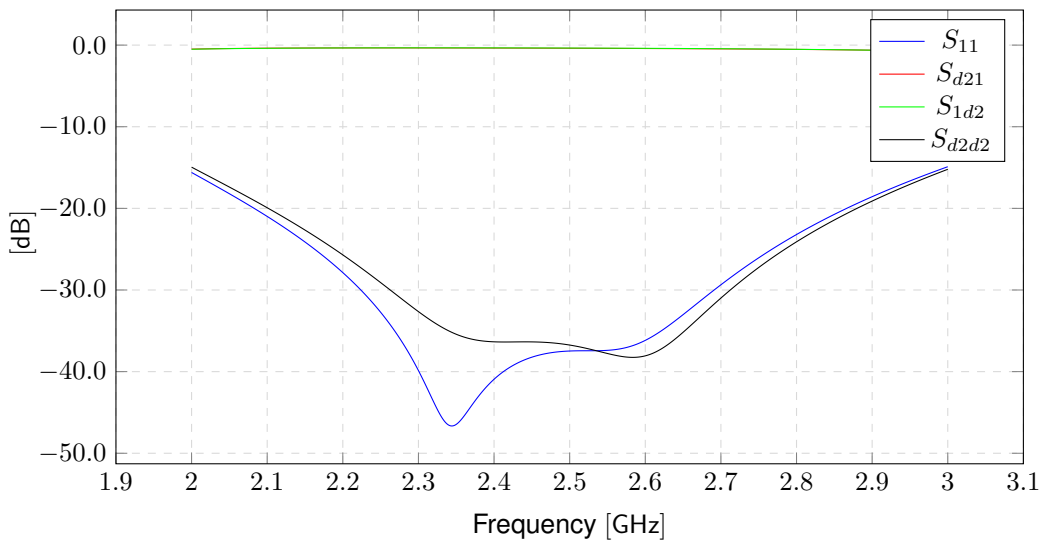


Figure 4.10: Balun A differential mode (mixed mode) s-parameters

### 4.3.1.3 Experimental results

In order to experimentally characterise this balun two measurements had to be performed in two specifically designed printed setups; one for the insertion loss and another for the return loss. The first board (Balun A IL test board in figure 4.11(a)) was designed to measure the return loss, and the latter (Balun A RL test board in figure 4.11(a)) was designed to measure the insertion loss.

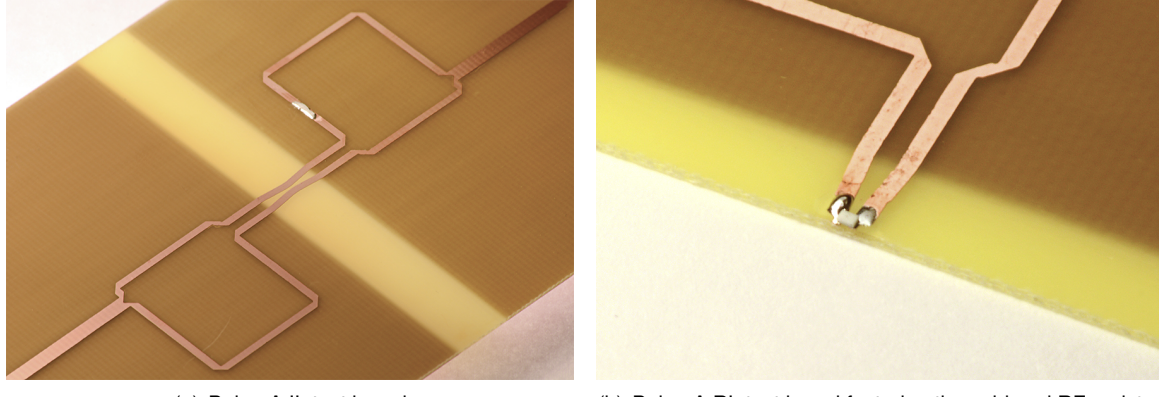


Figure 4.11: Test boards for measuring insertion and return losses

The Balun A IL test board (4.11(a)), is basically a back-to-back printed configuration of the Balun A. This mounting allows to obtain the insertion loss of the individual balun by dividing the insertion loss of the designed setup by 2. However, as shown in figure 4.11(a), a CPS gap is introduced between the baluns in order to characterize the losses caused by the  $100 \Omega$ -GCPS to  $100 \Omega$ -CPS transition of the final antenna measurement design in the chapter 5.

The Balun A RL test board (4.11(b)) was built in order to measure the return loss. However, like the IL test board, it has a GCPS-CPS transition in order to characterise the above mentioned transition. CPS extension is connected to a 100 Ohm resistor to match its characteristic differential impedance, thus allowing the measurement.

The insertion and return losses curves presented in figure 4.12 and 4.13 show a comparison of the experimental measurement with the simulation results. As expected, due to the sudden GCPS to CPS transition, there is an increase of the insertion loss of approximately 0.5 dB which should not introduce considerable errors in the final measurements of the antenna. Note the fair agreement between simulation and measured return loss results.

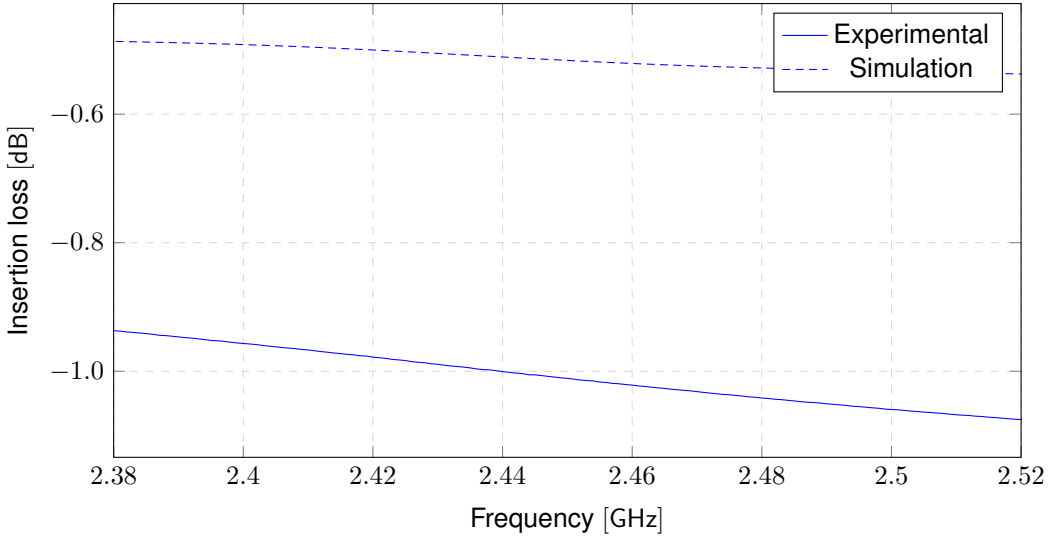


Figure 4.12: Balun A insertion losses comparison

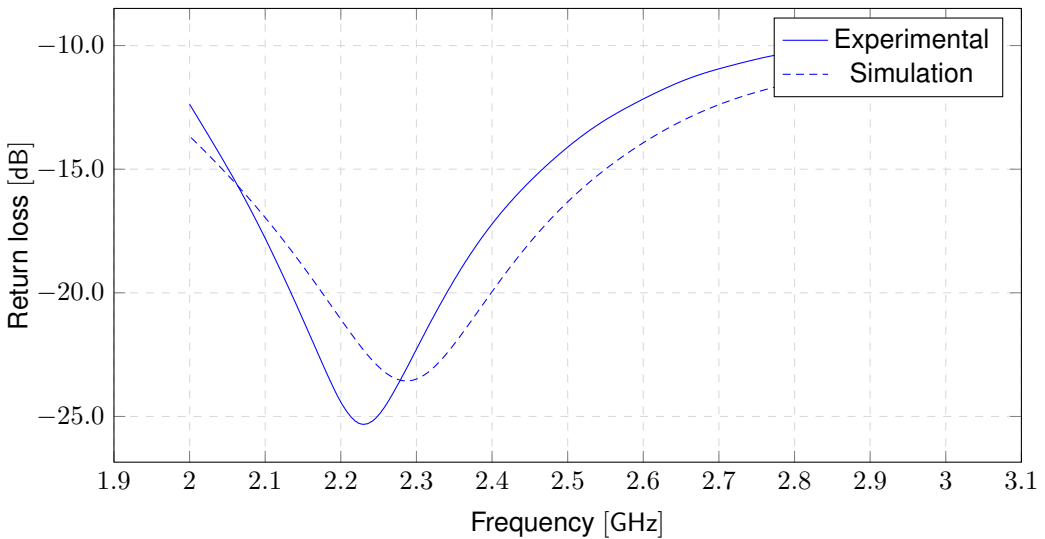


Figure 4.13: Balun A return losses comparison

#### 4.3.1.4 Conclusions

Although this balun was created to determine a measurement of impedance of the proposed antenna, the fact that it has a CPS feeding point may suggest an impedance mismatch between the two structures (balun and antenna); which is caused by a sudden GCPS-CPS transition structure, as shown in 4.3(b).

To test this hypothesis, a simulation of the transition (figure 4.14) was performed. Moreover, to eliminate the losses of substrate and cooper, the lossy dielectrics were simulated as loss-free and the lossy metals as perfect electric conductors (PECs). The insertion loss, in a range of 2.4-2.5 GHz, was between -0.27 dB and -0.35 dB; while the return loss was between -15.15 dB and -14.21 dB. Theoretically these are high values when compared to a normal CPS or GCPS which are practically 0 dB for the insertion loss and less than -40 dB for the return loss.

This balun concept may not optimally perform in this project conditions; however, when using a substrate with high dielectric permittivity (e.g.  $\epsilon_r > 10$ ) and when closing the gap of the GCPS, the

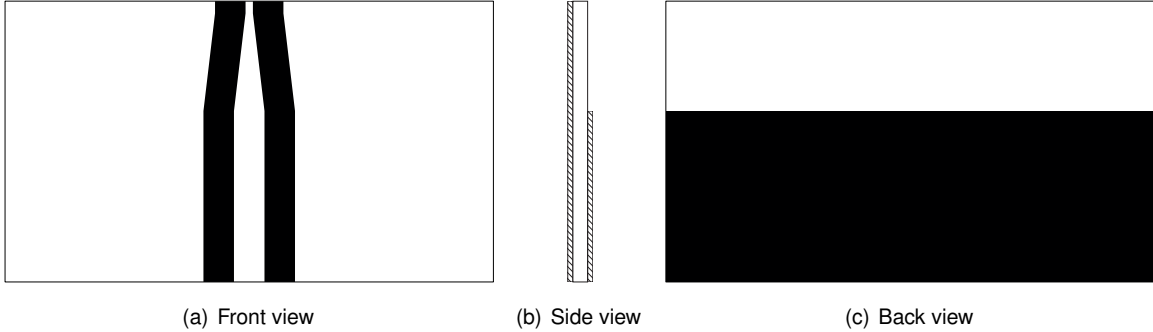


Figure 4.14: GCPS-CPS transition segment of Balun A

results tend to improve due to less GCPS dependency on the ground plane dimensions [55]. Hence, making the EM fields in the actual GCPS-CPS transition a lot smoother.

Despite not being perfectly suited to measure this antenna, the balun is optimally designed to measure other balanced antenna structures which must have a supporting ground plane or only feed by a GCPS.

#### 4.3.2 Printed balun B

A new design for a printed balun is presented, based on the concept of [56]. It consists in a microstrip fed structure, which is combined with a via structure to create a differential mode between points 1 and 2 (figure 4.15). The via structure allows point 2 to have  $180^\circ$  phase difference to point 1, as described in the above mentioned reference. As in the mentioned reference, this structure was optimized leading to best results for the 2.45 GHz frequency.

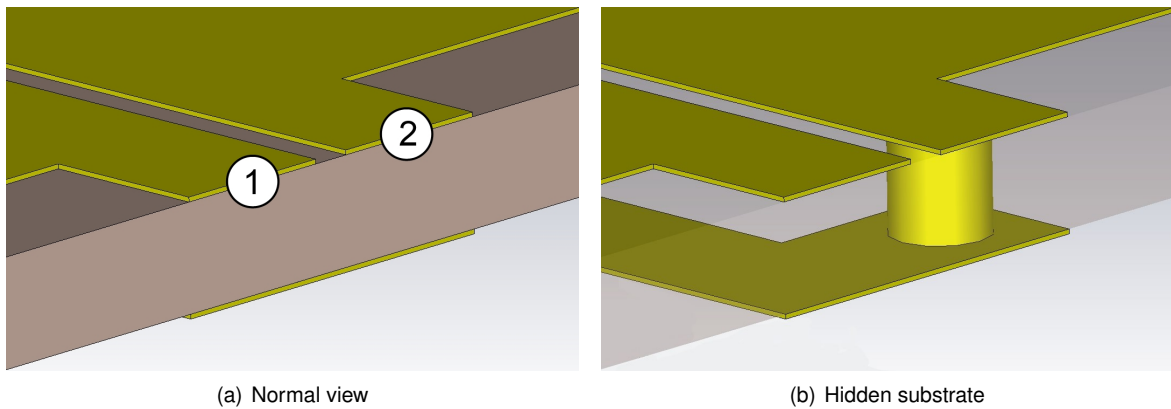


Figure 4.15: Via structure in detail

To better understand the balun behaviour, a sequence of magnitude of the electric snapshot in time is shown in figure 4.16, where the blue colour represents the negative values of the electric field while the red the positive values. Note that at the snapshot corresponding "phase =  $0^\circ$ ", there is in the microstrip line, an opposite ("negative") direction E-field component travelling towards the antenna in the microstrip line. At  $90^\circ$ , the E-field front is already travelling through the via structure while the ground

plane remains at "positive" orientation. At  $135^\circ$ , it is possible to see the "negative" electric field front travelling in the antenna, while a "positive" electric field appears at the beginning of the microstrip. The behaviour remains unaltered for positive values, as seen in  $180^\circ$  and  $225^\circ$ .

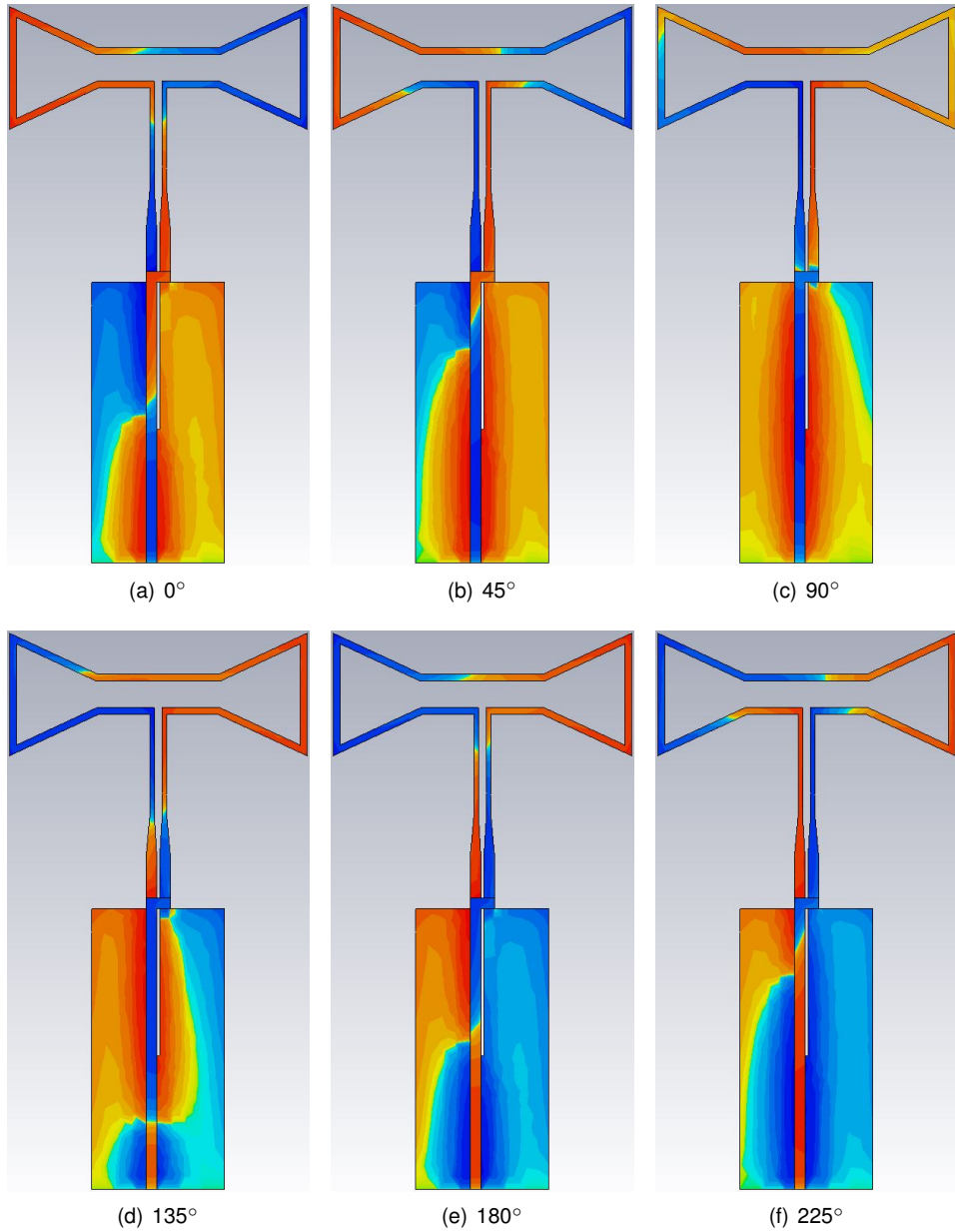


Figure 4.16: Sequence of snapshots of the Balun B including the proposed antenna

See Appendix A for mechanical dimensions of the balun.

#### 4.3.2.1 Simulations results

The simulation results are presented in the figure 4.17. As it is shown the return loss and insertion loss are near optimal values thus making it a good method for measuring this specific antenna. Due to software limitations, it was not possible to simulate neither the amplitude and phase balance nor the CMRR. However, this balun should perform better than the previous balun design (Balun A) because

its currents in the actual transition are less dependent of the ground and it is a true microstrip-CPS transition.

Although experimental differential impedance results are presented in chapter 5, no experimental results on the actual balun were performed due to its complex transition.

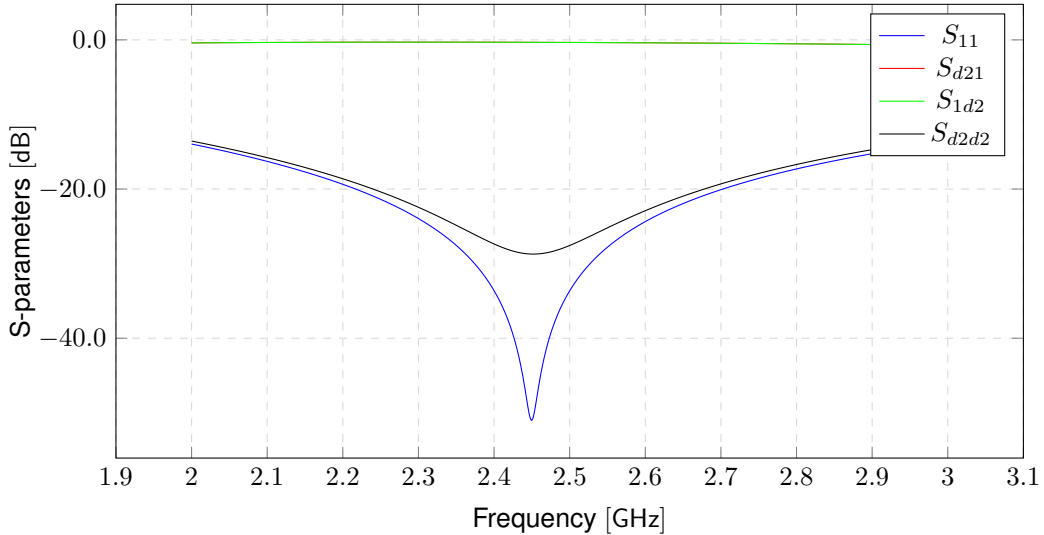


Figure 4.17: Balun B S-parameters - differential mode (mixed mode)

### 4.3.3 Integrated passive ceramic balun

This section aims to characterise an integrated ceramic balun (figure 4.18) by measuring its s-parameters with a VNA. Despite the fact that the manufacturer provides the s-parameters of the balun, it was decided to characterise the ordered balun to prove the good performance exhibited in the datasheet [57].

As introduced in the beginning of this chapter, a balun can be characterised as 2-port device or as 3-port device. Both of these methods will be applied on this structure.



Figure 4.18: Johanson Ceramic Balun

The datasheet specifications for this particular model, a Johanson Technology Inc. (JTI) model 2450BL15B100, are listed below.

1. Unbalanced Impedance:  $50 \Omega$
2. Balanced Impedance:  $100 \Omega$

3. Insertion Loss: 1.0 dB max.
4. Return Loss: 9.5 dB min.
5. Phase Difference:  $180^\circ \pm 10^\circ$
6. Amplitude Difference: 2.0 dB max

The return and insertion loss curves presented on the datasheet reveal significant good results for the desired operating frequency regarding both losses. These curves will be compared with experimental measurements obtained through two characterisation methods described in the next section.

#### 4.3.3.1 Two-port characterisation method

This method only allows to characterise the insertion and return loss by performing two measurements on the built test boards, similarly to the performed for the printed balun A (see section 4.3.1). The first test board (IL test board) represented on figure 4.19 was used to obtain the insertion loss, where two baluns are mounted in a back-to-back configuration. The insertion loss of the IL test board is, after being measured, divided by 2 which are presented and compared with the datasheet in figure 4.20. The insertion loss calculated in the 2.4 - 2.5 GHz range frequency is approximately -0.5 dB which is close to the value referred to by the manufacturer. Note that the experimental results confirmed an equal insertion loss from one port to the other ( $S_{21} = S_{12}$ ) due to the board's symmetry.

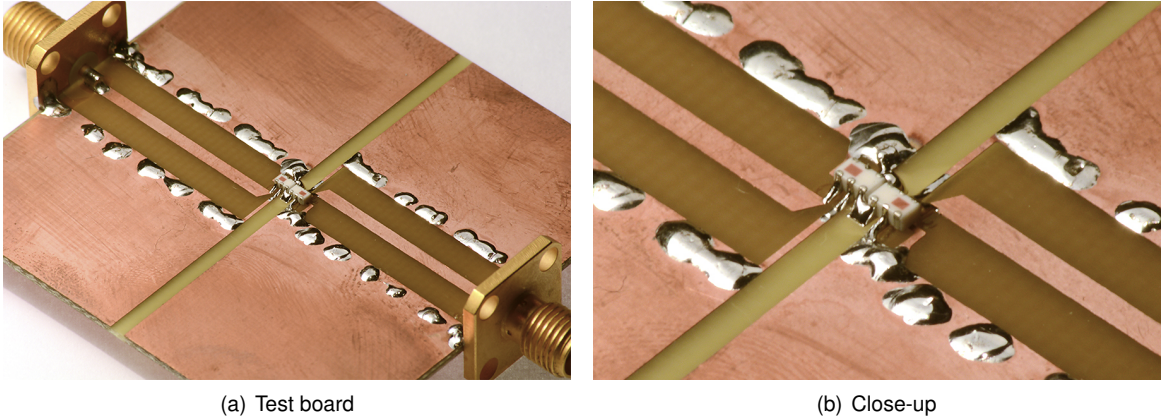


Figure 4.19: Insertion Loss test board for measuring insertion loss

The drawback of this measurement is the fact that the baluns are perfectly matched when placed in a back-to-back configuration which may result in unrealistically good values [58].

Another test board (figure 4.21) was used to measure the return loss (RL). This board consists in a configuration where the balanced ports of the balun are matched by resistive load of  $100 \Omega$  (high frequency resistor), depicted in detail in the close-up image of figure 4.21(b). Note that it is assumed that the resistor has indeed  $100 \Omega$  impedance with 2% tolerance [59].

The measured results shown in figure 4.22 reveal that the return loss "dip" is shifted to approximately 2.58 GHz against the expected 2.4 GHz. Also a significant difference of -15 dB is observed. This may

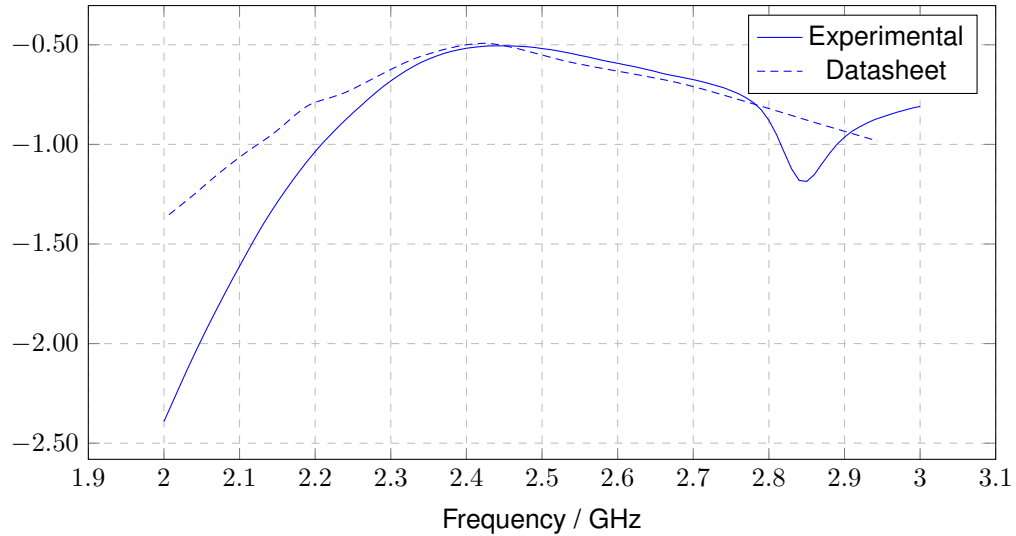


Figure 4.20: Insertion Loss test board: S-Parameters

suggest the hypothesis that the reported 2:1 impedance conversion ratio may not be guaranteed at 2.45 GHz. To prove it and confirm the insertion loss measured results through the IL test board, a three-port measurement is described in the next section.

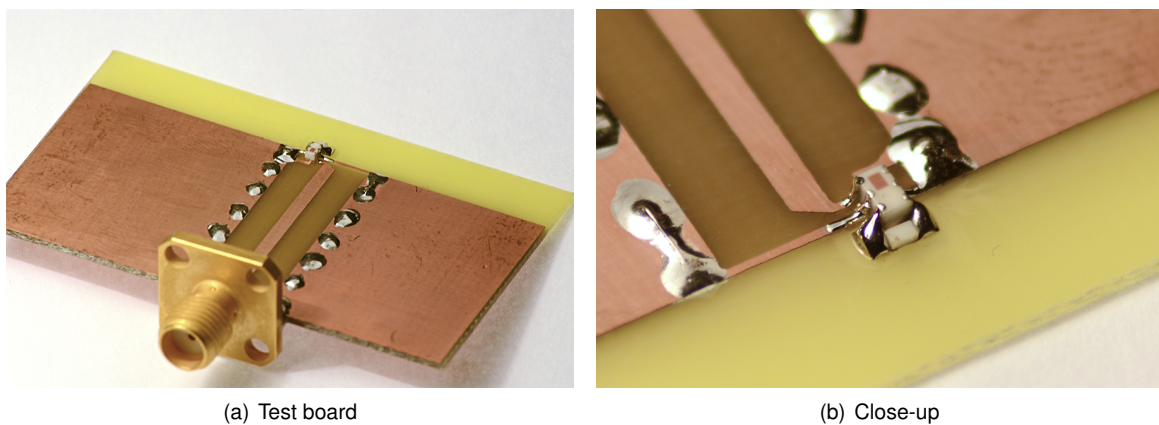


Figure 4.21: Return loss test board for measuring return loss

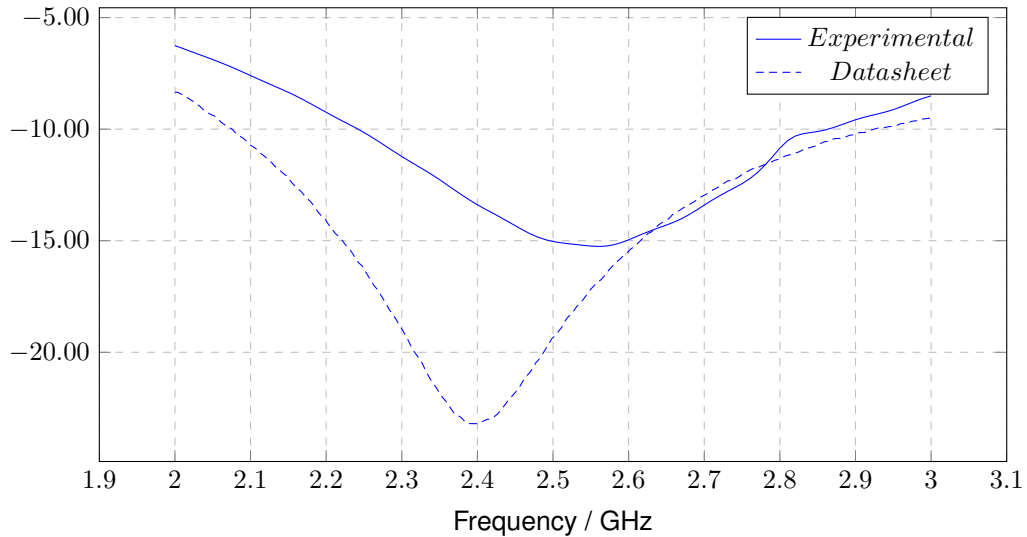


Figure 4.22: RL test board return loss

#### 4.3.3.2 Three-port characterisation method

Three-port characterisation, as the name suggests, is a method for measuring precisely baluns using simultaneously three ports from a VNA and provides s-parameters of a 3-port network structure, contrary to the method described before which only shows the differential return losses,  $S_{11}$  and  $S_{d2d2}$ , and insertion loss,  $S_{1d2}$  and  $S_{d21}$ . The test board (3P board) is illustrated in figure 4.23.

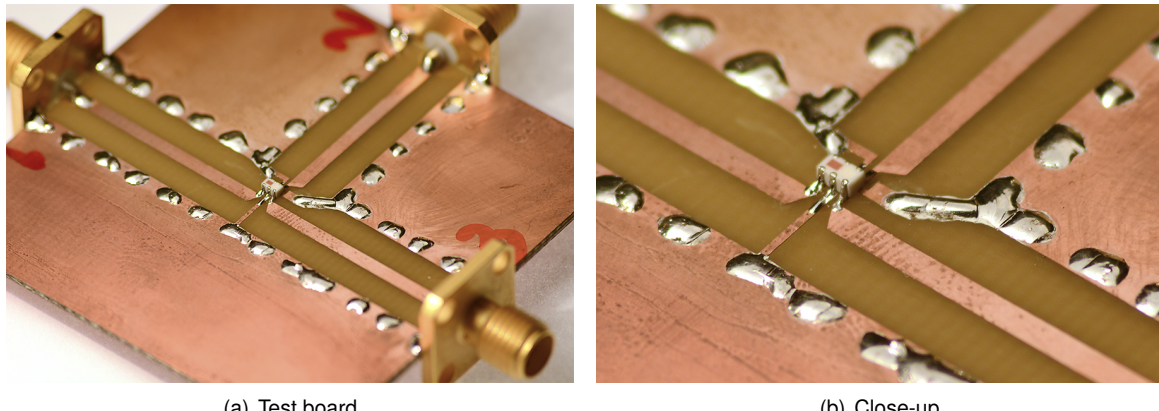


Figure 4.23: 3-port (3P) test board

To proceed the measurements, the 3P board was connected to a VNA and a single-mode S-parameter matrix (equation 4.1) was obtained. This setup allows to measure and calculate: amplitude and phase balance, insertion and return losses of the three ports and CMRR.

As explained in section 4.2, the s-parameters of interest to calculate the AB and PB are  $S_{21}$  and  $S_{31}$  through equations 4.3 and 4.4. The amplitude balance range from 0.12 dB to 0.15 dB, while the phase balance range from 0.2° to 0.4° which are within the expected datasheet values. The obtained result curves are compared with datasheet in figure 4.24.

The resulting curves for the insertion and return losses calculated by performing the single-mode to

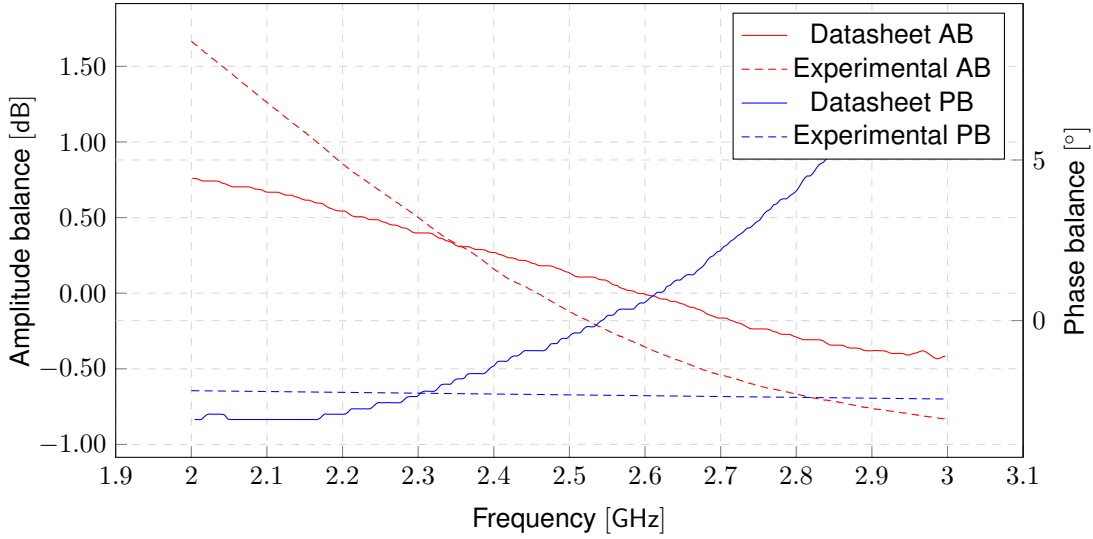


Figure 4.24: Ceramic chip balun amplitude and phase balance

mixed-mode conversion are presented in figure 4.25. It is assumed during this conversion that there is not coupling between the microstrip lines shown in the close-up figure 4.23(b). Measured curves of  $S_{11}$  and  $S_{d2d2}$ , exhibit a "dip" in return loss at 2.59 GHz, which frequency is near the "dip" obtained with the RL test board. This fact corroborates the previous hypothesis that the impedance conversion ratio may not be guaranteed at 2.45 GHz. Although the values declared by the manufacturer for return loss are guaranteed ( $RL > 9.5$  dB) this may not be an optimal solution to measure the differential impedance of the chosen antenna.

However, at 2.45 GHz the return loss is close to -17 dB which overall represents a good value. At this same frequency, the insertion loss is -0.59 dB which is similar to the value obtained with IL test board.

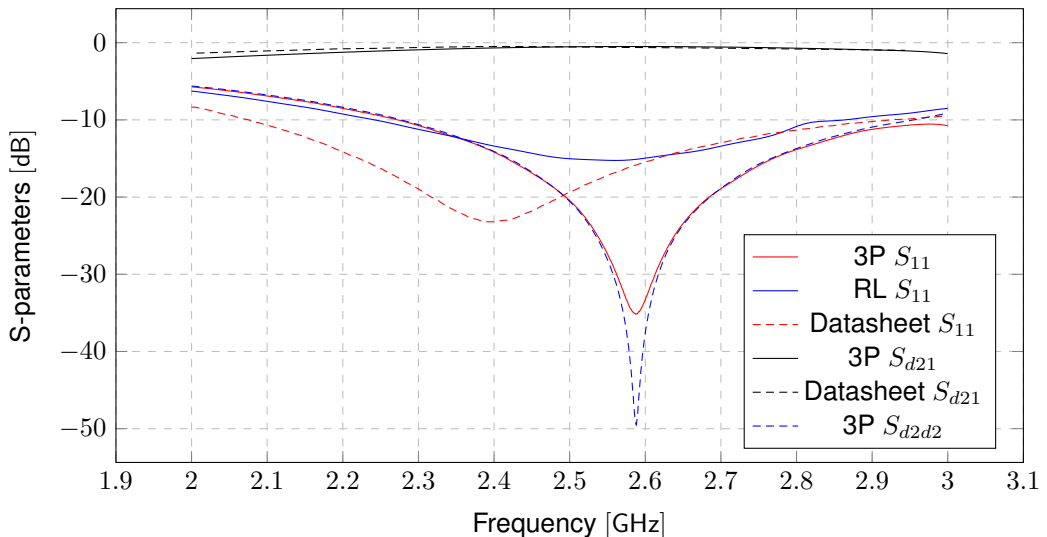


Figure 4.25: 3P test board differential mixed-mode converted s-parameters

#### 4.3.3.3 Extension port calibration

To characterize and confirm the balun solutions in the simulation package chosen (*CST MWS*), an extension port operation was performed in order to move the calibration plane from the SMA connectors of the IL/RL/3P test boards to the pads of the integrated balun through a "Short response calibration" [60] with the available Agilent VNA. This "eliminate the reflection tracking error from the test setup reflection using that port", according to the cited application note.

Thus, in order to create a proper test fixture, a line of  $50 \Omega$  was designed with the same length as the one used in the previously presented test boards. The test fixture features two ground planes separated from the microstrip line by of "four time the dielectric thickness", which reduce the parasitic effects of copper to "less than 1%" according to [61]. Via structures were also implemented in intervals of  $\lambda_g/8$  [62] in order to "achieve better impedance and loss characteristics as well as for suppressing parasitic wave modes" [63].

The test fixture was tested before built. By performing a simulation of the test fixture designed with the chosen software and combining its results with the Touchstone file of the balun (s3p file) obtained through the Johanson Inc the embedding results (*CST Design Studio*) were obtained. The results confirm that the test fixture performs at the range of 2.4 - 2.5 GHz introducing 2.5 dB of in the return loss and 0.3 dB of insertion loss. Thus, by performing the experimental calibration method mentioned before, this balun should provide a true shift of the calibration plane to the pads of the integrated ceramic balun. The embedding setup is presented in figure 4.26 and a 3D model of the simulated test fixture in figure 4.27.

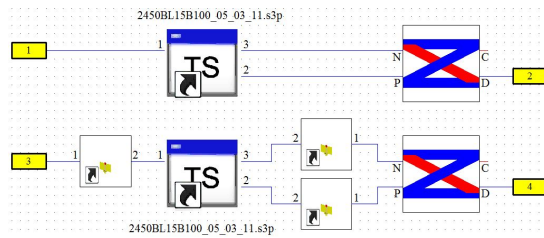


Figure 4.26: CST Design Studio software embedding setup

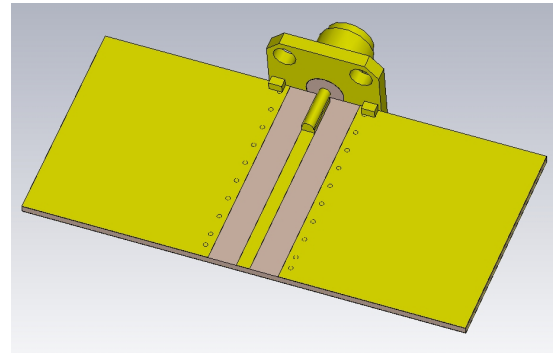
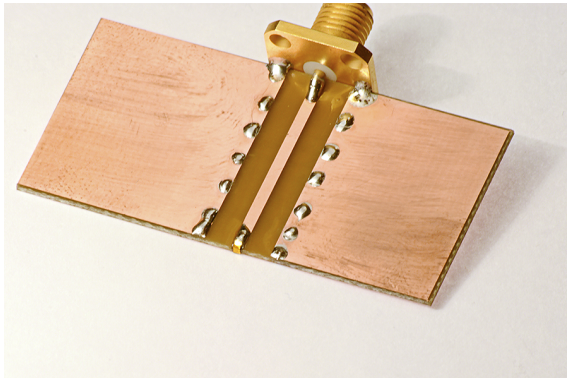


Figure 4.27: 3D model of the designed test fixture

Experimentally, the short calibration was accomplished by "shunting" the microstrip line to its ground using a golden sheet, as depicted in figure 4.28(b), and performing the procedure of the reference [60].



(a) Test fixture



(b) Test fixture featuring the soldered golden sheet in its edge

Figure 4.28: Short calibration test fixture

## 4.4 Test fixture

As mentioned in the beginning of this chapter, the current methods for measuring balanced antennas combine two major structures: a balanced antenna (also called Device Under Test) and a balun/test fixture. However this combination introduces losses due to impedance mismatch, copper and substrate losses and, the most undesired effect, radiation.

These unwanted effects or so called network errors can be removed by performing a measurement calibration to error-correct the network. The most common known techniques include port extensions, TRL/SOLT calibration algorithms and S-parameters de-embedding. In fact, as detailed in the section before, it was made a Agilent Automatic Port Extension, which provided a method for "removing" the delay and loss of the fixture using a short measurement. By using this calibration technique the calibration plane was shifted from the SMA connectors to the pads of the integrated balun.

There are plenty of calibration algorithms such as SOLT (Short-Open-Load-Thru) or TRL (Thru-Reflect-Line) families that require specific application-level calibration kits. Figure 4.29 illustrates a TRL calibration kit for USB 3.0 Std-A and Std-B connectors [64]. However, these techniques require measuring expertise that was not available at the time of this work. This section addresses one of the three mentioned calibration techniques: the extension port which requires a test fixture.

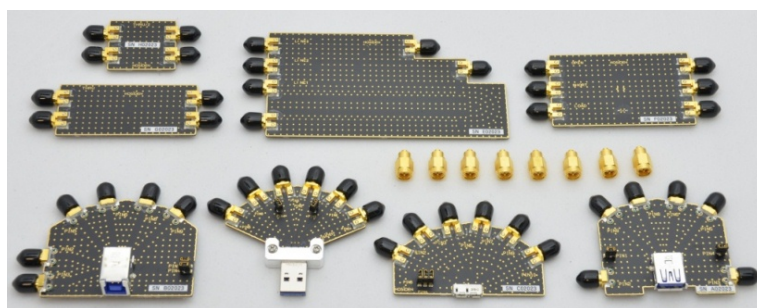


Figure 4.29: Thru-Reflect-Line calibration boards for High Speed USB 3.0 Std-A/Std-B connectors [64]

A test fixture, also called in the literature as jig, is designed according to the concept of [65] (figure 4.30) to provide impedance characterisation on balanced antennas.



Figure 4.30: Test fixture [65]

The fixture consists in two EZ-141 semi-rigid cables connected to Subminiature version A (SMA) connectors at the end of each one, while each other ends are soldered.

However, according to the cited reference, it does not provide information about how the length of the cables (soldered or non-soldered parts) were designed. Moreover, in the literature there are several authors [66] [67] [68] [69] (figure 4.31(b)) [70] (figure 4.31(a)) proposing similar fixtures using the same technique but with different lengths for the same frequency range (500-1500 MHz). In fact, in [71] is presented an identical jig, which does not reveal its true length and furthermore citing that "length of these cables, as well as the tips of these probes must be the same to reduce calibration error" and "the impact from the test fixture can be minimized" using the de-embedding solution built-in the VNA. Thus it is assumed that the length of the jig does not have a significant impact on the final measurements.

Furthermore, in [68], is explicitly mentioned that, this fixture measurement is "difficult to replicate in successive calibration measurements resulting in slightly different results for the same cable".

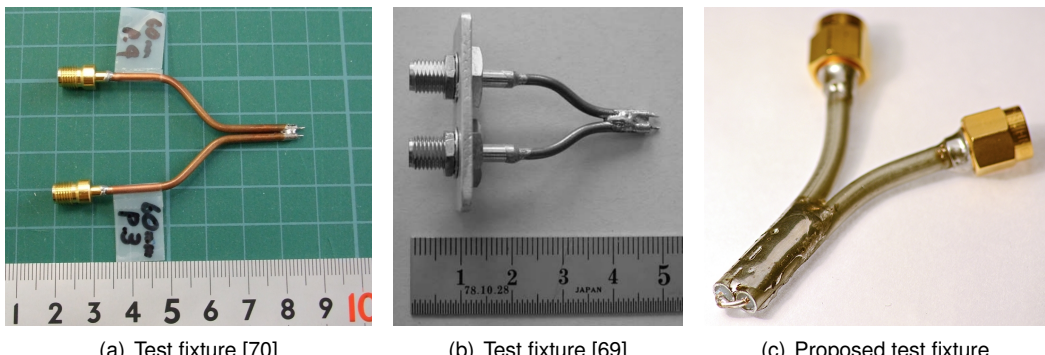


Figure 4.31: Test fixtures with different semi-rigid coaxial cable lengths

The process of removing the effects of the external test fixture such as delay due to length dielectric medium and losses in the copper of the coaxial cables, requires an extension port calibration which was also used for characterising the integrated passive ceramic balun.

In this case, the extension port objective is to move the calibration plane to the antenna feeding point plane (extended calibration plane), as illustrated in figure 4.33. Moreover, as in [68], to achieve a better short calibration, an aluminium sheet was wrapped around the coaxial inner conductors to prevent radiation. The image 4.32 illustrates the fixture with inner conductors soldered but without the aluminium sheet.

The measuring method consists in 3 major steps: performing the extension port calibration referred above, measuring the two-port S-parameters, and calculate the impedance using the equation 4.18.



Figure 4.32: Test-fixture short circuited

$$Z_d = \frac{2Z_0(1 - S_{11}S_{22} + S_{12}S_{21} - S_{12} - S_{21})}{(1 - S_{11})(1 - S_{22}) - S_{21}S_{12}} \quad (4.18)$$

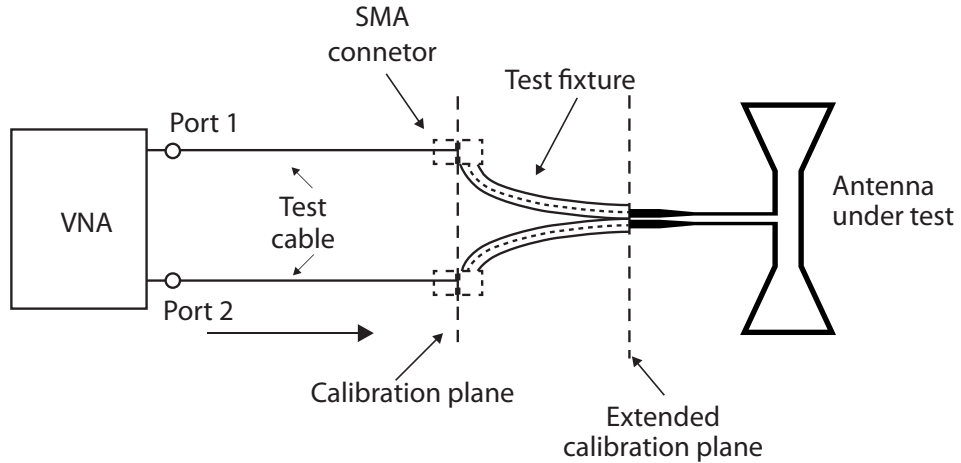


Figure 4.33: Mounting setup for the test fixture including the BSFD antenna. Adapted from [65]

## 4.5 Conclusions

In this chapter four possible solutions were designed to measure the impedance of the proposed antenna.

The first two are printed baluns (Balun A, Balun B) which have the advantage of reproducibility due to being actual printed circuits. They also provide satisfactory performance as described in its section. However, it is expected a better performance of balun B, relatively with balun A, because it features an excellent microstrip-CPS transition concept.

The third balun A, an integrated commercial solution, is characterised by performing two and three-port measurement methods. The curve of coefficient reflection (return loss) in both methods is not the expected according to the manufacturer datasheet. However, all the minimum specifications are guaranteed.

The fourth solution presented is a test fixture. The combined structure (test-fixture plus antenna) results are presented in the chapter 5 as this method does not provide previous performance curves as stated in [68]

# Chapter 5

## Proposed antenna characterisation

### 5.1 Introduction

This chapter includes the actual impedance measurements of the combined structure, balun plus antenna. The results of the proposed antenna as well as a comparison of its radiation pattern with the studied chip and whip antennas are presented. Moreover the radiation patterns measurement setup allows a relative comparison of the radiated power by each antenna.

### 5.2 Impedance measurement results

In order to obtain the impedance of the antenna, the proposed balun/test fixture structures studied had to be combined with actual antenna. Thus, four setup boards were built including the Balun A (figure 5.1), Balun B (figure 5.2), Integrated passive ceramic balun (figure 5.3) and, finally, the test fixture (figure 5.4).

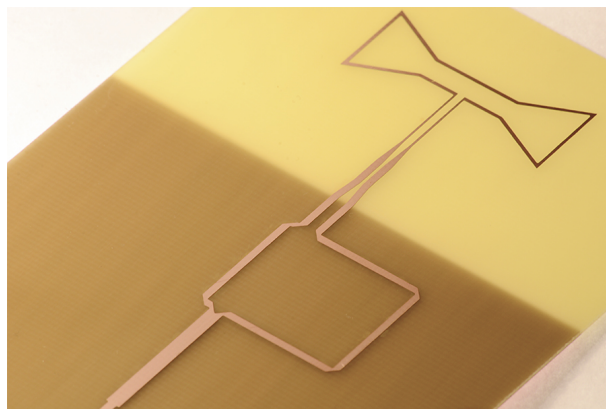
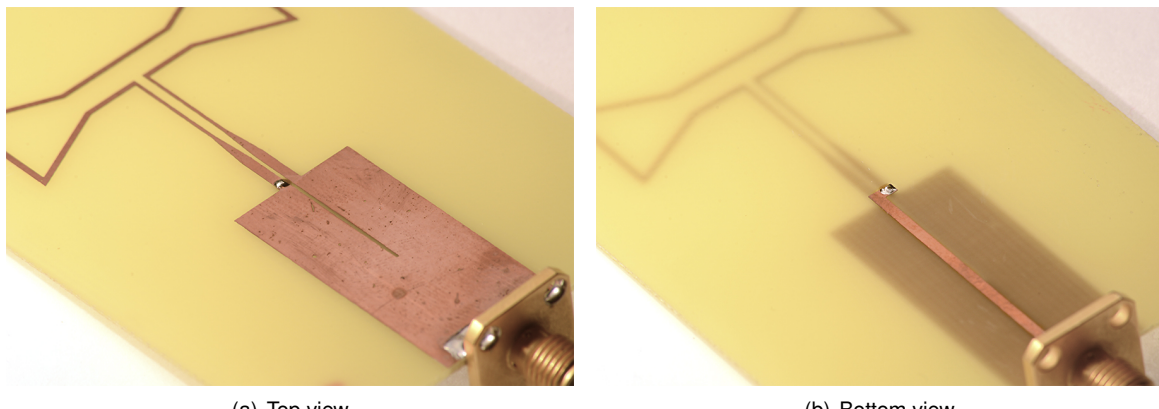


Figure 5.1: Balun A impedance test board including the proposed antenna

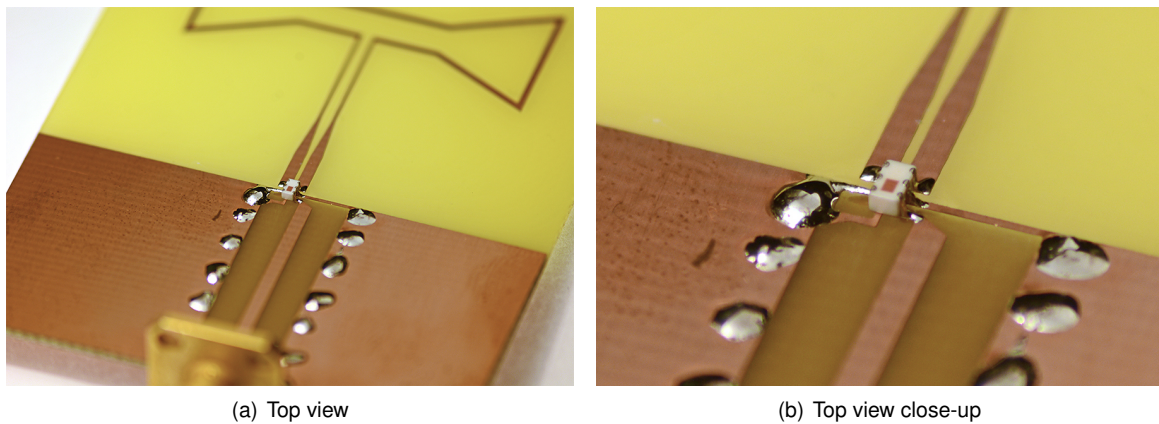
Note that these boards (except the test fixture) do not measure the actual value of the differential impedance antenna at its reference plane. Instead it is possible to obtain the impedance of the boards above presented, and assuming a satisfactory impedance conversion ratio of 1:2, it can be determined



(a) Top view

(b) Bottom view

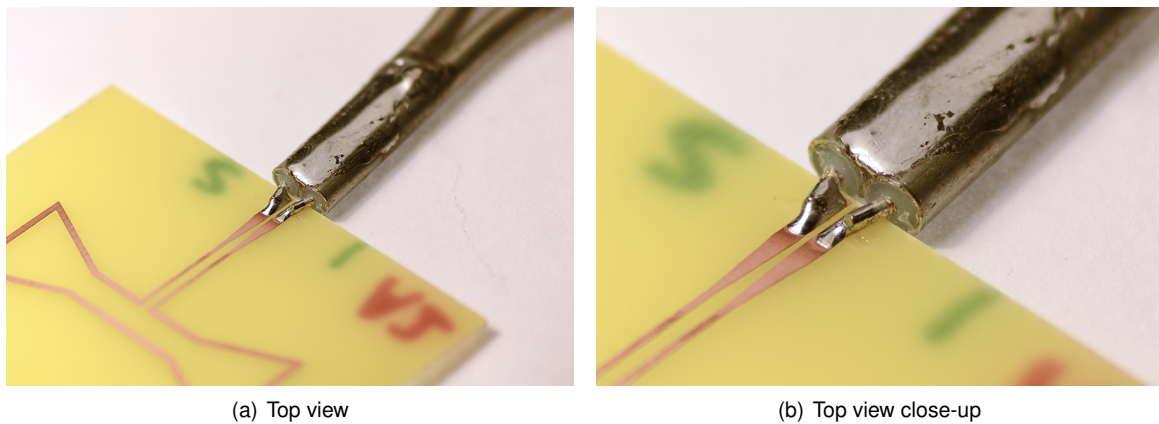
Figure 5.2: Balun B impedance test board including the proposed antenna



(a) Top view

(b) Top view close-up

Figure 5.3: Ceramic Balun impedance test board including the proposed antenna



(a) Top view

(b) Top view close-up

Figure 5.4: Test fixture impedance test board including the proposed antenna

the actual performance of the balun, thus revealing a measure of antenna impedance.

The figure 5.5 illustrates the impedance curves for the test boards. The curves were obtained by performing a return loss (reflection coefficient) measurement and converted to impedance with the equation 3.5.

The impedance of the boards is expected to be  $50 \Omega$  assuming that the antenna acts as perfect load

with  $100 \Omega$  differential impedance. The results for the Balun A and Balun B are satisfactory at 2.45 GHz, showing an impedance magnitude of  $57.1 \Omega$  and  $53.1 \Omega$ , respectively. The integrated commercial balun shows an impedance of  $40.5 \Omega$  which reveals fairly poor results. However, contrary to the good results declared in the cited references of section 4.4 for this test fixture concept, the magnitude of impedance measured was  $134 \Omega$  against the expected  $100 \Omega$ .

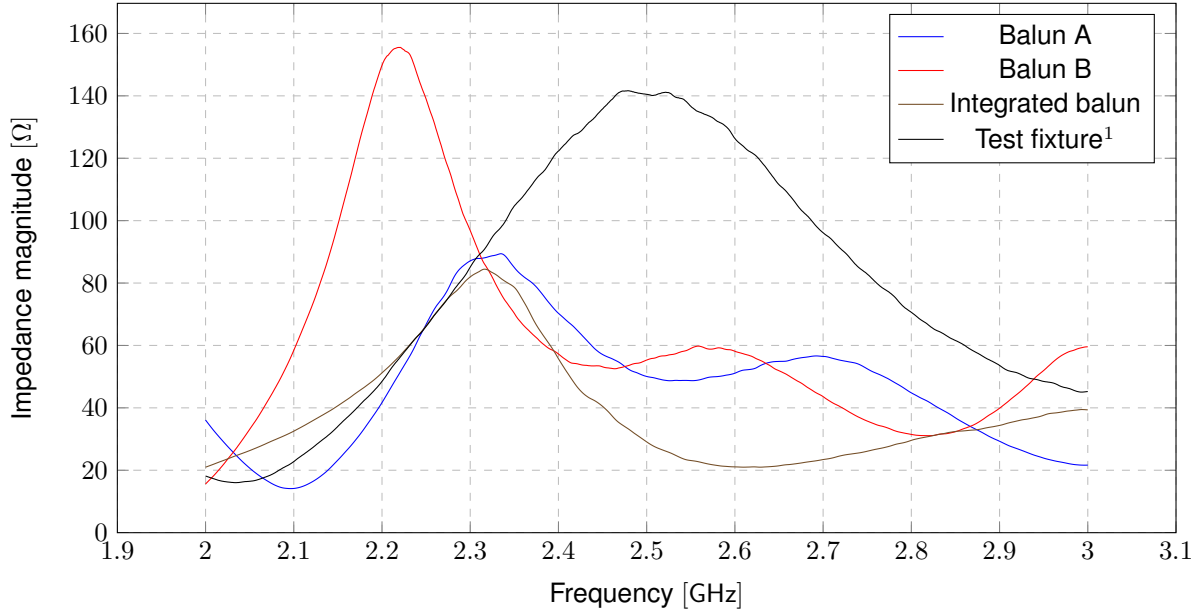


Figure 5.5: Impedance magnitude measurements. <sup>1</sup>Normalized to  $100 \Omega$

### 5.3 Radiation patterns

The radiation measurements were performed in an anechoic chamber (figure 5.6) to replicate the free space environment used in the simulations. The prototype including the above mentioned antennas are mounted on a rotating tower and an reception horn antenna is placed in the opposite side of the chamber while the tower turns  $360^\circ$ . By doing that, the relative power received can be plotted in a polar plot. This measurement also provides a relative gain comparison considering that transmit power of the radio transceiver was set to 0 dBm at all the tested boards.

To obtain the radiation patterns for the E-plane and H-plane of the studied antennas, the antenna plane of interest had to be turned. For instance, in figure 5.7, are illustrated the ceramic chip antenna mounted in different positions on the rotating tower for the E-plane and H-plane measurements.

Note that when the antennas are place in rotating head platform, part of it prevents the horn antenna to receive the transmitted power by antenna under test because it covers approximately  $60^\circ$ , which is represented by a red area on the figures of the next sections hence this range should not be considered as a valid measurement.

The radiation patterns illustrated next were plotted in linear scaling.

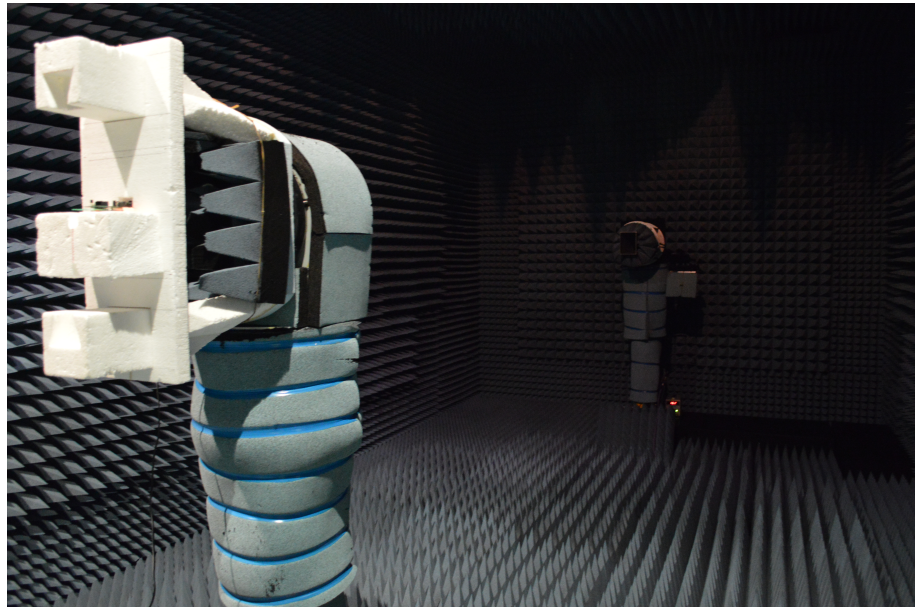


Figure 5.6: Anechoic chamber mounting setup

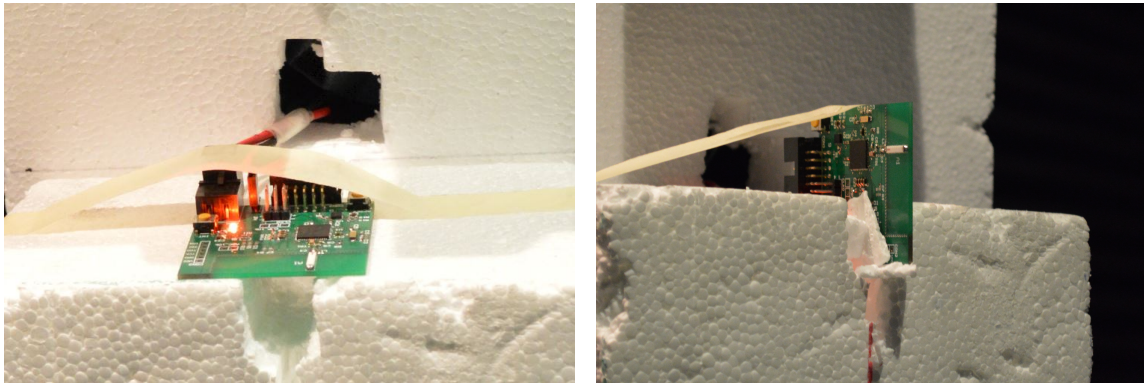


Figure 5.7: Measurement positions for both E-plane and H-plane of the chip antenna

### 5.3.1 Bowtie-Shaped Folded Dipole (antenna proposal)

As shown in 3.29, the prototype board includes some circuitry, and hence a ground plane. As expected, every antenna mounted near a ground plane would affect its radiation pattern. Considering this, and in order to accurately compare the proposed antenna radiation pattern with the prototyped antenna, a simulation featuring a simplified model of the printed circuit ground plane (figure 5.8) was performed. Bowtie-shaped folded dipole simulated and measured radiation are shown in figure 5.9 linear scaling. A fair agreement has been observed in the visible range not obliterated by the rotating tower.

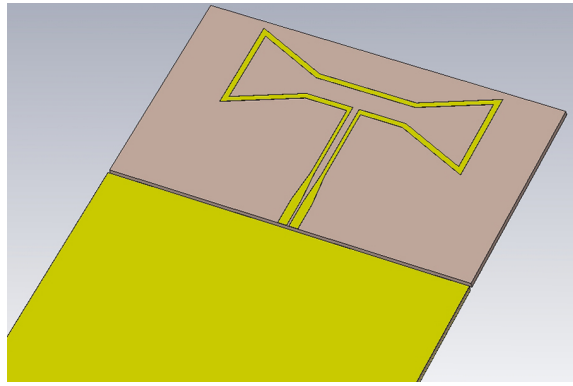


Figure 5.8: Simplified 3D model of node prototype including the proposed antenna

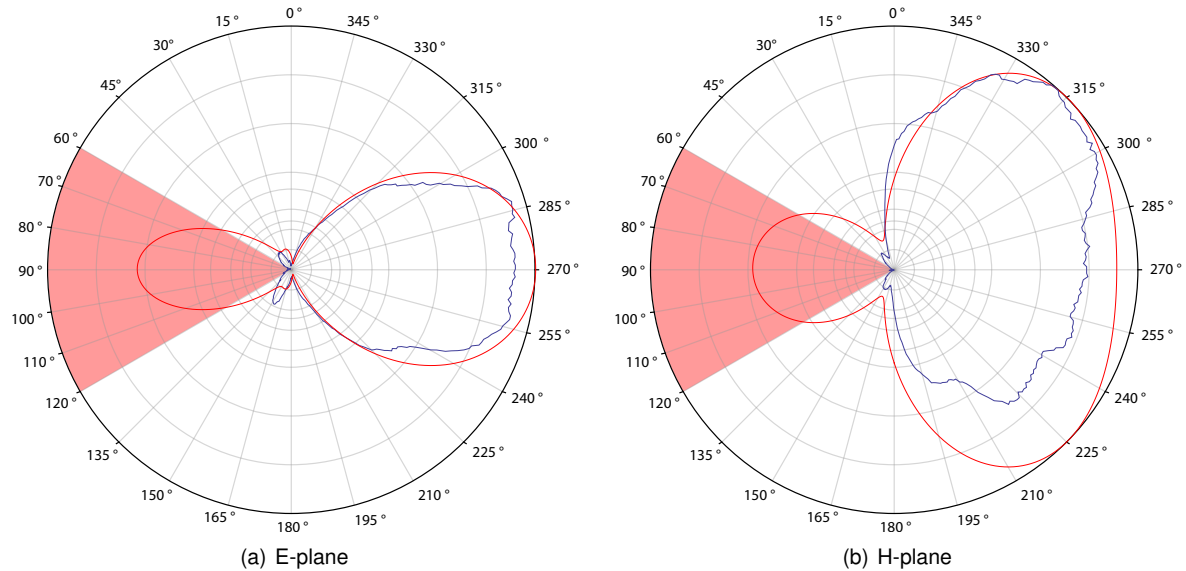


Figure 5.9: Bowtie-shaped folded dipole simulated and measured radiation pattern (linear scaling). Normalised at its maximum (H-plane)

### 5.3.2 Whip antenna (Pulse Electronics W1030)

The measured radiation pattern of the whip antenna studied in chapter 3 is illustrated in figure 5.10. The near-omnidirectional pattern is noticeable in the H-plane. However, when normalised to the proposed antenna maximum, it exhibits a worse performance between  $180^\circ$  and  $360^\circ$ .

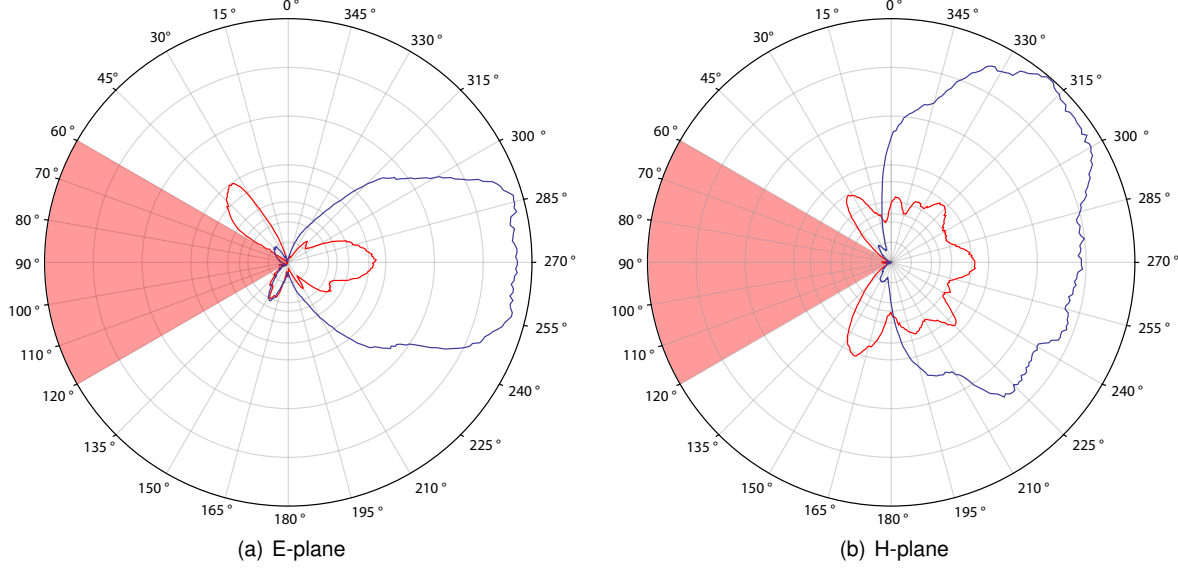


Figure 5.10: Whip antenna and proposed antenna radiation pattern comparison (linear scaling). Normalised at the maximum of the proposed antenna.

### 5.3.3 Chip antenna (JTI 2450AT45A100)

The previous WSN node prototype including the chip antenna was also subject of testing. It was fairly difficult compared the radiation patterns of the chip antenna and the proposed antenna when normalised to the BSFD maximum. Thus, in order to properly analyse its radiation pattern it was normalised to its maximum (E-plane XY). It is noted -16.2 dB of maximum power difference relatively to the proposed antennas maximum. This suggests a poor performance of the antenna and it is believed that it was not properly tuned, despite that fact that was strictly designed according to a detailed mounting guide specifically written to the combined structure of the micro-controller of interest and this specific ceramic chip antenna.

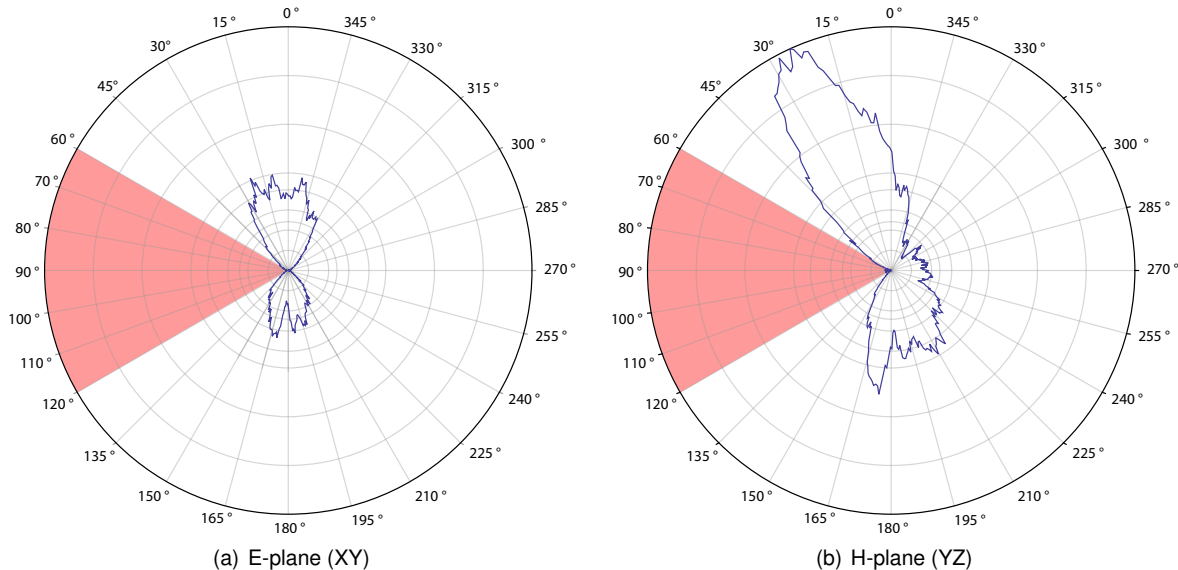


Figure 5.11: Chip antenna radiation pattern (linear scaling). Normalised at its maximum (E-Plane)

### 5.3.4 Conclusions

The measured radiation pattern for the bowtie-shaped folded dipole (BSFD), presented in figure 5.9, revealed a good agreement with the new simulated results. Despite the fact that it was not possible to measure the whole surrounding area of the antenna, it is expected to achieve better performance at all aspects relatively to the chip antenna and also to have a better gain and performance between 180 ° and 360 ° than the whip antenna.

The maximum received power on the horn antenna (RX antenna) for the proposed antenna was -16.1 dBm while for the whip antenna was -20.3 dBm. It is noted the inferior performance of the ceramic chip antenna which made impossible to receive a power over -30.1 dBm.

Although not illustrated, cross-polarization was also evaluated. Good results were again obtained for the proposed and whip antennas as well as for the chip antenna. The table 5.1 includes a comparison of the received power in the horn and the maximum cross-polarisation measured in negative dB.

Antennas	Maximum received power <sup>1</sup>	Maximum cross-polarisation <sup>1</sup>
Proposed antenna (BSFD)	-16.1 dBm	-16.6 dB
Whip antenna	-20.3 dBm	-21.1 dB
Chip antenna	-30.2 dBm	-35.1 dB

<sup>1</sup> Maximum values for both E-plane and H-plane

Table 5.1: Maximum received power and cross-polarisation for the antennas measured in the anechoic chamber

# Chapter 6

## Conclusions

The objectives of this dissertation were to study, develop and measure an antenna for a wireless sensor network node, intended to be used in an agricultural application and enhance the communication performance between nodes.

This chapter summarises the conclusions and results obtained. Several antennas were studied within the scope of this work. They were divided into two major classes: unbalanced and balanced antennas.

Unbalanced antennas comprise some of the most commonly used antennas in wireless sensor network communication modules, namely the following studied antennas: Planar Inverted F-antenna, ceramic chip antenna and whip antenna. A comparison of these is presented based on simulations and manufacturers datasheets. After an optimisation of the design varying its mechanical dimensions good performance could be obtained with a PIFA. According to the Johanson Inc. manufacturer, the ceramic chip antenna can also lead to satisfactory results when properly tuned. However, this can only be achieved using trial and error methods conditioned by external factors. The whip antenna, or more precisely, a quarter-wavelength dipole antenna was also considered. The fact that it can be placed outside an enclosure case makes this antenna the most used in medium-large size communication modules for WSNs. However, this antenna is more costly than other antennas such as the printed antennas (PIFA) or even chip antennas. Thus, the option of implementing a whip antenna may not be sustainable in a large scale WSN.

As a main drawback, this first class of studied (unbalanced) antennas requires a conversion circuitry to match the balanced RF port of the micro-controller transceiver used in this project. Besides the fact that this circuitry adds financial substance to the overall price of the WSN node, it also adds minor losses in the conversion process.

Balanced antennas designs are also discussed in this work. The first antenna studied was a differential fed patch antenna. This antenna design was inspired on an existing concept which features a directional pattern diagram. Despite being slightly modified relatively to the original concept removing its ground plane, the radiation pattern keeps its directional characteristic.

A multiple conductor folded dipole based on a four-folded dipole structure was also studied. Although the manufacturer moderate results in terms of return loss, it was impossible to replicate its behaviour

through simulations. For this reason, this antenna design was not pursued.

The third studied antenna was a dual-band dipole antenna. This antenna shows resonances in two different frequencies, one of them of interest, and it fitted all the requirements and manufacturing constraints of this work's project, thus, it should be considered and compared to the solutions addressed next.

An antenna design based on differential fed patch dipole, has also been studied. The antenna was re-scaled and optimised relatively to the original concept dimensions in order to cover the required frequency range and differential impedance. Good curve results were achieved for both the return loss and impedance (resistance and reactance). However, the mechanical dimensions of the coplanar stripline prevent this design from being manufactured by Seeedstudio Company. Nevertheless this antenna should be considered as a possible candidate for other projects if a manufacturer is interested.

A simple concept of a printed folded dipole was also considered but since its mechanical dimensions (62mm width) would exceed the width of the available design area (50 mm), this antenna was discarded in this project.

Finally, a Bowtie-Shaped Folded Dipole (BSFD) as been introduced. By re-designing the ends of the dipole's arms to increase its electrical length, all requirements can thus be met. The return loss and impedance were optimised to the desired project requirements and good results were found. A prototype node that included designed BSFD was tested.

In order to experimentally confirm the simulated results of the proposed BSDF, several microstrip to coplanar transitions were studied and designed. These structures include three baluns to convert a 50 Ohm microstrip line impedance to a 100 Ohm CPS differential impedance. Another structure, so called test fixture was also studied. A first balun (A) consists in a proven concept and it was optimally designed to 2.45 GHz. Although the original concept of the balun was a Microstrip-GCPW transition, simulations reveal optimistic results for the final design which were proven through an experimental characterisation.

A second balun (B) consists of simple microstrip-CPS transition. It features a microstrip line supported by a "half-fissured" ground plane and connected at its end through a via structure. Although the structure may seem complex, the theory is far way simpler making this balun an accurate measuring structure. However, these baluns (A and B) were designed to optimally perform at 2.45 GHz, which makes them narrowband structures which may not lead to good result at other frequencies.

A third commercial ceramic balun was characterised using two methods. The first method consists in measuring the insertion and return loss of the balun using only a two-port VNA contrary to the second method. With the latter, it is possible to achieve a more precise characterisation due to its mounting setup that considers the balun as true three-port device. Despite the fact that the characterisation reveals that this balun may not be able to provide a true 2:1 impedance conversion required at 2.45 GHz, the manufacturer minimum specifications are guaranteed.

Finally the studied baluns were implemented with the proposed antenna built prototype. Measurements of the reflection coefficient (return loss) were performed and converted to the respective impedance, normalised to 50 Ohm. Although the best impedance result was obtained with the balun B, balun A also provided satisfactory results. The ceramic balun presents a worse impedance mismatch

relatively to 50 Ohm caused by different impedance conversion ratio at 2.45 GHz. Note that impedance measurements were also performed in this work making use of a test fixture, but the results showed some inconsistency, and improving this technique should deserve some attention.

At last, an experimental comparison of the radiation patterns of some studied antennas integrated in a node have been presented. Moreover, these experimental measurements allow a relative comparison of the power transmitted by the actual measured antennas. The radiation diagram for the proposed antenna is distorted by the circuit ground plane and the whip antenna provides an overall good performance. Since the chip antenna exhibits bad performance in terms of the expected omni-directional radiation pattern and poor radiation efficiency, leading to short communication range, the BSFD has proven to be a better solution.

The author believes that this thesis has met all the proposed objectives.

## 6.1 Future Work

Improvements can be made in enhancing differential impedance measurements, with a TRL calibration set of printed boards. However, this requires calibration expertise and accurate PCB printing techniques.

The micro-controller used provides an RX antenna diversity extended feature, which includes a self-contained diversity algorithm that switches to the most reliable RF signal path hence improving the overall connection quality between nodes of a WSN.

Thus, as future work, multiple antennas could be used, allowing to reduce the effects of multipath propagation and fading and benefiting from MIMO techniques.

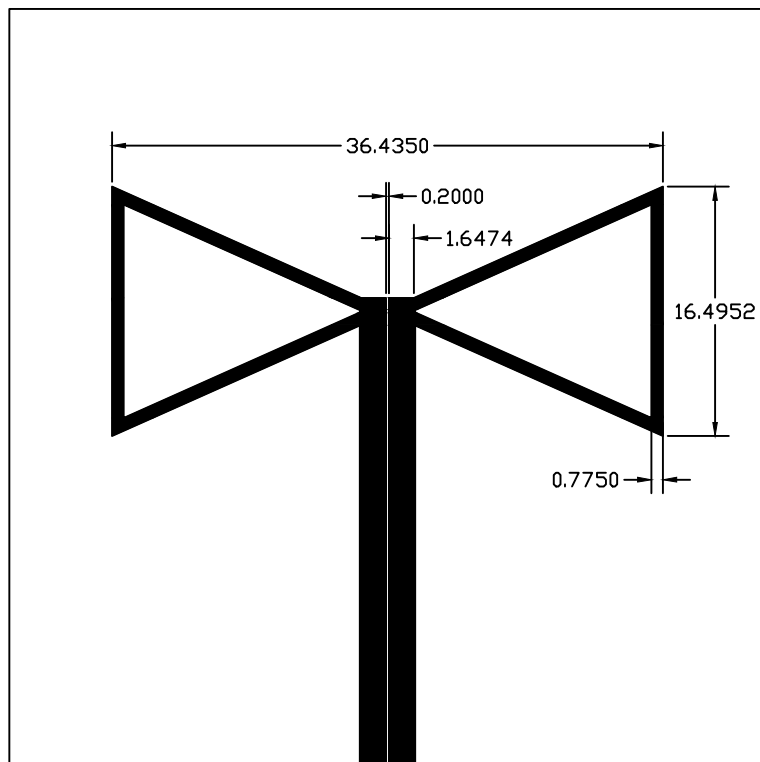


## **Appendix A**

# **Antennas and baluns mechanical dimensions**

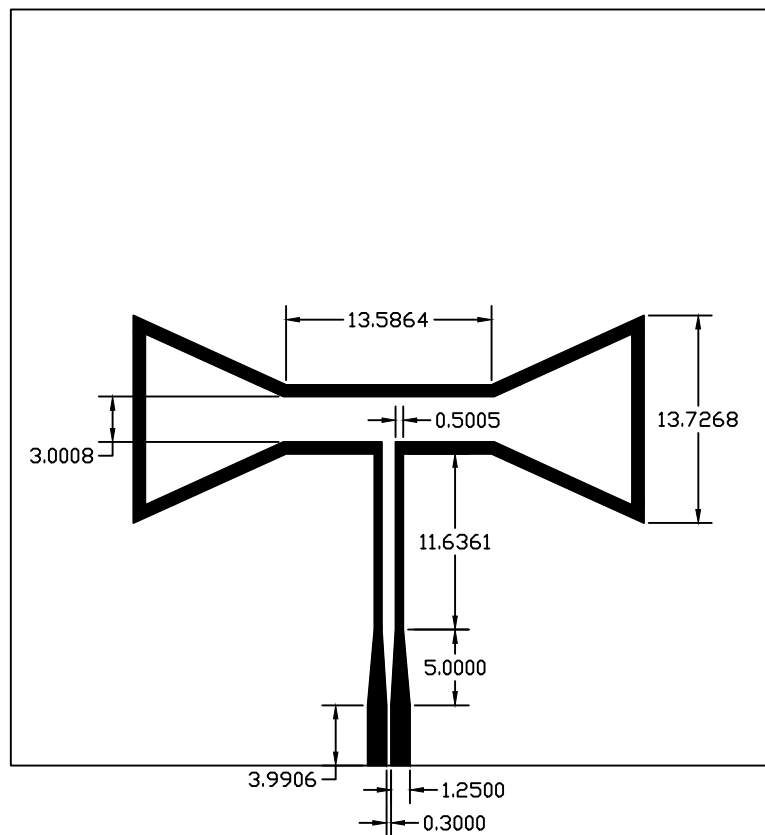
In this appendix, all the major mechanical dimensions of the relevant studied structures are presented. This includes: the bowtie antenna, the proposed antenna (BSFD), the Balun A and Balun B.





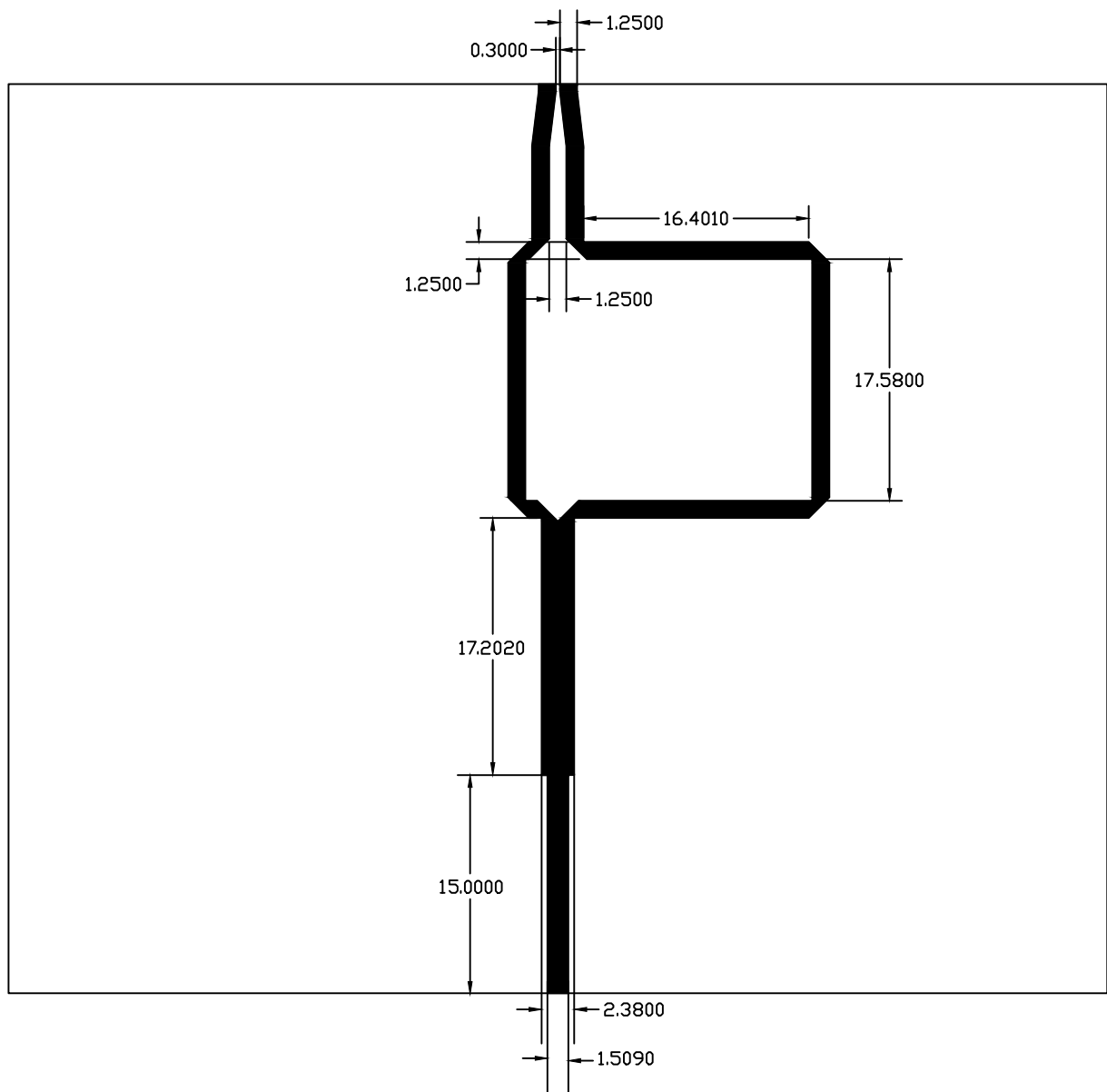
NOTES

DWG NAME:	Bowtie	DWG NO.:	1/1 - Front
DRAWN:	Tiago Parra	APPROVED:	Eng. Nuno Pires
SCALE:	2:1	DATE:	



NOTES

DWG NAME:	BFD	DWG NO.:	1/1 - Front
DRAWN:	Tiago Parra	APPROVED:	Eng. Nuno Pires
SCALE:	2:1	DATE:	



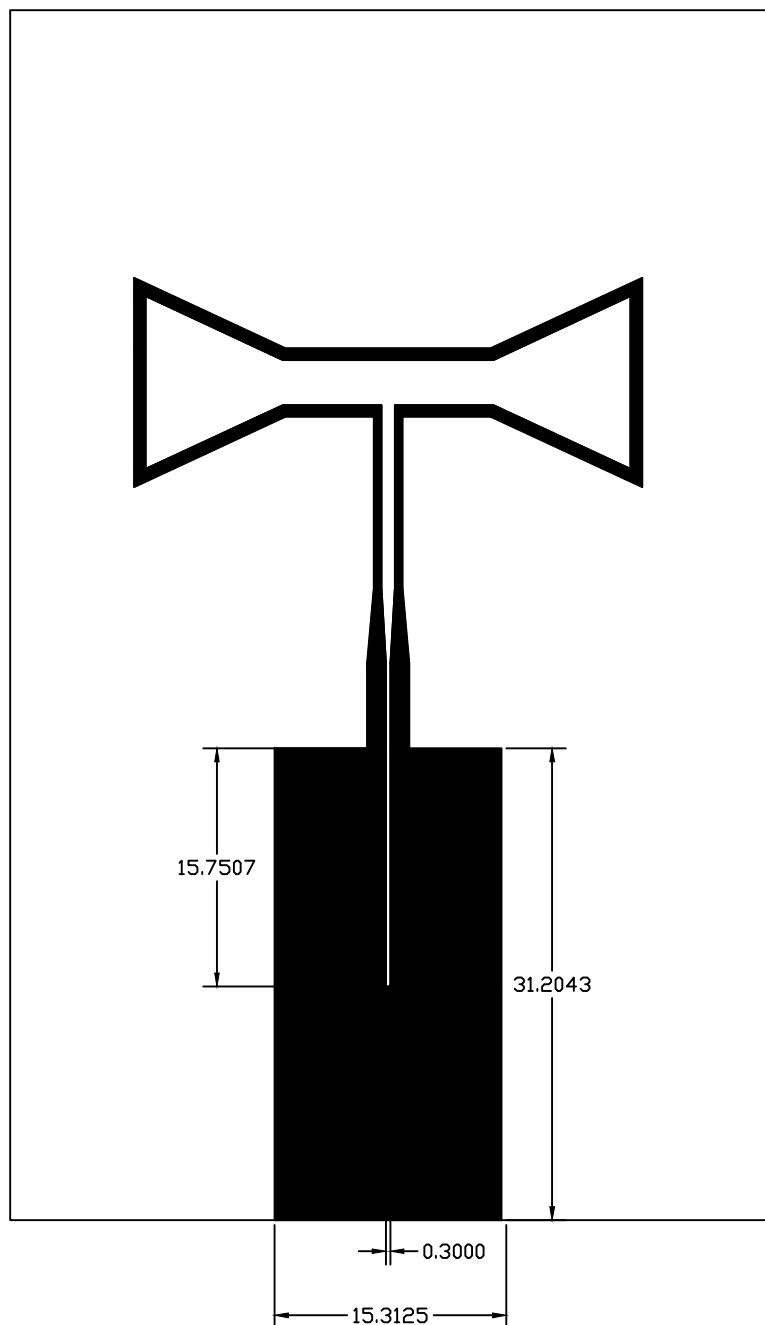
NOTES

DWG NAME:	Balun A	DWG NO.:	1/2 - Front
DRAWN:	Tiago Parra	APPROVED:	Eng. Nuno Pires
SCALE:	2:1	DATE:	



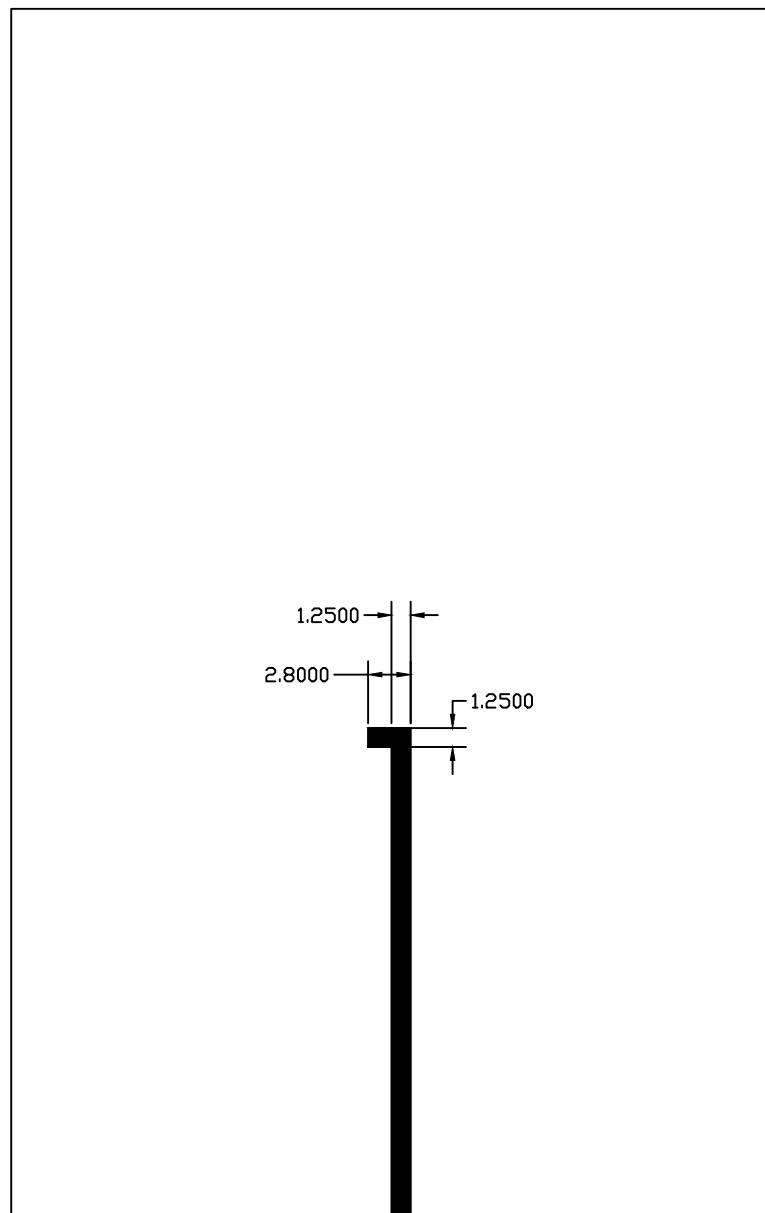
## NOTES

DWG NAME:	Balun A	DWG NO.:	2/2 - Back
DRAWN:	Tiago Parra	APPROVED:	Eng. Nuno Pires
SCALE:	2:1	DATE:	



## NOTES

DWG NAME:	Balun B	DWG NO.:	1/2 - Front
DRAWN:	Tiago Parra	APPROVED:	Eng. Nuno Pires
SCALE:	2:1	DATE:	



## NOTES

DWG NAME:	Balun B	DWG NO.:	2/2 - Back
DRAWN:	Tiago Parra	APPROVED:	Eng. Nuno Pires
SCALE:	2:1	DATE:	

# Bibliography

- [1] C. Raghavendra, K. Sivalingam, and T. Znati, *Wireless Sensor Networks*, ser. Ercoftac Series. Springer, 2004.
- [2] J. Huang, “Microstrip antennas for commercial applications,” *Microstrip Antennas, DM pozar and DH Schubert*, pp. 371–379, 1995.
- [3] *Microstrip Microwave Antennas*, ser. 3rd USAF Symp. on Antennas, 1953.
- [4] N. Instruments. What is a wireless sensor network. [Online]. Available: <http://www.ni.com/white-paper/7142/en/>
- [5] I. Akyildiz and M. Vuran, *Wireless Sensor Networks*, ser. Advanced Texts in Communications and Networking. Wiley, 2010.
- [6] R. Wagner, “Standards-based wireless sensor networking protocols for spaceflight applications,” in *Aerospace Conference, 2010 IEEE*, March 2010, pp. 1–7.
- [7] H. Zhang and C. Liu, “A review on node deployment of wireless sensor network.” *International Journal of Computer Science Issues (IJCSI)*, vol. 9, no. 6, 2012.
- [8] M. Younis and K. Akkaya, “Strategies and techniques for node placement in wireless sensor networks: A survey,” *Ad Hoc Networks*, vol. 6, no. 4, pp. 621 – 655, 2008. [Online]. Available: <http://www.sciencedirect.com/science/article/pii/S1570870507000984>
- [9] G. Tuna, T. Mumcu, K. Gulez, V. Gungor, and H. Erturk, “Unmanned aerial vehicle-aided wireless sensor network deployment system for post-disaster monitoring,” in *Emerging Intelligent Computing Technology and Applications*, ser. Communications in Computer and Information Science, D.-S. Huang, P. Gupta, X. Zhang, and P. Premaratne, Eds. Springer Berlin Heidelberg, 2012, vol. 304, pp. 298–305. [Online]. Available: [http://dx.doi.org/10.1007/978-3-642-31837-5\\_44](http://dx.doi.org/10.1007/978-3-642-31837-5_44)
- [10] M. R. Senouci, A. Mellouk, H. Senouci, and A. Aissani, “Performance evaluation of network lifetime spatial-temporal distribution for wsn routing protocols,” *Journal of Network and Computer Applications*, vol. 35, no. 4, pp. 1317–1328, 2012.
- [11] L. Alazzawi, A. Elkateeb, and A. Ramesh, “Scalability analysis for wireless sensor networks routing protocols,” in *Advanced Information Networking and Applications - Workshops, 2008. AINAW 2008. 22nd International Conference on*, March 2008, pp. 139–144.

- [12] J. Gilbert and F. Balouchi, "Comparison of energy harvesting systems for wireless sensor networks," *International Journal of Automation and Computing*, vol. 5, no. 4, pp. 334–347, 2008. [Online]. Available: <http://dx.doi.org/10.1007/s11633-008-0334-2>
- [13] Coalesenses, *iSense Environmental Sensor Module*. [Online]. Available: <http://www.coalesenses.com/index.php/products/solutions/isense-modules/environmental-sensor-module/>
- [14] M. Durisic, Z. Tafa, G. Dimic, and V. Milutinovic, "A survey of military applications of wireless sensor networks," in *Embedded Computing (MECO), 2012 Mediterranean Conference on*, June 2012, pp. 196–199.
- [15] S. H. Lee, S. Lee, H. Song, and H.-S. Lee, "Wireless sensor network design for tactical military applications : Remote large-scale environments," in *Military Communications Conference, 2009. MILCOM 2009. IEEE*, Oct 2009, pp. 1–7.
- [16] M. Hussain, P. Khan, and K. kyung Sup, "Wsn research activities for military application," in *Advanced Communication Technology, 2009. ICACT 2009. 11th International Conference on*, vol. 01, Feb 2009, pp. 271–274.
- [17] M. Maroti, G. Simon, A. Ledeczi, and J. Sztipanovits, "Shooter localization in urban terrain," *Computer*, vol. 37, no. 8, pp. 60–61, 2004.
- [18] F. Resquin, J. Guevara, C. Cardozo, C. Santacruz, and F. Brunetti, "A low power routing and topology control protocol for cluster-based environmental wireless sensor networks: The flora project case," in *Mobile Adhoc and Sensor Systems (MASS), 2011 IEEE 8th International Conference on*, Oct 2011, pp. 132–134.
- [19] X. Jiang, G. Zhou, Y. Liu, and Y. Wang, "Wireless sensor networks for forest environmental monitoring," in *Information Science and Engineering (ICISE), 2010 2nd International Conference on*, Dec 2010, pp. 2514–2517.
- [20] D. Herring and R. Simmon. Precision agriculture. [Online]. Available: <http://earthobservatory.nasa.gov/Features/PrecisionFarming/>
- [21] Precision agriculture - vineyards and greenhouses. [Online]. Available: <http://www.probesrl.net/>
- [22] K. Langendoen, A. Baggio, and O. Visser, "Murphy loves potatoes: experiences from a pilot sensor network deployment in precision agriculture," in *Parallel and Distributed Processing Symposium, 2006. IPDPS 2006. 20th International*, April 2006, pp. 8 pp.–.
- [23] V. Jelicic, T. Razov, D. Oletic, M. Kuri, and V. Bilas, "Maslinet: A wireless sensor network based environmental monitoring system," in *MIPRO, 2011 Proceedings of the 34th International Convention*, May 2011, pp. 150–155.
- [24] M. Mafuta, M. Zennaro, A. Bagula, G. Ault, H. Gombachika, and T. Chadza, "Successful deployment of a wireless sensor network for precision agriculture in malawi," in *Networked Embedded Systems for Every Application (NESEA), 2012 IEEE 3rd International Conference on*, Dec 2012, pp. 1–7.

- [25] X. Shu-ming, W. Liang-Min, Q. Xiao-qian, and Z. Yong-Zhao, "Application research of wsn in precise agriculture irrigation," in *Environmental Science and Information Application Technology, 2009. ESIAT 2009. International Conference on*, vol. 2, July 2009, pp. 297–300.
- [26] P. Patil, H. Vidya, S. Patil, and U. Kulkarni, "Wireless sensor network for precision agriculture," in *Computational Intelligence and Communication Networks (CICN), 2011 International Conference on*, Oct 2011, pp. 763–766.
- [27] K. Konstantinos, X. Apostolos, K. Panagiotis, and S. George, "Topology optimization in wireless sensor networks for precision agriculture applications," in *Sensor Technologies and Applications, 2007. SensorComm 2007. International Conference on*, Oct 2007, pp. 526–530.
- [28] L. C. D. S.L., "Agriculture 2.0. technical guide," last access: 2014-02-21. [Online]. Available: <http://www.libelium.com/>
- [29] T. Gao, C. Pesto, L. Selavo, Y. Chen, J. Ko, J. H. Lim, A. Terzis, A. Watt, J. Jeng, B. rong Chen, K. Lorincz, and M. Welsh, "Wireless medical sensor networks in emergency response: Implementation and pilot results," in *Technologies for Homeland Security, 2008 IEEE Conference on*, May 2008, pp. 187–192.
- [30] J. M. Kahn, R. H. Katz, and K. S. Pister, "Next century challenges: mobile networking for "smart dust"," in *Proceedings of the 5th annual ACM/IEEE international conference on Mobile computing and networking*. ACM, 1999, pp. 271–278.
- [31] A. Wood, G. Virone, T. Doan, Q. Cao, L. Selavo, Y. Wu, L. Fang, Z. He, S. Lin, and J. Stankovic, "Alarm-net: Wireless sensor networks for assisted-living and residential monitoring," *University of Virginia Computer Science Department Technical Report*, vol. 2, 2006.
- [32] N. Suryadevara and S. Mukhopadhyay, "Wireless sensor network based home monitoring system for wellness determination of elderly," *Sensors Journal, IEEE*, vol. 12, no. 6, pp. 1965–1972, June 2012.
- [33] C. Baker, K. Armijo, S. Belka, M. Benhabib, V. Bhargava, N. Burkhardt, A. Der Minassians, G. Dervisoglu, L. Gutnik, M. Haick, C. Ho, M. Koplow, J. Mangold, S. Robinson, M. Rosa, M. Schwartz, C. Sims, H. Stoffregen, A. Waterbury, E. Leland, T. Pering, and P. Wright, "Wireless sensor networks for home health care," in *Advanced Information Networking and Applications Workshops, 2007, AINAW '07. 21st International Conference on*, vol. 2, May 2007, pp. 832–837.
- [34] K. Sohraby, D. Minoli, and T. Znati, *Wireless sensor networks: technology, protocols, and applications*. John Wiley & Sons, 2007.
- [35] A. Corporation, "Atmega128rfa1 - microcontroller with low power 2.4ghz transceiver for zigbee and ieee 802.15.4," last access: 2014-03-20. [Online]. Available: <http://www.atmel.com/Images/doc8266.pdf>
- [36] Texas Instruments, *2.4 GHz Inverted F Antenna*, ser. Design Note DN0007, April 2007.

- [37] “3MATE! - 2.4GHZ IEEE 802.15.4 WSN MODULE ,” accessed: 2014-01-30. [Online]. Available: <http://www.tretecl.it/public/webroot/default.asp?pID=OaA9luYtqkls>
- [38] Texas Instruments, *CC-Antenna-DK and Antenna Measurements Summary*, ser. Design Note eDN031, April 2010.
- [39] ——, *Antenna Selection Guide*, ser. Application Note AN058, October 2010.
- [40] Freescale Semiconductor, *Compact Integrated Antennas*, ser. Application Note AN2731, December 2012.
- [41] I. Johanson Technology, “Antenna Tuning and Characterization Services,” <http://www.johansontechnology.com/images/stories/ip/Johanson-Antenna-Service-Website-and-Flyer.pdf>, 2009, [Online; accessed 2-February-2014].
- [42] ——, “2.45 ghz high gain smd chip antenna.” [Online]. Available: <http://www.johansontechnology.com/datasheets/antennas/2450AT45A100.pdf>
- [43] Pulse Electronics, *Wireless External Antenna for 2.4 GHz Applications - Part Number W1030*.
- [44] K. Gupta, *Microwaves*. Wiley Eastern, 1979.
- [45] V. Fouad Hanna, “Finite boundary corrections to coplanar stripline analysis,” *Electronics Letters*, vol. 16, no. 15, pp. 604–606, 1980.
- [46] A. S. S. Lutz, K. Baur and T. Walter, “Lens based 24 ghz sige iq radarsensor for a multitude of applications,” in *7th European Conference on Antennas and Propagation*, Apr. 2013.
- [47] Atmel, “Design and characterization of the Radio Controller Board’s 2.4GHz PCB Antenna,” August 2007. [Online]. Available: <http://www.atmel.com/Images/doc8095.pdf>
- [48] P. Nepa, G. Manara, S. Mugnaini, G. Tribellini, S. Cioci, G. Albasini, and E. Sacchi, “Differential planar antennas for 2.4/5.2 ghz wlan applications,” in *Antennas and Propagation Society International Symposium 2006, IEEE*, July 2006, pp. 973–976.
- [49] I. Rosu. Wideband printed bow-tie antenna. [Online]. Available: [http://www.qsl.net/va3iul/Antenna/Printed\\_and\\_Microstrip\\_Antennas/Wideband\\_Printed\\_Bow\\_Tie\\_Antenna.gif](http://www.qsl.net/va3iul/Antenna/Printed_and_Microstrip_Antennas/Wideband_Printed_Bow_Tie_Antenna.gif)
- [50] D. Bockelman and W. Eisenstadt, “Combined differential and common-mode scattering parameters: theory and simulation,” *Microwave Theory and Techniques, IEEE Transactions on*, vol. 43, no. 7, pp. 1530–1539, Jul 1995.
- [51] D. Jorgesen and C. Marki, “A tutorial on baluns, balun transformers, magic-ts, and 180° hybrids,” 2014.
- [52] Y. Qian and T. Itoh, “A broadband uniplanar microstrip-to-cps transition,” in *Microwave Conference Proceedings, 1997. APMC '97, 1997 Asia-Pacific*, Dec 1997, pp. 609–612 vol.2.

- [53] D. Pozar, *Microwave Engineering*, 3Rd Ed. Wiley India Pvt. Limited, 2009.
- [54] R. Douville and D. James, "Experimental study of symmetric microstrip bends and their compensation," *Microwave Theory and Techniques, IEEE Transactions on*, vol. 26, no. 3, pp. 175–182, Mar 1978.
- [55] K. W. Kim, "Balance analysis of microstrip-to-cps baluns and its effects on broadband antenna performance," *International Journal of Antennas and Propagation*, vol. 2013, 2013.
- [56] H.-R. Chuang and L.-C. Kuo, "3-d fDTD design analysis of a 2.4-ghz polarization-diversity printed dipole antenna with integrated balun and polarization-switching circuit for wlan and wireless communication applications," *Microwave Theory and Techniques, IEEE Transactions on*, vol. 51, no. 2, pp. 374–381, Feb 2003.
- [57] I. Johanson Technology, "2.45 ghz 1:2 impedance balun," May 2011, last access: 2014-02-07. [Online]. Available: <http://www.johansontechnology.com/datasheets/antennas/2450AT45A100.pdf>
- [58] I. Anaren Ceramics, "Measurement techniques for baluns," May 2005, last access: 2014-02-21. [Online]. Available: [http://www.anaren.com/sites/default/files/uploads/File/BalunTesting\\_0.pdf](http://www.anaren.com/sites/default/files/uploads/File/BalunTesting_0.pdf)
- [59] I. Vishay Intertechnology, "50 ghz thin film microwave resistors," accessed: 2014-01-07. [Online]. Available: <http://www.farnell.com/datasheets/1500277.pdf>
- [60] A. Technologies, "Open/short response calibration (reflection test)," accessed: 2014-01-24. [Online]. Available: [http://ena.tm.agilent.com/e5061b/manuals/webhelp/eng/measurement/calibration/basic\\_calibrations/open\\_short\\_response\\_calibration\\_reflection\\_test.htm](http://ena.tm.agilent.com/e5061b/manuals/webhelp/eng/measurement/calibration/basic_calibrations/open_short_response_calibration_reflection_test.htm)
- [61] Atmel, "Atmel AT02865: RF Layout with Microstrip," May 2013. [Online]. Available: [http://www.atmel.com/Images/Atmel-42131-RF-Layout-with-Microstrip\\_Application-Note\\_AT02865.pdf](http://www.atmel.com/Images/Atmel-42131-RF-Layout-with-Microstrip_Application-Note_AT02865.pdf)
- [62] S. Hageman, "Via spacing on high-performance pcbs," February 2013. [Online]. Available: <http://www.edn.com/electronics-blogs/the-practicing-instrumentation-engineer/4406491/Via-spacing-on-high-performance-PCBs>
- [63] B. Rautio and J. Coonrod, "Comparing microstrip and cpw performance," July 2012.
- [64] L. C. D. S.L., "Bit-1040-0003-0, usb 3.0 cable adapter kit no. 3." [Online]. Available: [http://www.bitifeye.com/cms/front\\_content.php?idart=711](http://www.bitifeye.com/cms/front_content.php?idart=711)
- [65] X. Qing, C. K. Goh, and Z.-N. Chen, "Impedance characterization of rfid tag antennas and application in tag co-design," *Microwave Theory and Techniques, IEEE Transactions on*, vol. 57, no. 5, pp. 1268–1274, May 2009.
- [66] R. Meys and F. Janssens, "Measuring the impedance of balanced antennas by an s-parameter method," *Antennas and Propagation Magazine, IEEE*, vol. 40, no. 6, pp. 62–65, Dec 1998.
- [67] S.-K. Kuo, S.-L. Chen, and C.-T. Lin, "An accurate method for impedance measurement of rfid tag antenna," *Progress In Electromagnetics Research*, vol. 83, pp. 93–106, 2008.

- [68] A. G. Santiago, "Antennas for body area networks," Master's thesis, Instituto Superior Técnico - Universidade de Lisboa, April 2010.
- [69] K. Palmer and M. van Rooyen, "Simple broadband measurements of balanced loads using a network analyzer," *Instrumentation and Measurement, IEEE Transactions on*, vol. 55, no. 1, pp. 266–272, Feb 2006.
- [70] S. Konya, T. Sasamori, T. Tobana, and Y. Isota, "Calibration of impedance measurement of a balanced antenna using the s-parameter method," in *Proc. ISAP*, 2010.
- [71] H. Zhu, Y. Ko, and T. Ye, "Impedance measurement for balanced uhf rfid tag antennas," in *Radio and Wireless Symposium (RWS), 2010 IEEE*, Jan 2010, pp. 128–131.
- [72] John Donovan, "Selecting Antennas for Embedded Designs," August 2012, accessed: 2014-01-24. [Online]. Available: [http://ena.tm.agilent.com/e5061b/manuals/webhelp/eng/measurement/calibration/basic\\_calibrations/open\\_short\\_response\\_calibration\\_reflection\\_test.htm](http://ena.tm.agilent.com/e5061b/manuals/webhelp/eng/measurement/calibration/basic_calibrations/open_short_response_calibration_reflection_test.htm)
- [73] G. Matthaei, *Microwave filters, impedance-matching networks, and coupling structures*. McGraw-Hill, 1964, no. vol. 1.
- [74] I. Akyildiz, W. Su, Y. Sankarasubramaniam, and E. Cayirci, "A survey on sensor networks," *Communications Magazine, IEEE*, vol. 40, no. 8, pp. 102–114, Aug 2002.
- [75] M. Quaritsch, K. Kruggl, D. Wischounig-Struci, S. Bhattacharya, M. Shah, and B. Rinner, "Networked uavs as aerial sensor network for disaster management applications," *e & i Elektrotechnik und Informationstechnik*, vol. 127, no. 3, pp. 56–63, 2010. [Online]. Available: <http://dx.doi.org/10.1007/s00502-010-0717-2>
- [76] J. Yick, B. Mukherjee, and D. Ghosal, "Wireless sensor network survey," *Computer Networks*, vol. 52, no. 12, pp. 2292 – 2330, 2008. [Online]. Available: <http://www.sciencedirect.com/science/article/pii/S1389128608001254>
- [77] I. Johanson Technology, "50 ghz thin film microwave resistors," accessed: 2014-01-07. [Online]. Available: <http://www.farnell.com/datasheets/1500277.pdf>
- [78] P. Harrop and R. Das, "Wireless sensor networks - 2012-2022 forecasts." [Online]. Available: <http://www.idtechex.com/research/reports/wireless-sensor-networks-wsn-2012-2022-forecasts-technologies-players-000314.asp>
- [79] "Design guide for high-speed controlled impedance circuit boards," 2004.
- [80] T. Deng, M. Leong, P. S. Kooi, and T. S. Yeo, "Synthesis formulas for coplanar lines in hybrid and monolithic mics," *Electronics Letters*, vol. 32, no. 24, pp. 2253–2254, 1996.